Turn-Key Stabilization and Digital Control of Scalable, N GTI Resonator Based Coherent Pulse Stacking Systems

by

Morteza Sheikhsofla

A dissertation submitted in partial fulfillment
of the requirements for the degree of
Doctor of Philosophy
(Electrical Engineering)
in the University of Michigan
2018

Doctoral Committee:

Professor Almantas Galvanauskas, Chair
Associate Research Scientist John A. Nees
Associate Professor Alexander Thomas
Professor Herbert G. Winful

Morteza Sheikhsofla

msheikhs@umich.edu

ORCID iD: 0000-0003-2177-4702

© Morteza Sheikhsofla 2018

Dedication

This Thesis is dedicated to my beloved parents

Acknowledgements

Making an acknowledgement list is really a difficult task for me, because the number of people whom I would like to show my gratitude to seems countless. If someone is missed in this list, he or she must be hidden in my heart. Certainly, I would start with the most important person in my PhD life, and he is my adviser Professor Almantas Galvanauskas. I would like to express my highest gratitude to him for playing many important roles in this period. He is definitely a smart, hardworking, passionate and supportive research adviser. There are many times during research, specifically experimental-based research that the desired results are not achieved easily perhaps a lot of times facing failure. I would say in all those cases he was even the first one before me trying to think and look for the solutions to resolve the issues and always provided great guidance to help me go across the barrier. He is among few faculty members that give enough space for creativity, thinking, and trial and errors to his students so that they can examine different ideas and find their best strengths in research and these are important things a PhD student always look for. In addition to being a good researcher, I also learned to never lose my hopes in achieving a goal in my life and I appreciate this lesson from him.

I want to thank all my committee members (Professor Herbert Winful, John Nees, and Professor Alec Thomas)' help in reviewing and evaluating my dissertation. I really appreciate the time and effort that you spend in evaluating and giving me feedback on my PhD thesis work. Moreover, I would like to specifically thank John Nees who was always a great on-time help in the lab providing immediate help and smart advice in our research.

I would like to thank my current and previous colleagues Dr. John Trey Ruppe, Hanzhang Pei, Siyun Chen, Dr. Tong Zhou, and Mathew Wittlesey. Accomplishing all these tasks might have not been possible without their help. Many times I worked closely with Dr. John Ruppe in the lab on different tasks. Hanzhang Pei was a great help especially in my last semester when I was busy with my dissertation, and helped me in measurements. I would like to specifically thank Dr. Qiang Du, and Dr. Yawei Yang from Lawrence Berkeley National Laboratory (LBNL) whom I worked with closely in many programing-oriented tasks.

Table of Contents

Dedication ii

Acknowledgements iii

List of Figures viii

Abstract xiii

Chapter 1 Introduction 1

1.1 Background 1

1.2 Time Domain Coherent Combining Techniques 2

1.2.1 Divided Pulse Amplification (DPA) 3

1.2.2 Stacking and Dump (SnD) 5

1.2.3 N^2 Coherent Combining 7

1.3 GTI Cavity Based Coherent Pulse Amplification (CPSA) 10

1.3.1 Concept of the CPSA technique 11

1.3.2 Coherent Pulse Stacking with a Single GTI Cavity 12

1.3.3 Amplitude Profile Requirements for the "Main" Pulse Sequence 15

1.3.4 Equal-Length GTI Stackers 17

1.3.5 Multiplexed-length GTI Stackers 18

1.3.6 Theoretical Description of N-GTI pulse stacker 20

1.4 Stacking Stabilization 22

1.5 Stacking Burst Amplitude and Phase Control for Achieving High Stacking Efficiency 22

1.6 Pathways to High Pre-Pulse Contrast 23

Chapter 2 Algorithmic and Haredware Basics of the Control System 25

2.1 Background 25

2.2 Concept and Definition of Stabilization in Control Theory 26

2.2.1 Survey of Stabilization Algorithms 28

1) Stochastic Parallel Gradient Descent (SPGD) Algorithm 28

2) LOCSET (self-referenced & self-synchronous) 36

3) Hänsch-Couillaud technique 38

4) A. D White Stabilization Technique: 39

5) 5) Pound Drever Hall (PDH) method for phase and frequency stabilization 40

2.3 Stabilization Systems Implementations 43

2.3.1 Analog Electronics 43

2.3.2 Software Based Implementation 44

2.3.3 FPGA Based Control System 47

Chapter 3 System Noise Characterisation Techniques 52

3.1 Phase Noise Measurement Technique Using a GTI Stacker 52

3.2 Time-Domain and Frequency-Domain Representations of System Noise 61

3.3 Example for Phase and Amplitude Noise Measurements 65

3.4 Appendix A: Sensitivity Analysis of the SHG profile to Different Number of Input Pulses 68

3.5 Appendix B: Sensitivity of the SHG profile to Different Number of Input Pulses 70

Chapter 4 Demonstration of Stable Stacking with Cascaded and Multiplexed GTI Configurations 73

4.1 Experimental Set-Up 73

4.2 Stacking Sensitivity to Cavity Phase, Pulse Phase and Signal Amplitude Errors 75
4.3 Oscillator Noise Characterization, analysis, and improvement results 80
4.4 Stacker Phase Space and Phase Drift Characteristics, and their effect on stacking stability 87
4.5 Stacker Stabilization Algorithm and its implementation 88
4.6 Stabilization Results for an Equal-Length 4-GTI Stacker Cascade 91
4.7 Stabilization Results for a Multiplexed-Length 4+4 GTI Stacker Configuration 92
Chapter 5 Optimization of the Stacked Pulse Fidelity 96
5.1 Background 96
5.2 Concept and Definition of Optimization 98
5.2.1 Survey of Optimization algorithms 99
1) SPGD 99
2) Genetic Algorithm (GA) 100
3) Simulated Annealing (SA) 101
4) Algorithm Of Pattern Extraction (Alopex) 101
5.3 Implementation of SPGD-Based Algorithm for Optimizing the Burst 102
5.4 Experimental Set-Up 106
5.5 Implementation of Genetic Algorithm for Optimization Purposes 107
Chapter 6 Conclusions and Future Work 119
6.1 Conclusion 119
6.2 Future Work 121
Bibliography 123

List of Figures

Figure 1.1: DPA principle DPA principle. The original pulse is divided into N copies of itself; the N pulses are amplified, and then recombined coherently to produce the final intense pulse [16]……...4

Figure 1.2: Experimental Set Up for DPA (PBS - polarizing beam splitter, HWP - half-wave plate, QWP - quarter wave plate)…….....5

Figure 1.3: working principle of SND enhancement cavity…….....6

Figure 1.4: a) The Concept of N^2 coherent combining b) The Time domain representation of N^2 coherent combing showing the input and output pulse sequences as well as their pulse energy coefficients [12]……...8

Figure 1.5: coherent pulse stacking amplification single fiber channel diagram……..11

Figure 1.6: a) impulse response of a single cavity (consisting the main and tail sequences) as well as the single pulse with unit amplitude that is input to the stacker b) the stacking burst profile which is the complex conjugate time reversal of the impulse response……13

Figure 1.7: Stacking profiles producing equal nonlinearity within the burst……16

Figure 1.8: M cascaded equal-length GTI cavities……17

Figure 1.9: stacking burst sequence with precisely prescribed amplitude profile for M equal-length GTI cavities…….18

Figure 1.10: M×M Multiplexed Different Round-Trip Length GTI Cavities……...19

Figure 1.11: stacking burst sequence profile for a multiplexed-length GTI stacker…….20

Figure 2.1: Typical closed loop configuration of a control system [49]……27

Figure 2.2: Hill-Climbing algorithm…… 30

Figure 2.3: Scheme of laser frequency stabilization using Hänsch-Couillaud technique [55]…38

Figure 2.4: (top) block diagram of the PDH stabilization scheme , (bottom left) intensity spectrum of the reflection coefficient for a Fabry-Perot cavity (bottom right) phase spectrum of the reflection coefficient for a Fabry-Perot cavity. [58,59]……...41

Figure 2.5: SPGD model in GTI based CPSA system……...42

Figure 2.6: Analog-Implementation for stabilizing N-cascaded GTI cavities……...43

Figure 2.7: Software-Based Implementation for stabilization of N GTI stacker system……...45

Figure 2.8: FPGA-Based Hardware Structure with Experimental Setup……..50

Figure 3.1: Time-frequency correspondence of the output from a femtosecond mode-locked laser……53

Figure 3.2: phase scan profile for measuring either GTI cavity phase noise or the Oscillator phase noise……...59

Figure 3.3: an example of the SHG drift signal that starts being measured right after the phase scan stops at point C……..60

Figure 3.4: Clustering the raw noise data for applying Allen Deviation process……..63

Figure 3.5: Different regions of the Allen Deviation plot…….64

Figure 3.6: a) scan profile of the GTI stacker cavity for more than 2π period b) Second Harmonic Generation (SHG) drift signal c) Normalized Allen Deviation Characteristics of the Amplitude Noise from the Oscillator. d) Allen Deviation Characteristics of the Stacking Phase noise in absolute mrad…….66

Figure 3.7: frequency spectrum of the SHG drift……66

Figure 3.8: a) SHG phase profile with 2 pulse b) SHG phase profile with 3 equal-amplitude pulses c) SHG phase profile with 3 non-equal amplitudes……69

Figure 3.9: Measurement results for the photodiode dark noise and the ADC quantization noise……...71

Figure 3.10: Signal-to-Noise (SNR) performance of the 1GHz ADC versus the peak-to-peak clock voltage at different input signal frequencies……72

Figure 4.1: Experimental Setup for stabilization of 4-Cascaded GTI stacker system using either the All-Software-based control system using fixed National Instrument hardware set-up or the fast FPGA control system……..74

Figure 4.2: Experimental Setup for stabilization of 4+4 Multiplex of two different-length Cascaded GTI stacker sets using the fast FPGA control system……...75

Figure 4.3: a) Pre-Pulse contrast versus cavity phase error for 4-Cascaded GTI cavity set. b) Peak Power Enhancement versus cavity phase error for 4-cascaded GTI cavity set……77

Figure 4.4: Pre-Pulse contrast versus pulse phase and amplitude errors for 4-Cascaded GTI cavity set……78

Figure 4.5: a) Pre-Pulse contrast versus cavity phase error for 4+4 Multiplexed GTI cavity set. b) Peak Power Enhancement versus cavity phase error for 4+4 Multiplexed GTI cavity set……79

Figure 4.6: Pre-Pulse contrast versus pulse phase and amplitude errors for 4+4 Multiplexed GTI cavity set……72

Figure 4.7: a) SHG drift using 2.7m cavity b) SHG drift using 30cm cavity c) Allen Deviation Characterization of the absolute stacking phase noise and comparison……82

Figure 4.8: Normalized Allen Deviation Comparison between the Short GTI Cavity Stacking Phase and the Amplitude Noise of the mode-locked Oscillator……84

Figure 4.9: Absolute Amplitude Noise of the Laser Diode with Various Drivers……85

Figure 4.10: Significant Improvement of the Stacking Phase Noise by noise reduction on the pumping side. Curves are the Allen Deviation Characteristics of the stacking phase noise using different-length GTI cavities before and after Noise improvement……...86

Figure 4.11: A two dimensional cavity phase landscape where the colors represents the strength of the peak-power metric (TPA or SHG). The simulated landscape covers a $4\pi \times 4\pi$ phase space for a 2 Cascaded GTI stacking case……...87

Figure 4.12: Algorithmic description of the Lissajous Local Search followed by the SPGD-based Algorithm for stabilizing the stacked pulse……...90

Figure 4.13: Simulation results showing the maximized and stabilized SHG signal associated with 4-cascaded GTI Stacking Stabilization……..91

Figure 4.14: Experimental results of 4 Cascaded 1ns-GTI cavities, time domain drift of the maximized metric, and stabilized stacked pulse……92

Figure 4.15: Block-diagram of the FPGA Control System along with the Stacker arrangement for 4+4 Multiplexed Stabilization Experiment……93

Figure 4.16: Simulation results for 4+4 Multiplexed Stacker System, Normalized Output Stacking Intensity Profile before and after stacking achieved……...94

Figure 4.17: Experimental results for 4+4 Multiplexed Stacker System, Normalized Output Stacked Profile before and after the stacking achieved…….....94

Figure 5.1: Representation of power contained in the pulses of the stacked profile……..…97

Figure 5.2: Flow-diagram of typical genetic algorithms for optimization purposes……...100

Figure 5.3: Block Diagram of the Control Algorithm for Stacker Stabilization and Pulse Profile Optimization……104

Figure 5.4: Experimental Setup for improving stacking fidelity…….106

Figure 5.5: Flow-Diagram for the Genetic Algorithm…….110

Figure 5.6: a) time-reversed impulse response as the input intensity profile with the largest 9 pulses b) Complex-conjugate phase of the impulse response as the input phase profile c) ideal stacked profile in linear scale d) ideal stacked profile in logarithmic scale……...111&112

Figure 5.7: A1) and A2) are the perturbed phase profile resulting in an SHG 20% off the peak and the corresponding stacked profile respectively. B1) and B2) are the perturbed phase profile resulting in an SHG 40% off the peak and the corresponding stacked profile respectively, C1) and C2) are the perturbed phase profile resulting in an SHG 57% off the peak and the corresponding stacked profile respectively…….113&114

Figure 5.8: SHG changes with respect to the perturbations specified by the standard deviation of the normal distribution…….115

Figure 5.9: a) SHG profile over 120 iterations for 50 different perturbation distributions (Genetic) b) SHG profile over 1000 iterations for 50 different perturbation distributions (SPGD) c) & d) corresponding linear-scale stacked profile associated with Genetic and SPGD algorithms respectively. e) & f) corresponding logarithmic-scale stacked profile associated with Genetic and SPGD algorithms

respectively…….115&116

Figure 5.10: a) Converged SHG value for different runs (SPGD) b) Final Stacked Pulse for different runs (SPGD) c) Converged SHG value for different runs (GENETIC) d) Final Stacked Pulse for different runs (GENETIC)……...117&118

Abstract

Coherent Pulse Stacking Amplification (CPSA) is a new time-domain coherent addition technique that overcomes the limitations on pulse energies achievable from optical amplifiers. It uses reflecting resonators to transform a sequence of phase- and amplitude-modulated optical pulses into a single output pulse enabling high pulse energy for fiber lasers.

This thesis focuses on utilizing efficient algorithms for stabilization and optimization aspects of CPSA and developing a robust, scalable, and distributed digital control system with firmware and software integration for algorithms, to support the CPS (Coherent Pulse Stacking) application. We have presented the theoretical foundation of the stochastic parallel gradient descent (SPGD) for phase stabilization, discussed its performance criteria, its convergence, and its stability. We have presented our software and hardware development for time-domain coherent combing stabilization (specifically, an FPGA (Field Programmable Gate Array)-based Control system with software/firmware development to support stabilization and optimization algorithms). Analytical formulations of output stacked pulse profile as a function of input pulse train amplitudes and phase and stacker cavity parameters have been derived so as to build up a foundation for a GTI (Gires-Tournois-Interferometer) Cavity-based noise measurement technique. Time-domain and frequency domain characterization techniques have been presented to analyze phase and amplitude noise in the stacking system. Stacking sensitivity to errors in different control parameters (stacker cavity phase, pulse amplitude, and phases) for different stacker configurations have been analyzed. Noise measurement results using GTI cavities with different round-trip time has have been presented and we have shown how effectively the stacking phase noise in the system

can be reduced by improving the noise performance of the mode-locked oscillator. Simulation and Experimental results for stabilizing different stacker configurations have been presented. Finally an algorithmic control system along with software/hardware development for optimizing amplitudes and phases of the input burst has been implemented to increase stacking fidelity. A complete detailed description, and simulation of the Genetic Algorithm as an alternative algorithm for optimizing the stacked pulse fidelity has been presented. Comparison between SPGD and Genetic Algorithm results has been done to evaluate their performance.

To summarize, this thesis provides theoretical, experimental, and implementation aspects of controlling CPSA system by introducing efficient control algorithms and developing a turn-key digital control system which is scalable to large number of stacker cavities.

Chapter 1 Introduction

1.1 Background

Ultrashort-pulse laser sources, or equivalently, ultrafast laser sources which output picosecond to hundreds of femtosecond long pulses are widely used for many applications such as acceleration of particles, laser cutting, biomedical engineering, etc. [1,2].

Of particular interest are high energy ultrashort pulses, which can reach peak powers in the range from TW (10^{12}W) to multiple PW (>10^{15}W), which have enabled entirely new areas in ultrafast science and technology based on laser-matter interactions in the relativistic intensity regime. Achieving such high peak powers is only possible via the use of optical amplification, necessary to boost the energy of mode-locked laser oscillator seed sources from approximately nanojoules to more than a Joule (and up to 10s and 100's of Joules) .

In 1985, Donna STRICKLAND and Gerard MOUROU invented a new technique called chirped pulse amplification (CPA), which enabled achievement of these high pulse energies and peak powers. They showed that by first stretching a chirped optical pulse, then amplifying, and finally compressing, very high laser peak powers could be achieved. Focusing such high peak power pulses to a diffraction-limited spot led to the demonstration of record-breaking peak intensities of $10^{22}\ W/cm^2$ in 2004 [3]. It was the CPA technique that had enabled the rapid development of ultra-intense and ultra-short lasers, and had led to the development of extremely high-field ultrafast science, which creates extreme physical conditions using relatively compact laboratory-scale facilities. In this approach, ultrashort pulses on the order of 10's of femtoseconds

need first to be stretched out to about a nanosecond. This, in turn, reduces the peak power in the laser amplifier, and lowers the significant nonlinear effects in the amplifier. After the amplification stage, pulse lengths are compressed back to the femtosecond domain. As a result, chirped pulse amplification effectively increases the pulse energy by about 4 to 5 orders of magnitude. In the majority of solid-state laser amplifiers (e.g. Ti:sapphire) the amplified pulse energy can be further increased by another ~2 orders of magnitude by correspondingly increasing the transverse aperture size, thus allowing a complete stored-energy extraction with minimal nonlinearities. For example, energies of 100s of Joules can be achieved in TW-PW Ti:sapphire CPA systems using transverse apertures as large as 150mm in diameter [4]. Scaling up the transverse aperture size to get the maximum extracted energy out of the stored energy suffers from limitations for some laser amplifiers such as fiber amplifiers. For the case of single mode (SM) operation, the core size usually needs to be less than 100um in diameter [5].As an example, single mode operation of a photonic crystal Large Mode Area (LMA) fiber with core size of larger than 50um has been reported in [6]. However, operating with largest diffraction-grating-based pulse stretchers and compressors for implementing CPA is not sufficient to completely extract the stored energy which in most of cases is nearly 1% of the stored energy. (<1mJ for SM operation).

1.2 Time Domain Coherent Combining Techniques

As indicated in the previous section, fiber CPA can extract only ~1% of the stored energy. For high energy applications, one needs parallel combination of channels to achieve required energy per pulses (Notice that solid state laser amplifier such as Ti:sapphire with large transverse aperture size are not discussed here). For example, a 10GeV acceleration stage [2] would require 10s of Joules per pulse. However, each amplification channel in the standard CPA allows 10^{-4} to 10^{-3}

Joules meaning that the acceleration stage requires parallel combination of 10^4 to 10^5 amplification channels to satisfy the energy condition, which is quite a technical challenge. To overcome the challenge one can amplify much longer pulses (effectively beyond 1ns) instead. This will boost the achieved pulse energies closer to the stored energies in the amplifier. However, there are no known practical dispersion-based techniques of extending stretched pulse duration to significantly beyond 1 ns. Therefore, it is necessary to look beyond dispersion based pulse stretching. One broad approach to increase pulse duration is to use time-domain pulse combining, in which multiple stretched pulses would be amplified in a burst, and then combined into a single pulse at the system output. This thesis is devoted to the development of certain control aspects of such a time-domain pulse combining technique, called coherent pulse stacking amplification (CPSA). In the remainder of this introductory chapter we will first review the other demonstrated time-domain pulse combining techniques, such as divided pulse amplification (DPA) [8,9], Stacking and Dumping (SND), and N^2 coherent combining, and then describe the CPSA approach.

1.2.1 Divided Pulse Amplification (DPA)

DPA is a time domain coherent combining technique, which is based on first spatially splitting the pulses, amplifying, then spatially recombining the pulses after the amplification. (see Fig. 1.1). The technique starts with spatially arranging N delay lines in which the initial pulse is divided into N pulses that are temporally delayed with respect to each other. Next, this pulse train is amplified. Finally the pulse train goes through another delay-line setup where the delays are removed, and a single pulse is obtained after the copied pulses interfere with each other. [16,17].

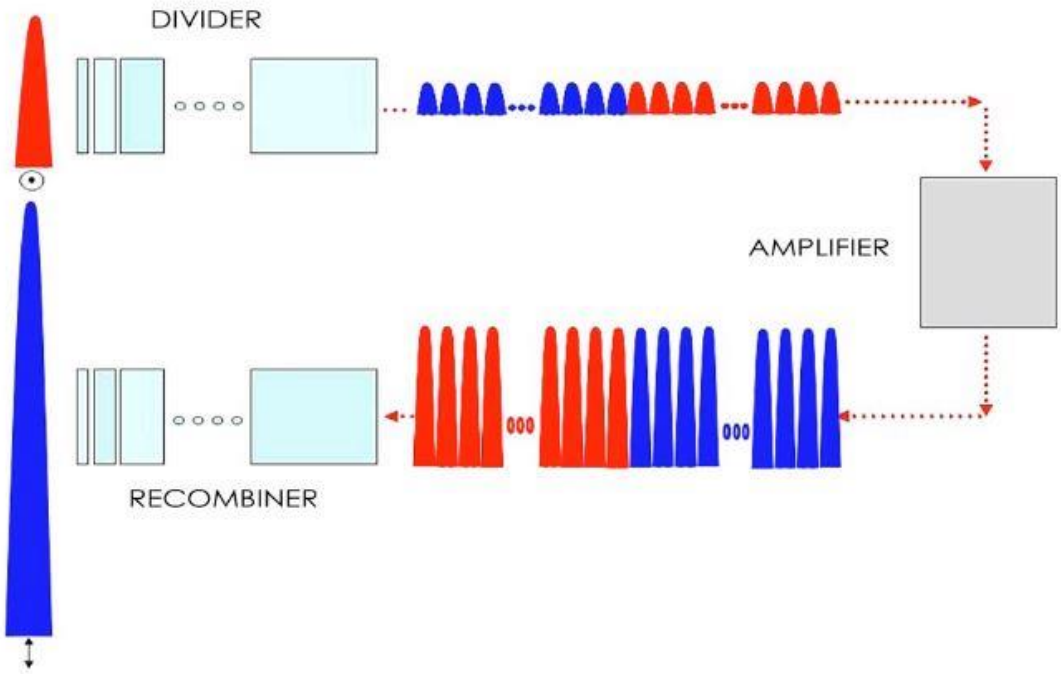

Figure 1.1: DPA principle DPA principle. The original pulse is divided into N copies of itself; the N pulses are amplified, and then recombined coherently to produce the final intense pulse [16]

Figure 1.2 shows a typical experimental DPA System. A single low energy pulse is divided into a number of pulses with different polarizations utilizing a number of delay lines, PBS (Polarizing Beam Splitters) and HWPs (Half-Wave Plates). As stated before, the delayed pulses are then amplified and finally turn into a single intense pulse utilizing a similar setup of delay lines, PBS and HWPs. As shown in figure 1.2 for this specific example, there are 2 different delay lines in the division stage of the DPA implementation in which each line produces two copies (total 4 pulse copies). The delay of the two lines are different namely τ_1 and τ_2. The two HWPs before and after the PBS in the division stage are used to shape the amplified pulse train for saturation compensation.

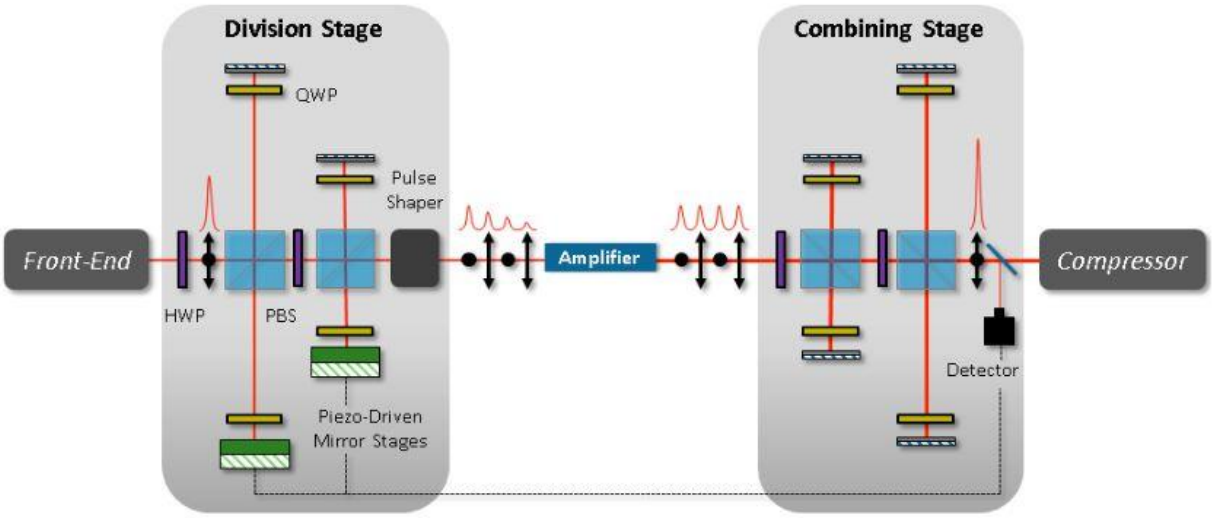

Figure 1.2: Experimental Set Up for DPA (PBS - polarizing beam splitter, HWP - half-wave plate, QWP - quarter wave plate) [17]

Therefore, the DPA technique (as any time-domain combining technique) allows one to increase the amplified pulse energy by approximately the factor *N* equal to the number of pulse replicas. This technique is also simpler to implement compared to the chirped pulse amplification technique discussed previously in the sense that it utilizes only one amplification stage.

If the number of delay lines goes beyond 2 or 4 or more, the existing combination of HWPs and pulse shapers would not provide sufficient degrees of freedom to accordingly shape the input burst to compensate for saturation. This is a major challenge since one need always to accurately carve out the input amplitude profile to minimize the nonlinearity in and after the amplification stage.

1.2.2 Stack-and-Dump (SnD)

The experimental setup for this technique is made of a high-finesse optical cavity, for storing the stacked pulses, and an active element such as a rotating-mirror or an AOM (Acousto-Optic-Modulator) for extracting or dumping the stored pulses [10,11]. As an alternative to the DPA technique, the stacking and dump (SND) avoids the creation of temporal replicas, by

amplifying a pulse train at a high repetition rate, storing them in a high-finesse optical cavity (i.e. enhancement cavity - EC) as a single circulating pulse, and then periodically extracting this circulating pulse using a sufficiently fast optical switch [18,19].

Figure 1.3 shows a typical experimental set-up for SnD technique. In this experimental setup the pulse train from the mode-locked oscillator with repetition rate f_{rep} is first stacked in a high-finesse optical cavity (e.g. EC) to enhance the power. Next, the stored stacked pulses are extracted or dumped by the implemented switch. Assuming that N pulses are stacked in the EC, the switch needs to operate at $\frac{f_{rep}}{N}$ to accurately and periodically extract out the circulating stacked pulse. It can be further shown that the pulse energy linearly increases by the number of stacked pulses [18]. It is also important for the switching to function fast enough so that it can dump the circulating stacked pulse out of the EC between the successive pulses.

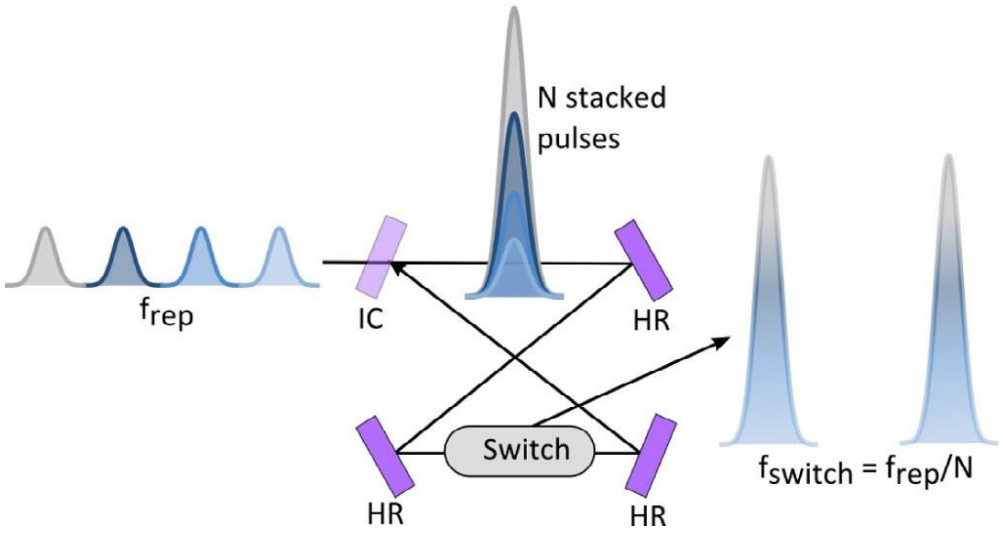

Figure 1.3: working principle of SnD enhancement cavity

This technique suffers from pulse energy limitations and stability constrains. All existing SnD experimental setups use AOMs for the switching part which will ultimately limit the maximum energy storage due to the insertion loss of the modulator and the trade-off between speed

and damage threshold/strong nonlinearity due to the small spot size, which is necessary to achieve sufficiently short rise time. Beam size is the key factor for damage considerations where increasing the beam size will accordingly reduce the energy density and hence reducing the risk of damaging the AOM. For example, a beam diameter of larger than 1cm will keep the energy density below the $10J/cm^2$ threshold for achieving 10J for 1ns pulses [20]. This range of beam size will result in very large round-trip length of the enhancement cavity which would be technically challenging. As an example, a beam diameter of larger than 1cm for a SiO2-based AOM corresponds to 1us rise time for the AOM, and 300m round-trip length for the optical cavity.

Insertion loss in the modulator as mentioned before also limits the maximum number of stacked pulses inside the EC and hence the maximum energy storage. To resolve this, an all-reflective mechanical rotating mirror could be implemented for the switching part which is also experimentally difficult [18].

1.2.3 N^2 Coherent Combining

The third published time-domain technique is N^2 coherent array combining. This technique is utilized to boost the pulse energy extraction corresponding to each individual amplification channel in a coherently combined array [12]. This approach is realized and analyzed in both temporal and spatial domains. As is further visually shown, N^2 coherent combing boosts the output pulse energy proportional to N^2, which is the key benefit of this technique compared to other conventional combining approaches. This is due to the reduction of repetition rate by a factor of N after coherently combing N channels. The average power in this technique also linearly increases by the number of combined channels which is the same in other conventional combining systems.

This N^2factor in pulse energy increase indicates that one can achieve same pulse energies with smaller number of combined channels combined to the previous conventional combining approaches.

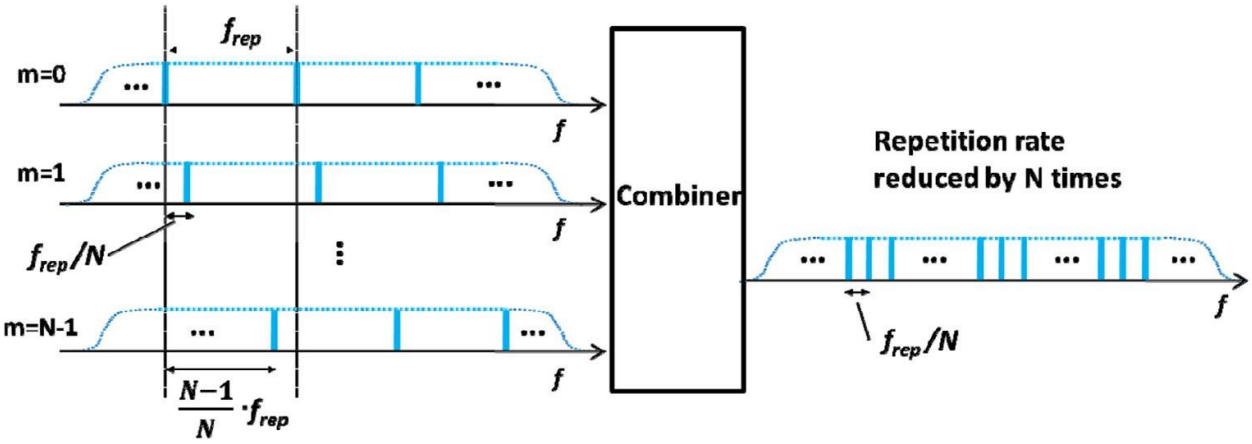

a)

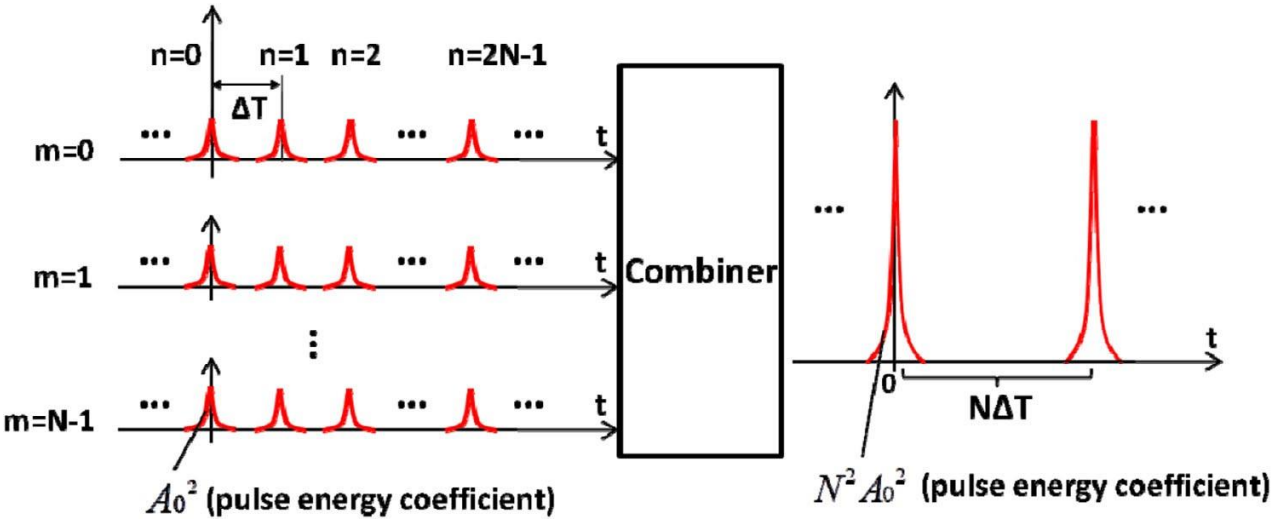

b)

Figure 1.4: a) The Concept of N^2 coherent combining b) The Time domain representation of N^2 coherent combing showing the input and output pulse sequences as well as their pulse energy coefficients [12]

Figure 1.4 a) shows the concept of N^2 coherent combining in frequency domain. There are N parallel channels or N periodic pulse trains in the input stage that are coherently combined into a pulse train with an effective repetition rate N times lower than the input repetition rate f_{rep}. The

combining elements in this approach are a sequence of Fabry-Perot-Interferometers (FPI)s. It is important to point out that repetition rate for all N parallel channels is the same and equal to f_{rep}. The frequency spectrum for these parallel channels is a frequency comb in which the comb teeth are separated by f_{rep} and the pulse envelope is the same for all the channels. The only difference is that the comb teeth in the m^{th} channel ($1 \leq m \leq N-1$) are shifted by $\frac{m}{N} f_{rep}$ (e.g the last pulse train's spectrum is shifted by $\frac{N-1}{N} f_{rep}$). This indicates that the comb teeth in two consecutive pulse trains are shifted by $\frac{f_{rep}}{N}$ with respect to each other. Now if a linear combiner adds these channels together the resulting output pulse train will have a frequency spectrum with the same envelope but the comb teeth are separated by $\frac{f_{rep}}{N}$. This is the important conclusion indicating that the output pulse energy in N^2 coherent combining technique which is the average power divided by the output repetition rate is approximately N^2 times the input pulse energy. (Notice that the average power in this technique is approximately increased by a factor of N as in any other combining approach). In the time domain, as shown in 1.4 b) the output train consists of pulses with a period of N times lower than the period of the input pulse [12].

The issue we have in N^2 coherent combing is that having short FPIs as the combining elements is at the cost of high starting repetition rates which is not compatible with high energy applications. Still this technique is valuable for high repetition rate operation, but in order to significantly reduce the repetition rate to the desired degree one would need a very large number of cavities and channels, beyond what is practical. An additional minor technical issue is the need to combine two beams with each cavity, whereas in the CPSA technique there is only one input beam into each GTI cavity stacker, which is much simpler to implement.

1.3 GTI Cavity Based Coherent Pulse Stacking Amplification (CPSA)

The research of this thesis was focused on developing key control-system aspects (specifically –algorithms, software and hardware for time-domain coherent combining stabilization, and algorithm-based stacked-pulse fidelity optimization) of the new technique, called coherent pulse stacking Amplification (CPSA). As has been proved in [22] in details, CPSA is the best candidate among all the published combining techniques that enable achievement of maximum pulse energies and at the same time do not suffer from the limitations mentioned in the previous techniques. In this approach, an input burst of pulses that have been modulated both in their phases and amplitudes is transmitted through a number of GTI (Gires-Tournois-Interferometer) cavities as optical resonators. These resonators then temporally and coherently stack the pulses and transform them into a single intense stacked pulse at the output under specific conditions. Different stacking scenarios have been demonstrated in either cascading or multiplexed configurations (which will be further explained in detail through this chapter) including stacking of 81 pulses for high energies. This approach proved successful in achieving high energy pulses from the initial ultrashort femtosecond long pulses by completely extracting the stored energy in a yb-doped fiber laser system. In the following sections we describe the CPSA concept and its key design and performance characteristics in more detail. Since the development of the theoretical aspect of the CPSA technique was not the subject of this thesis, this will be only a review of key theoretical results that were obtained in [22].

1.3.1 Concept of the CPSA technique

The conceptual outline of the CPSA technique is shown in the figure 1.5. Note that the specific pulse repetition rates and pulse energies indicated in the figure 1.5 are intended only as a representative example, not as a general CPSA system description.

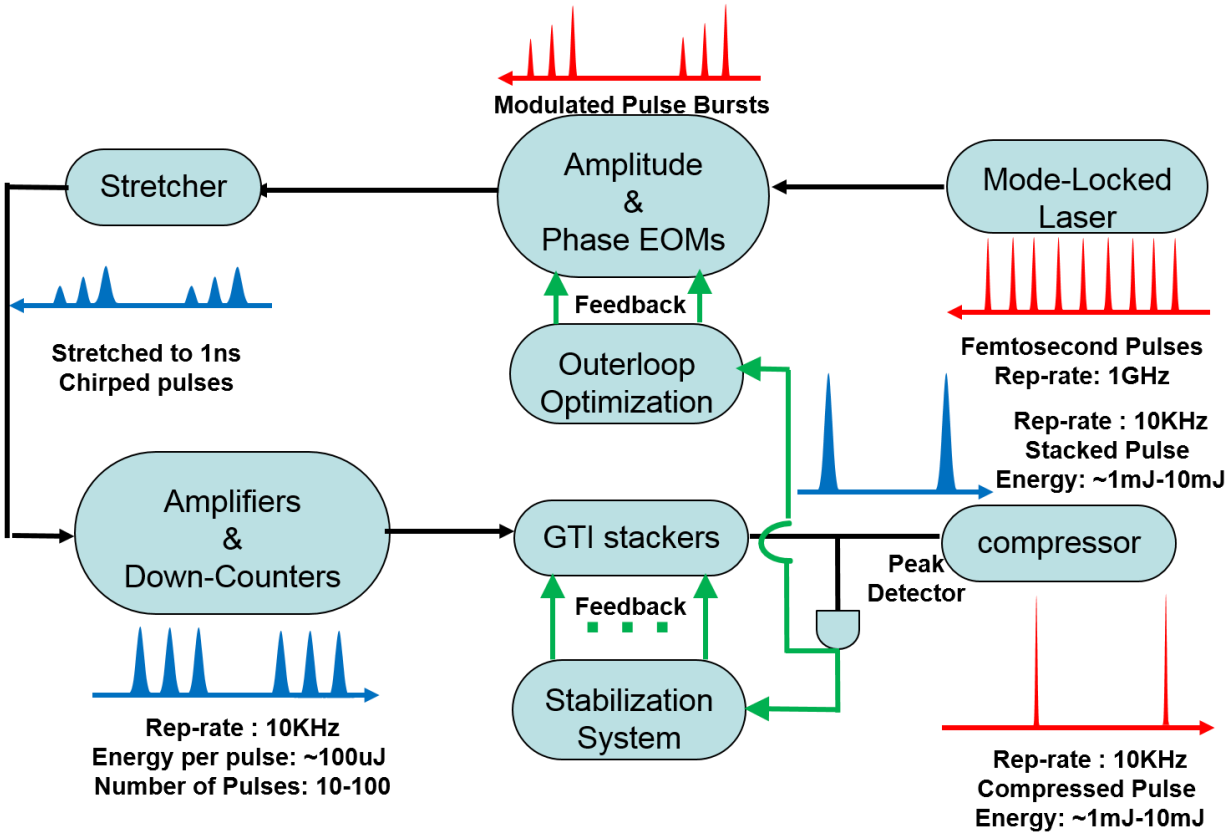

Figure 1.5: coherent pulse stacking amplification single fiber channel diagram

As shown in figure 1.5, The CPSA experimental setup starts with a mode-locked oscillator operating at repetition rate of 1GHz (~988.7MHz) generating bursts of ultrashort femtosecond pulses which are then modulated both in their phase and amplitude using integrated Electro-Optic-Modulators (EOMs) operating with bandwidths from 1GHz to 10GHz. Proper modulation for phases and amplitudes are important to make it possible for the pulse burst to be stacked after going through the free-space resonators. Due to the fact that different pulses experience different

gain values during amplification stage (~ the front pulse gets highest and the last one gets the lowest gain), this amplitude profile should be carved out accordingly to minimize the output nonlinearity which needs to be always taken care of. Next the pulses go into the stretching stage to be stretched to nanosecond duration and then amplified in the subsequent amplifiers. At this stage, the pulse burst is transmitted through a number of free-space GTI interferometers to achieve stacking. These optical resonators need to be controlled in terms of their round-trip length or phase and stabilized to achieve stacking. They can be scaled to larger numbers for higher energy and average power experiments as well. An advantage of this setup is that only a few numbers of these optical cavities in a specific spatial configuration can lead to stacking of up to 100 pulses.

1.3.2 Coherent Pulse Stacking with a Single GTI Cavity

In coherent pulse stacking amplification (CPSA) a sequence of pulses from the mode-locked oscillator at GHz repetition rate is coherently added together in the time-domain and being stacked into a single intense pulse at the output utilizing resonant reflecting interferometers. This resonant reflecting interferometer is basically a variant of Fabry-Perot interferometer consisting of one partially reflecting mirror which is usually called as Gires-Tournois-Interferometer (GTI). A travelling-wave GTI cavity is able to spatially separate the input optical beam and the reflected beam. For the CPSA scheme to function, the cavity roundtrip time must be an integer number of the laser-oscillator cavity roundtrip periods, plus a certain fraction of the pulse-train carrier-wave optical cycle [13], which defines an individually-prescribed phase shift associated with each individual GTI in the stacker.

In order to explain how the pulse stacking works, let us first consider stacking with a single GTI cavity [13]. Such a single-GTI stacker has a roundtrip length L equal to that of the mode-

locked oscillator seed of the system and is characterized by its front-mirror reflectivity R and its roundtrip phase ϕ for the carrier wave (cavity phase).

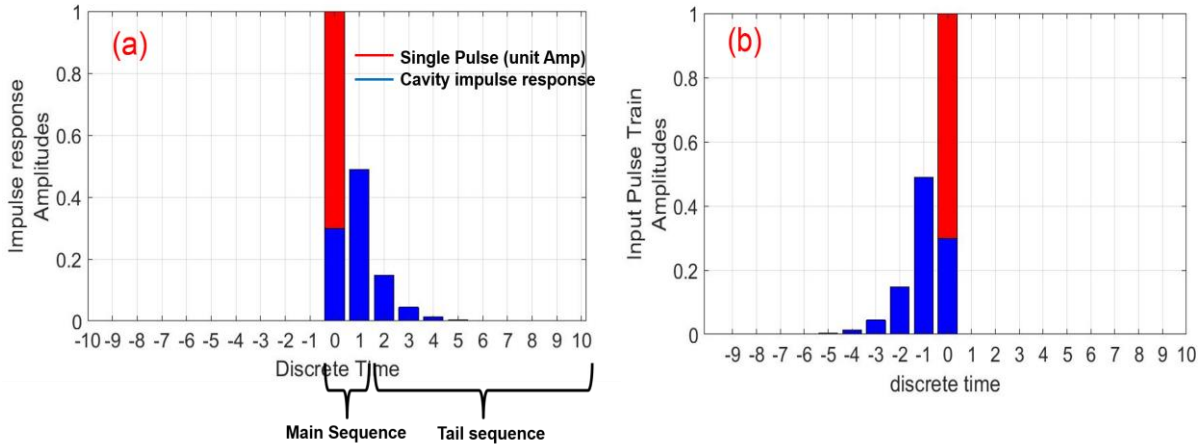

Figure 1.6: a) impulse response of a single cavity (consisting the main and tail sequences) as well as the single pulse with unit amplitude that is input to the stacker b) the stacking burst profile which is the complex conjugate time reversal of the impulse response

If the GTI is lossless (i.e. it's cavity-folding mirrors have perfect 100% reflectivity and the beam splitter has no absorption), then it is a linear and time-reversible system. In practice, there will be some small losses associated with each cavity-folding mirror, but they should be negligibly small, and the time- reversibility should be preserved to a high degree. This reversibility makes it convenient to consider this GTI stacker in reverse: i.e. consider its response to a single input pulse. Because a lossless GTI reflects all the incident optical power, a single input pulse at the GTI input will produce a sequence of pulses at its output. Analytically this can be calculated using the equation 3.4 from the chapter 3, which indicates that the sequence will consist of two "main" pulses at the beginning, followed up by a rapidly (as a geometrical progression) decaying "tail", as illustrated in the figure 1.6 (a). The relative amplitudes of the two "main" pulses is determined by the front-mirror reflectivity $r = \sqrt{R}$. Equation 3.4 also indicates that there will be certain phases

imprinted on each of the pulses. Time reversing this sequence (which means reversing the order of the pulses and complex conjugating pulse phases) produces a stacking burst (illustrated in figure 1.6(b)), which, when launched into this single-GTI stacker, should produce a single stacked pulse at the output.

As evident from the equation 3.4, stacking-burst pulse phases are primarily determined by the stacking condition, which requires that the last pulse in the stacking burst should be out of phase with the rest of the pulses in the burst. However, there will be also an additional phase added to each pulse, which is determined by the GTI roundtrip phase ϕ. Imprinting this "total" phase (i.e. required by stacking condition + GTI cavity roundtrip) on the stacking burst is achieved with the phase EOM, and the correct amplitudes - with the amplitude EOM, as shown in figure 1.5.

This analysis of a single-GTI stacking highlights key aspects of a stacker design: choosing front-mirror reflection coefficient r determines the shape of the "main" pulse sequence, in this simplest case consisting of two pulses, and choosing GTI cavity round-trip phase ϕ affects the phase modulation profile at the system input. As we discuss in greater detail later, this can be generalized to a general stacking arrangement consisting of M GTI cavities: a sequence of M of GTIs has 2M degrees of freedom (only 2M-1 are independent), and it can be shown that these degrees of freedom can be optimized to stack approximately 2M pulses (i.e. $2M \pm 1$) with a precisely prescribed amplitude profile [13].

Furthermore, this single-GTI example also highlights key features of the stacking burst, as well as the stacker design strategy. The stacking burst contains the "main" pulse sequence with approximately 2M pulses, whose amplitude profile can be precisely tailored by finding suitable M cavity reflection coefficients and M -1 cavity round-trip phases. It also contains the "tail" pulse sequence. The important design aspect for a general M – GTI stacker is that the choice of the all

M front-mirror reflection coefficients and the cavity round-trip phases is completely defined by the desired amplitude profile of the "main" pulse burst, while the amplitude profile of the "tail" sequence, as well as the phases of all the pulses in the burst, are merely the result of this stacker-parameter choice.

1.3.3 Amplitude Profile Requirements for the “Main” Pulse Sequence

At this point it is necessary to consider the general requirements placed on the amplitude profile of the main stacking-burst sequence, which are visualized in the figure 1.7. Since the CPSA technique is used in addition to the CPA technique, each pulse in the stacking burst is a stretched (approximately 1 ns) pulse. Therefore, the length/duration of the main sequence will be completely determined by the number of pulses in that sequence, assuming an optimal arrangement in which all the pulses are immediately adjacent to each other in the burst. The choice of the duration of the stacking-burst main sequence is determined by the need to achieve sufficiently low nonlinearity in the last amplification stages, which generally means longer bursts will be required for achieving higher pulse energies. From the early discussion in this chapter it is clear that in order to extract all stored energy it is necessary to use pulse-burst lengths on the order of approximately 100 ns.

Furthermore, CPSA is uniquely different from the CPA in that it can reach a nearly complete stored-energy extraction from a yb-doped fiber amplifier. This means that there will be very strong distortions in the profile of the final amplified pulse burst [22]. It is one of the principal advantages of the CPSA technique that it allows one to completely control the shape of this burst. As shown in [22], the amplified burst shape is optimally defined by the requirement that equal nonlinearity would be produced at every point in this amplified burst. As it happens, this optimal profile also minimizes the induced nonlinearity. The analytical expression for this optimal profile can be found in the reference [22]. One important result, however is that this optimal amplified-

burst shape strongly depends on the degree of energy extraction. As illustrated in the figure 1.7, at low energy extraction the required burst shape is nearly flattop, but it becomes a strongly decaying profile as the degree of energy extraction increases toward full stored-energy extraction. Again, it is the principal advantage of the CPSA technique that it can accommodate this varying stacking-burst shape and is thus fully compatible which strongly saturated amplification at the limit of near-complete energy extraction.

Finally, the last additional requirement is that this main stacking-burst profile be smooth, to within approximately +-1% (as determined by the numerical simulations), in order to avoid adding detrimental nonlinearity-produced phases to each of the pulse of the stacking burst.

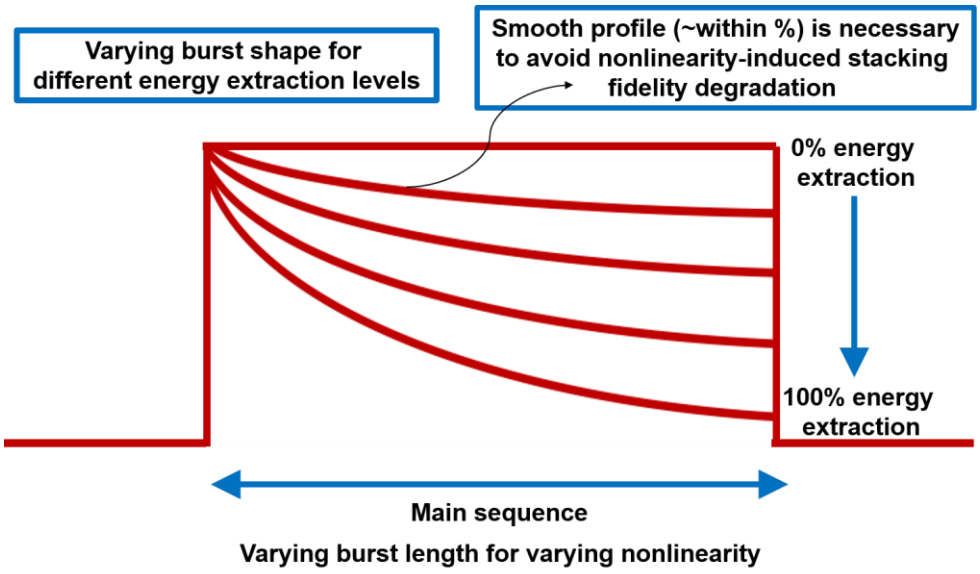

Figure 1.7: Stacking profiles producing equal nonlinearity within the burst

1.3.4 Equal-Length GTI Stackers

From what was described earlier it follows directly that using M equal-length GTI cavities (Fig. 1.8) it is always possible to stack 2M pulses in the main stacking-burst sequence with precisely prescribed amplitude profile (see the illustration in Fig. 1.9). As was discussed in the preceding section, this profile has to be smooth, of certain optimum shape, and sufficiently long to achieve sufficiently low linearity in the last amplification stages. Since in order to extract fully the stored energy, it is necessary to use approximately 100 pulses in the main stacking sequence, it follows that this would require approximately 50 equal-length GTI cavities. Such large number of the stacking cavities does not appear to be practically appealing. Fortunately, this practical challenge can be overcome by using multiplexed-length GTI stacker configurations described in the next section.

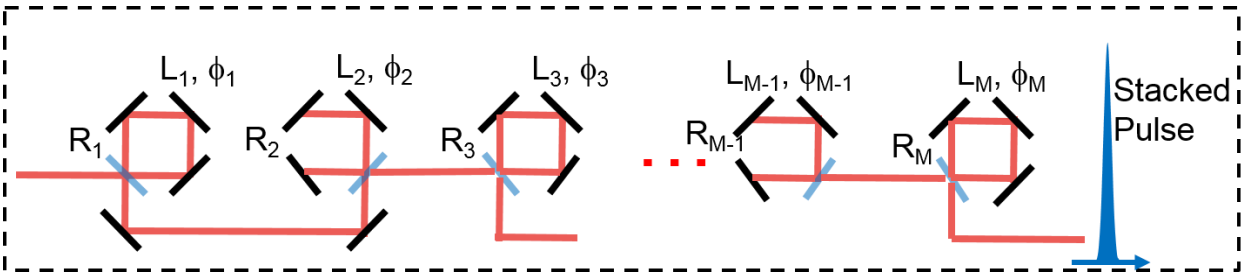

Figure 1.8: M cascaded equal-length GTI cavities

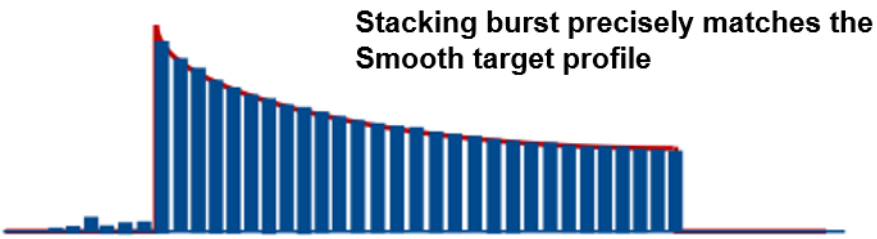

Figure 1.9: stacking burst sequence with precisely prescribed amplitude profile for M equal-length GTI cavities

1.3.5 Multiplexed-length GTI Stackers

Detailed description of how the multiplexed-length GTI stacker works, and how it is designed goes beyond the research topics of this thesis. It is sufficient to state at this point that, as it has been proven in [22], using multiplexed-length stacking arrangements it is possible to stack a very large number of pulses in the main stacking-burst sequence with very few stacking cavities.

Instead of considering a general case, let's consider a conceptually much simpler case of two identical-design equal-length cascades, each consisting of M GTI cavities, but one cascade having the round-trip GTI-lengths equal to that of the mode-locked seed oscillator, and another having 2M (M is the number of GTIs per set) times longer round-trip GTI-lengths (see Fig. 1.10).

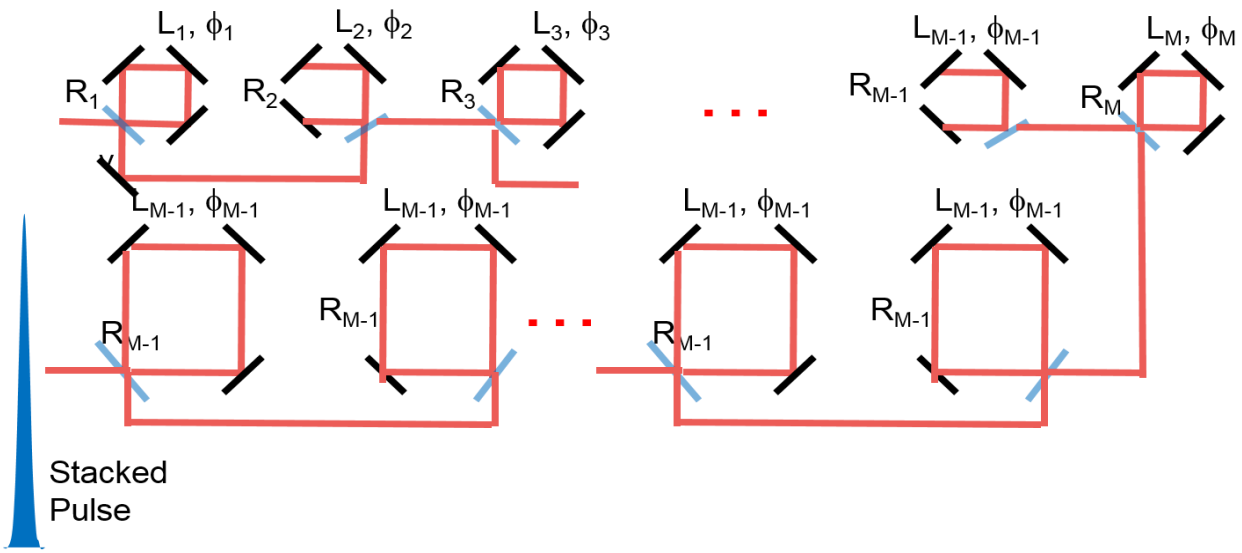

Figure 1.10: M+M Multiplexed Different Round-Trip Length GTI Cavities

Here the Multiplexed configuration is analyzed in terms of the pulse bursts. First a burst of approximately $(2M)^2$ pulses with a time-separation of T enters the first set of M-cascaded cavities. This burst is then transformed into a burst of $2M$ pulses but with a time-separation of $(2M) * T$. Second this burst of $2M$ pulses enters the second set of M-cascaded cavities and transforms into a single stacked pulse at the final output. The peak power for the final stacked pulse is $(2M)^2$ times larger than the peak power in the incident pulse burst. Therefore, a large number of pulses can be stacked using only a few GTI stackers. For example, in the experiments carried out in this work, we typically used 4 + 4 multiplexed configuration consisting of 8 cavities, but capable of stacking up to 81 pulses in the main sequence. (Notice that $(2M)^2$ is an approximate number. For instance, for the case of M=4, $(2M+1)^2 = 81$ pulses can be stacked).

However, as is shown in [22], the price one has to pay is that in general it is no longer possible to precisely match any desired and smooth main stacking-burst sequence profile – it is only possible to approximate this desired profile. This means that in general (i.e. except some very rear special cases) the main stacking-burst sequence profile is not smooth, as illustrated in the figure 1.11. Nevertheless, we have recently shown that this limitation of multiplexed-length

GTI stackers can be overcome by accepting a certain trade-off. While it is not possible to achieve a single stacked pulse with any desired smooth main sequence profile, it is possible to achieve efficient stacking with some negligible post-pulses after the main stacked pulse. Detailed explanation of this, however, goes beyond the subject matter of this thesis.

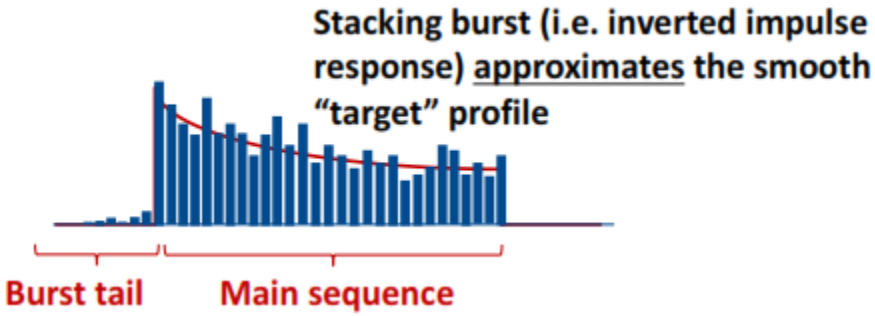

Figure 1.11: stacking burst sequence profile for a multiplexed-length GTI stacker

1.3.6 Theoretical Description of N-GTI pulse stacker

For completeness we include here a summary of a theoretical description of coherent pulses stacking technique. In general, a sequence of GTI cavities can be described by linear time invariant (LTI) system theory [23] and such an LTI system is characterized by its impulse response (i.e. its response to a single unit amplitude pulse). Since the M-GTI stacking system is an LTI system, it can be characterized by the product of individual responses of each cavity as follows:

$$F(\omega)_M = \prod_{k=1}^{M} F_k(\omega) \tag{1.1}$$

the transfer function $F_i(\omega)$ of such a cavity can be written as follows [24]:

$$F_k(\omega) = \frac{e^{i\omega T_r}\sqrt{R_k} - e^{i\phi_k}}{e^{i\omega T_r} - \sqrt{R_k}e^{i\phi_k}} \tag{1.2}$$

Where R_k is the front mirror reflectivity of the kth cavity, and ϕ_k is the round-trip phase of the kth cavity, and T_r is the round-trip time of each cavity.

Considering a single unit-amplitude pulse $p_s(t)$ which is transmitted into an M-GTI stacker, this incident pulse will produce a pulse burst at the output which represents the continuous time impulse response $h(t)$ as follows:

$$h(t) = \sum_{n=0}^{\infty} \tilde{h}[n].\, p_s(t - n.T_r) \tag{1.3}$$

The formula above represents $h(t)$ as a summation of equal amplitude pulses $p_s(t - n.T_r)$ each characterized by $h[n]$ (the discrete time impulse response) that accounts for amplitude and phases of each pulse. After a few steps in mathematical manipulation one can show that the frequency response of the M-GTI stacker system can be related to the discrete time impulse response as follows:

$$F(\omega)_M = \sum_{n=0}^{\infty} \tilde{h}[n].\, e^{-i\omega n T_r} = \sum_{n=0}^{\infty} \tilde{h}[n].\, e^{-i\Omega n} \tag{1.4}$$

$$h[k] = \frac{\omega}{2\pi} \int_0^{2\pi} \prod_{i=1}^{N} F_i(\omega) e^{j\omega T_r k} d\omega \tag{1.5}$$

Where $\Omega = \omega T_r$.

After the input pulse train propagates through the M-GTI stacker system, the response of the stackers $\tilde{A}^{out}[n]$ to the input pulse train can be calculated as the convolution sum between the input pulse sequence and the stackers discrete time impulse response as follows:

$$\tilde{A}^{out}[n] = \tilde{A}^{in}[n] * \tilde{h}[n] = \sum_{k=-\infty}^{\infty} \tilde{A}^{in}[k].\, \tilde{h}[n-k] = \sum_{k=-\infty}^{n} \tilde{A}^{in}[k].\, \tilde{h}[n-k] \tag{1.6}$$

The upper bound of the summation is limited by n due to the causality of the impulse response of the M-GTI stacker system. Using this impulse response, the response of the system to any arbitrary input pulse sequence can be calculated as the convolution of the impulse response and that input pulse train. The M-GTI stacker response $\tilde{h}[k]$ which is obtained by solving equation

(1.6) is characterized by the round-trip phase of each cavity and the reflectivities of the partially-reflective front mirror in each cavity as stated in equations (1.2).

1.4 Stacking Stabilization

As described in the section 1.3, coherent pulse stacking is a time-domain coherent combining technique. Therefore, in order to achieve coherent stacking at the output, it is necessary to "actively" control the round-trip length of the GTI cavities and lock them to each prescribed cavity phase ϕ with a tolerance of a fraction of wavelength, as described by the equations (1.2) and (1.5) in section 1.3.3 where the round-trip phase and reflectivity of each cavities are determined once the impulse response $h(t)$ of the M-GTI stacker system is obtained. Stabilizing cavity requires active stabilization using feedback control systems. This stabilization has been one of the key tasks accomplished by this thesis work and is described in greater detail in chapters 2 and 4.

1.5 GTI Stacking Burst Amplitude and Phase Control for Achieving High Stacking Efficiency

One of the key advantages offered by the CPSA technique is the many degrees of freedom of the control that are available. This becomes particularly relevant when considering the many uncertainties present in the system. First of all, the recipe for the stacking-burst profile both in terms of amplitude and pulse phases cannot be known with absolute accuracy. This is due to the fact that front-mirror reflection coefficients of each GTI cavity cannot be defined with the accuracy of better than approximately 1%. Furthermore, even if this recipe were known precisely, it is nearly impossible in practice to imprint it with an absolute accuracy using electro-optic modulators at the front end of the system, since there always is a certain degree of inaccuracy in determining the

exact amplitude and phase response of each of the modulators, expressed for example as inaccuracy in knowing the V_π voltage of a modulator. Also, one can expect that various linear and nonlinear effects in the fibers and components of the fiber amplifier chain might also affect both the amplitudes and the phases of the stacking-burst pulses. It is certain that quantifying all these effects beforehand would be a very challenging, and perhaps even a hopeless task.

Therefore, it was one of the critical research tasks carried out for this thesis to develop a computer-based control system, which would optimize the stacking-burst amplitude and phase profiles in real time, based on the measured fidelity of the stacked pulse at the system output. This work is described in detail in the chapter 5.

1.6 Pathways to Pre-Pulse Contrast

Throughout this work we had used stacked pulses fidelity measurement based on peak power detection. This, however, puts certain constrains on the maximum achievable fidelity of the stacked pulses. Indeed, one of the important desired characteristics of the stacked pulses is associated with a high degree of pre-pulse contrast of up approximately 40 – 60 dB, which is required by laser-plasma acceleration applications, as well as numerous other laser-matter interaction-based applications. Since in practice peak detection cannot be achieved with better than approximately 1% accuracy (due to the laser amplitude noise), this stacked-pulse fidelity metrology does not allow achieving pre--pulse of better than approximately 20 dB. At this point we have identified techniques with which this limitation can be overcome (for example, developing a new fidelity measurement technique which would detect both the pre-pulse content and the stacked pulse peak). However, development of these techniques is outside of the topics of

this thesis and will be carried out in the future. Nevertheless, it is important to point out that this next stage in improving fidelity of the stacked pulses will necessarily be founded on the work reported in this thesis.

Chapter 2 Algorithmic and Hardware Basics of the Control System

2.1 Background

As previously explained coherent pulse stacking is a time-domain combining technique where the GTI cavity phases should be stabilized in real-time to achieve stacking. As shown in equations (1.2), (1.5), and (1.6), for a given stacker design, round-trip phases of the GTI cavities, as well as input pulse amplitudes and phases are known; However, cavity phases change in time and need to be precisely kept at the required values. This is done by an active stabilization system.

Stabilizing the GTI stacker system is a key element in CPSA to achieve robust stacking and it directly affects the stacking parameters such as stacking efficiency. The stacker design defines amplitudes, and phases of the input pulse profile ($\tilde{A}^{in}[k]$ in equation (1.6)) where they are imprinted onto the burst by the electro-optic modulators (EOMs) and are kept unchanged during stacking. The design also defines the required mirror reflectivities for the cavities that cannot be changed once they are fabricated. However, phase variations in the GTI cavities or the oscillator need to be actively controlled by an stabilization system to stabilize the phases as required for stacking.

Before discussing the details of how we developed the stabilization algorithm, a general discussion in broad sense about the concept and definition of stabilization in control theory followed by a survey of different stabilization algorithms is presented. This provides the reader

with broad insight into the subject before being deeply involved into the formulations. Among the many stabilization algorithms that are discussed here in the survey section, we chose stochastic parallel gradient descent (SPGD) due to its model-free and stochastic-based model, its relatively fast convergence, simplicity in implementation, and etc.

2.2 Concept and Definition of Stabilization in Control Theory

Stabilization system in a general and broad sense is a particular control system that is commonly used in a variety of engineering problems and applications. Control systems exist in almost every aspect and they consist of different parts that can give commands, regulate, improve, and manage the behavior of a single or a group of devices. Automobile steering control system, temperature-controlled air conditioning systems, GPS-based path control systems in vehicles or aircrafts are only a few examples of many types of the existing control systems. A control system can be generally discussed in open-loop and closed loop forms. An open-loop configuration is not able to compensate for any internal or external noise, thus will not be discussed here. On the other hand, a closed loop configuration is well-known for its ability to reconstruct or compensate for any possible disturbances in the system. The configuration (see figure 2.1) starts with an input transducer which converts the input to the measurable electric signal that is further used by the controller. For instance, if the input signal is position it can be converted to voltage through a potentiometer or in the case of digital control system, if the input signal is an analog electric signal, it can be converted to a digital signal through Analog to Digital Converters (ADC). Next block in the configuration is just a subtractor which can be a mixer producing an error signal which shows how deviated the output signal is from the desired input signal. This error signal is then used by the controller to decide in which direction and how to drive the system (plant, or process) [48,49].

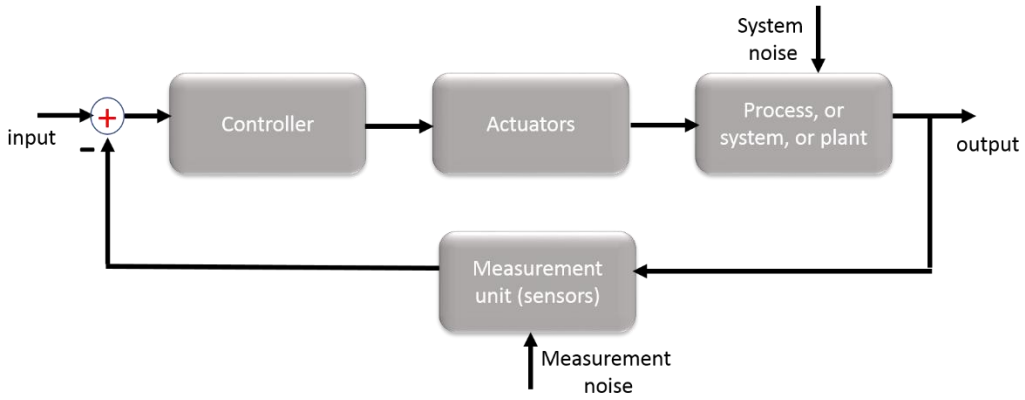

Figure 2.1: Typical closed loop configuration of a control system [49]

The plant, process, or system block in many cases are unstable systems where the controller (stabilization system) tries to stabilize it. In control theory, the stable system is generally defined as a system whose response to a bounded input is bounded. Or in other words, the system does not exhibit oscillatory or unbounded behavior in response to a bounded input [48,49]. There exist many approaches in control theory to check this criterion. For example, Laplace transformation is one specific approach where this criterion is checked by evaluating the poles of the system transfer function. If all the poles of a transfer function lie on the closed left hand plane (LHP) then the system is called stable. [50]. Assuming that a system is potentially stabilizable, the question is that what are the conditions that need to be satisfied to stabilize an unstable system. As discussed previously a stabilization system is essentially a closed-loop control system. The inputs of a typical stabilization system are the control parameters or the parameter space that define the output signal. For example, for the case of coherent combining systems, phases of the combining elements are the key parameters that define the output signal. Therefore, input signal in the closed-loop configuration of the control system is a vector of combining element phases. The feedback path might need a mechanism to extract phase information from the output signal. Usually the output signal in such combining system is a function of intensity. The controller unit in figure 1 is the

stabilization algorithm that determines how to derive the actuators and consequently the plant which will be the system. This discussed overview of typical stabilization systems implies that an unstable system and consequently the output signal is stabilized once the error signal goes below certain threshold and ideally approaches zero. In other words, the vector of phases gets locked with high precision to the required values. Upon satisfaction of this criteria, the system and the output signal are stabilized but not necessarily optimized in terms of the desired performance.

The following section discusses in detail a general survey of existing stabilization algorithms that can be used for stabilizing coherent combining systems and lasers.

2.2.1 Survey of Stabilization Algorithms

1) Stochastic Parallel Gradient Descent (SPGD) Algorithm:

Gradient Descent Algorithm

A popular method for finding the global minimum of a metric function or minimizing an error functional for a known metric is the gradient descent (steepest descent) [30,31,32,33,34] (if the goal is to find the global maximum of the function the algorithm is called gradient ascent (steepest ascent). These algorithms calculate gradients based on detailed knowledge of the metric model and they involve calculating exact values of the derivative of the goal function. Gradient method is based on the observation that if the goal function $J(\vec{u})$ is defined and differentiable in a neighborhood of a point then $J(\vec{u})$ increases fastest if one goes from $\vec{u}^{init}$ in the direction of the gradient as follows [30]:

$$\vec{u}^{i} = \vec{u}^{i} + \mu \nabla J(\vec{u}^{i}) \qquad (2.1)$$

However, for those scenarios where the goal function is not analytically known, or where calculating exact values of the gradients in the landscape is analytically or numerically difficult, an alternative algorithm to the gradient descent is the Hill-Climbing Stochastic Gradient Descent method it is independent of the exact gradient calculation.

Hill-Climbing Stochastic Gradient Descent Algorithm

For many years, a sufficiently simple and efficient optimization technique was the mountain-climbing technique where the optimization unit tries to detect the best path in the landscape of the control parameters for maximizing/minimizing a certain goal function in the system (see figure 2.2). This is achieved by disturbing the control parameters and correspondingly evaluating the variation of the goal function. It has been shown that following the gradient path in the landscape is the optimal path [29]. Currently, this method is being used by the stochastic gradient descent (SGD) optimization algorithm.

Stochastic gradient descent (SGD), from machine learning point of view was originally introduced in [36] but from control and applications point of view, it is an improved alternative algorithm to the standard gradient descent (GD) method simply because GD requires computation of a full gradient on each iteration. Stochastic Gradient Descent Algorithm is a model-free (blind) algorithm for optimization purposes and it is a local optimization that seeks to "climb the hill" toward the local maximum (or minimum), and for this reason it is sometimes also referred to as a "hill climbing algorithm". In general, Stochastic Gradient Descent (SGD) algorithms are commonly used mainly because of their simplicity and ease of implementation. SGD has been widely used in control areas even for complicated systems. While the key advantage of the SGD algorithm is its model-free characteristic it is also popular due to its stability if it converges, its simplicity for implementation, and its potential for scalability.

The algorithm is based on the idea where the small perturbation δu_m (the perturbation voltage which follows the Poisson random distribution or Gaussian random distribution on the m^{th} step, e.g. the probability density distribution ($P(\delta u_m) = \pm\tau) = 0.5$) is applied to the control parameter u_m in the system. For instance, in our CPSA system, $u_1, u_2, \dots, u_N$ will be the cavity phases as the control parameters and the perturbations δu_j are applied to them. The resulting change in the system performance metric would be expressed in a Taylor expansion as in equation 2.2 if perturbations were sequentially applied: [26]

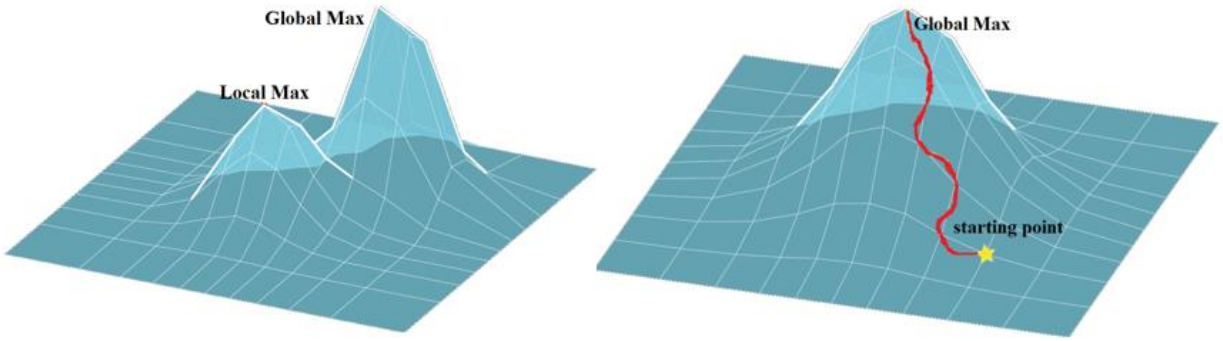

Figure 2.2: Hill-Climbing algorithm

$$\delta J = \frac{\delta \mathrm{J}}{\delta u_m}\delta u_m + \frac{1}{2}\frac{\delta^2 J}{\delta u_m^2}(\delta u_m)^2 + \cdots \tag{2.2}$$

The metric J that we used in our system is a second harmonic generation (SHG) signal proportional to the intensity to the power of four at the output of the stackers. If we multiply both sides of the equation above by δu_m we will have:

$$\delta J \delta u_m = \frac{\delta J}{\delta u_m}(\delta u_m)^2 + \psi_m \tag{2.3}$$

The term $\delta J \delta u_m$ in the equation above is essentially a sum of two terms. The actual gradient component $\frac{\delta J}{\delta u_m}(\delta u_m)^2$ and the noise term ψ_m.

Now, there is an interesting feature in stochastic gradient descent algorithm compared to the conventional gradient descent algorithm and that is the replacement of the true gradient component $J'_m = \frac{\delta J}{\delta u_m}$ with the product $\delta J \delta u_m$. This is key benefit of the Stochastic Gradient Descent (SGD) method over the conventional gradient descent (GD), one which requires exact calculation of the gradient at each point. We will present the proof for this feature in a more general fashion in section 2.2.3 where Stochastic Parallel Gradient Descent (SPGD algorithm.

Stochastic Parallel Gradient Descent (SPGD)Algorithm

In order to speed-up the Stochastic Gradient Descent (SGD) algorithm, it is much more efficient to parallelly perturb the control parameters instead of dithering them sequentially. This opens the path to the stochastic parallel gradient descent (SPGD) algorithm which was first applied for adaptive optics in 1997 by M.A.Vorontsov [26]. The idea here is to apply perturbations δu_j (the perturbation voltage vector) simultaneously (Parallel) to the control parameters in the system.

$$\delta J = J(u_1 + \delta u_1, u_2 + \delta u_2, \dots, u_N + \delta u_N) - J(u_1, u_2, \dots, u_N) \tag{2.4}$$

$$\delta J = \Sigma \frac{\delta \mathrm{J}}{\delta u_j} \delta u_j + \frac{1}{2} \Sigma \frac{\delta^2 J}{\delta u_i \delta u_j} \left(\delta u_i \delta u_j\right) + \cdots \tag{2.5}$$

Now, in this part, it will be shown why in SGD the exact gradient can be replaced by the product $\delta J \delta u_m$. Let us evaluate both sides of the equation above in terms of average [26].

$$< \delta J \delta u_m >= \frac{\delta J}{\delta u_m} < (\delta u_m) >^2 + < \psi_m > \tag{2.6}$$

$$< \psi_m >= \sum_{j \neq m}^{N} \frac{\delta \mathrm{J}}{\delta u_j} < \delta u_j \delta u_m > + \frac{1}{2} \sum_{i,j}^{N} \frac{\delta^2 J}{\delta u_i \delta u_j} \left(< \delta u_i \delta u_j \delta u_m >\right) + \tag{2.7}$$

Usually the terms δu_j are generated as statistically independent variables with zero expected value and same variances.

$$< \delta u_j \delta u_m >= \sigma^2 \delta_{i,j} \quad \&\& \quad < \delta u_j >= 0$$

$$< \delta u_i \delta u_j \delta u_p >= 0 \; for \; all \; i,j,p \tag{2.8}$$

Consequently $< \psi_m >= O(\sigma^4)$. Therefore, we can conclude that statistical average of the term $\delta J \delta u_m$ (stochastic gradient) is well-approximated by the scaled gradient value (J'_m) to the accuracy of $O(\sigma^4)$. This is the most important conclusion manifesting the reason why the stochastic gradient descent can be a suitable candidate for replacement of the conventional gradient descent algorithm. (e.g. replacement of J'_m by $\delta J \delta u_m$).

As is known, control parameters { u_m} (m=1,…,N) in the conventional gradient descent algorithm are updated through an iterative process as $u_m^{i+1} = u_m^i - \mu(\frac{\delta J}{\delta u_m})$, where i is the iteration number and μ is the gain coefficient (positive for minimizing ΔJ). This iterative process can be similarly applied for the SGD algorithm by replacing the actual gradient term $\frac{\delta J}{\delta u_m}$ by the so-called stochastic gradient term $\delta J \delta u_m$ discussed above. The resulting relation is as follows:

$$u_m^{i+1} = u_m^i - \mu(\delta J^i \delta u_m^i) \tag{2.9}$$

It is necessary to evaluate the variation of the metric function as the dithering δu_mon the control parameters is applied. The variation of the metric function between two consecutive

iterations can be written as $\Delta J = J\left(u^{i+1}\right) - J(u^i)$. Plugging equation (2.9) into equation (2.4) and (2.5) we would have the following:

$$\Delta J \cong \sum_{m=1}^{N} \left(\frac{\delta J}{\delta u_m}\right)(-\mu \delta J \delta u_m)$$

$$= -\mu \sum_{m=1}^{N} \left(\frac{\delta J}{\delta u_m}\right)\left(\frac{\delta J}{\delta u_m}(\delta u_m)^2 + \psi_m\right)$$

$$\cong -\mu \sum_{m=1}^{N} \left(\frac{\delta J}{\delta u_m}\delta u_m\right)^2 - \mu \sum_{m,n\neq n}^{N} \frac{\delta^2 J}{\delta u_m \delta u_n}(\delta u_m \delta u_n) \quad (2.10)$$

By using the assumptions in (2.8) implying that the dithering values are statistically independent from each other and their variances are the same and equal to σ, (2.10) can be evaluated in terms of the statistical average as follows:

$$< \Delta J > = -\mu\sigma^2 \sum_{m=1}^{N} \left(\frac{\delta J}{\delta u_m}\right)^2 + O(\mu\sigma^4) \quad (2.11)$$

Equation (2.11) shows that the metric function tends to decrease on average under the previously-mentioned conditions if the first term dominates the sum on absolute.

In this part a thorough reasoning from physical point of view is presented to manifest the advantage of the SPGD over sequential-based SGD in terms of the convergence speed. It has been proved in the literature that the maximum speed of the sequential-based SGD algorithm is a factor of N slower than the conventional gradient descent algorithm. Now we will show that SPGD can reduce the upper limit of this maximum speed to $\sqrt{N}$ meaning that the maximum speed of the SPGD algorithm is effectively $\sqrt{N}$ slower than the conventional gradient descent algorithm. In other words, SPGD performs $\sqrt{N}$ times faster than the sequential-based SGD algorithm.

SPGD is implemented by simultaneously generating N stochastically independent dithering values and applying them in N parallel paths. The variation of the single metric function instead is evaluated only through a single path. This means that maximum effective information that can be obtained on average about the response of the system to the N paths of control parameters is through $\sqrt{N}$ paths. However, this is the best case that can be achieved only if all the N dithers are completely independent from each other allowing for maximum information extraction. The worst case also happens when the information is extracted only through a single path. As a result, by parallelly dithering the control parameter through SPGD once can achieve a factor of $\sqrt{N}$ faster speed compared to sequential-based SGD algorithm. [30]

Convergence of SPGD

Convergence of the SGD or SPGD algorithms has been analyzed from different points of view. One of the well-known ways is through the theory of convex/concave minimization/maximization. It can be shown that by making the gain parameter sufficiently small in the vicinity of the global peak the algorithm is almost guaranteed to converge to the global maximum. Otherwise, it is mostly probable for the algorithm to converge to a local maximum. This analysis is essentially one of the results of the so-called Robbins-Siegmund theorem [35]. As we will be explaining more in detail in further chapters, the objective function in our optical system is not a concave/convex function since it has many local peaks around the main global peak. However, executing a local search prior to the actual stochastic gradient descent algorithm will compensate for that we can show that the objective function can converge to the desired global peak.

Convergence of the gradient-descent-based algorithms can be also viewed and analyzed from other directions. In fact, the steeper the gradient path in the landscape is, the faster the algorithm reaches the ultimate global peak. This essentially implies that the larger absolute values of the gradients $J'_m = \frac{\delta J}{\delta u_m}$ at each point in the landscape are, the steeper the gradient curve is and consequently the algorithm approaches the peak faster. This idea can be similarly applied to the SPGD algorithm as well where instead the average variation of the goal function $< \delta J >$ should be maximized to increase the convergence speed. [26]

stability of SPGD

Stability analysis for SPGD-based Control systems can be done in different ways. For instance, for those systems where the goal/metric function is mathematically provided, Lyapunov functions are used to prove that a system is locally stable [28]. In this technique, the defined function needs to be locally evaluated for 2 different criteria. One is that the function is locally positive definite and the second is that it is simultaneously possess a semidefinite negative time derivative at that spot. Upon satisfaction of these two criteria the system is proved to be stable at the specified spot.

Another approach which has recently been developed is based on the assumption that the goal function behaves parabolically around the point to be stabilized. [22]. In this analysis optimal steady state error of the cavity phase and average of the metric function has been analytically calculated as follows:

$$Err(\delta_i) \approx 3.42 M R_0^2$$

$$< J(\vec{\delta}) > \approx J(\vec{\delta}^{opt}) - 1.71|H|M^2 R_0^2 \qquad (2.11)$$

Where $Err(\delta_i)$ is the steady state error of cavity phases, M is the number of cavities, R_0 is the standard deviation of the cavity phase noise profile, and $|H|$is the magnitude of the second derivative for the metric. As $|H|$ does not show up in (2.11) for calculating the steady state error it implies that $Err(\delta_i)$ does not depend on what objective you have chosen or in other words, only the number of cavities and the noise magnitude matters for minimizing the steady state standard deviation.

2) LOCSET (self-referenced & self-synchronous)

In this section a summary of the theory of an active coherent technique called LOCSET (locking of optical coherence by single-detector electronic-frequency tagging) [51,52,53] is presented. This technique is usually implemented in two different ways namely self-reference and self-synchronous. The difference is that in self-synchronous version all the array elements in the system are modulated in phase whereas in self-referenced version one of the elements is remains unmodulated during the locking process. In the following section a summary of how this technique is modeled and implemented is presented.

Suppose that the electric fields associated with each individual array element in an array of optical fibers are modeled as polarized plane waves as in equation (2.12):

$$E_m = A_m \cos(\omega_L . t + \phi_m + B_m \sin(\omega_m . t)) \tag{2.12}$$

Where A_m $(1 \leq m \leq N)$ represent the amplitudes of the electric fields for each of the modulated array elements. ω_L represents the central laser frequency, ϕ_m represents the optical phases associated with each array element which equivalently shows the relative phase among them. β_m represents the phase modulation associated with the m^{th} element in the array, ω_m represents the radio frequency (RF) angular frequency associated with the m^{th} array element. Notice that for

the case of self-referenced LOCSET one of the array elements is not modulated. The total electric field sensed at the photodetector can be modeled as the superposition of the individual modulated and unmodulated electric fields as:

$$E_{tot} = \sum_{m=1}^{N+1} E_m(t) \quad \text{for the self-synchronous LOCSET} \tag{2.13}$$

$$E_{tot} = E_{um}(t) + \sum_{m=1}^{N} E_m(t) \quad \text{for the self-referenced LOCSET} \tag{2.14}$$

In equations (2.13) and (2.14), $E_{um}(t)$ represents the unmodulated electric field.

As a result, the photodetector current or the sensed intensity by the photodetector is proportional the above summation squared as follows:

$$I_{tot} \propto (E_{um}(t) + \sum_{m=1}^{N} E_m(t))^2 = (E_{um}^2(t) + \sum_{p=1}^{N} E_p(t) \sum_{q=1}^{N} E_q(t) + 2E_{um}(t) \sum_{m=1}^{N} E_m(t)) \tag{2.15}$$

The intensity signal is then used to extract the error signal through RF demodulation process. The whole intensity function is multiplied by $\sin(\omega_m t)$ and integrated over certain time period to extract the error signal associated with the m^{th} array element (see equation 2.16))

$$Err(m) = \frac{1}{\tau} \int_0^{\tau} I_{tot}(t). \sin(\omega_m t) dt \tag{2.16}$$

The aforementioned error signal can be approximated to high degree of accuracy under specific condition. This condition states that the integration time should be sufficiently longer than $2/\min(\omega_i - \omega_j)$ for all the $i's$ and $j's$ where $1 \leq i, j \leq N$ and $i \neq j$. Under this condition the error signal can be approximated as follows:

$$Err(m) \propto \sqrt{P_m} J_1(\beta_m) [\sum_{j=1}^{N} J_0(\beta_j). \sqrt{P_j} \sin(\phi_j - \phi_m)] \tag{2.17}$$

Where J_0 and J_1 are the 0^{th} and 1st order Bessel functions respectively, and P_i represent the optical power sensed by the photodetector associated with the ith array element.

3) Hänsch-Couillaud technique

This technique has been first used by T.W. HANSCH and B. COUILLAUD to stabilize the frequency of the laser by polarization spectroscopy of a passive reference cavity but has been widely used for variety of spatial combining of FPCA laser systems as well. [54]. Prior to this technique there were many locking schemes that were used to electronically locked the laser frequency to a passive reference cavity. However, this technique utilizes a passive cavity as well as an internal linear polarizer to monitor the changes in the polarization of the reflected beam [55].

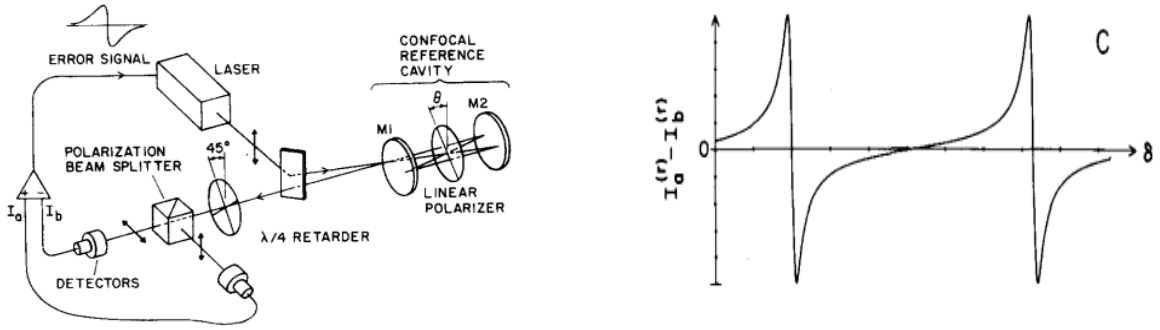

Figure 2.3: Scheme of laser frequency stabilization using Hänsch-Couillaud technique [55]

In order to briefly explain this technique, we consider a linearly polarized incoming light from the laser incident on the passive reference cavity with the intracavity polarizer (see figure 2.3). This linearly polarized light can be decomposed into two orthogonal linearly polarized electric fields, parallel and perpendicular to the transmission axis of the polarizer inside the cavity. As calculated in [55], the reflected electric fields associated with the two orthogonal components can be calculated as follows:

$$E_{||}^{r} = E_{||}^{i}\left(\sqrt{R_1} - \frac{T_1 R}{\sqrt{R_1}}\frac{cos\delta - R + isin\delta}{(1-R)^2 + 4Rsin^2\frac{1}{2}\delta}\right) \;\&\; E_{\perp}^{r} = E_{\perp}^{i}\sqrt{R_1} \qquad (2.18)$$

R_1 and T_1 are reflectivity and transmittivity of the M1 mirror shown in the scheme, R is a ration factor taking into account the losses in the intracavity polarizer. It also determines the amplitude

ration between successive roundtrips, and the cavity finesse as well. By looking into the two reflected electric field, one can see a phase difference between the two components due the imaginary part of $E_{||}^{r}$. This happens at off-resonances ($\delta \neq 2m\pi$) where produces an elliptically polarized beam. This elliptically polarized light then enters a combination of a $\lambda/4$ retarder and a beam polarization splitter to measure its ellipticity. The difference between the output intensities $I_a - I_b$ as shown in the scheme is then used to generate an error signal and consequently servo-lock the laser frequency.

4) A. D White Stabilization Technique:

This technique was reported by A. D White in 1965 for stabilizing lasers based on high quality factor optical cavities [57]. Prior to this Pound in 1946 introduced the frequency stabilization scheme in microwave regime where high quality factor cavities were used as discriminators [56]. Here in optical regime, transmission or reflection characteristic of a high quality factor optical reference cavity is used to measure the deviation of the laser frequency from the reference cavity frequency and thus control it. In order to this, central frequency of a high Q optical cavity is modulated at a low frequency f_m, and consequently the reflected or transmitted beam is modulated as well. The intensity modulated component in the transmitted beam is then detected by a phase detector (PD) and used an error signal to lock the laser frequency to the center frequency of the cavity [56]. There exist some drawbacks for this technique. First, the electronics required for modulation and phase detection need to be extremely precise and they are quite slow in functioning. Second, the signal away from the resonance becomes small very fast and thus makes it difficult to compensate for very large laser frequency deviations.

5) Pound Drever Hall (PDH) method for phase and frequency stabilization:

This technique is a powerful method for stabilization of laser frequency using the derivative of the reflected beam from an optical cavity [58]. Prior to this technique, many locking schemes such as [57] were introduced which were based on measuring the intensity of the transmitted beam through an optical cavity, and then feeding it back to the laser to compensate for the changes in the laser frequency. However, these techniques could not allow the user to distinguish between laser intensity changes and laser frequency changes since both of them could produce the same changes in the intensity of the reflected light [59]. In this case, PDH method uses the reflected beam from an optical cavity and try to lock it to zero which separates the intensity noise from the frequency noise. In this way the previous drawback is resolved. However, due to the symmetry of the reflected intensity around the resonance, characteristic of the derivative of the reflected light is needed since its spectrum is asymmetric with respect to the resonance. Above the resonance the intensity increases in phase with frequency, and below resonance it decreases 180 degree out of phase from the frequency. This reflected signal is then feedbacked to the laser for locking its frequency to the optical cavity. The detail of this scheme is shown in figure 2.4.

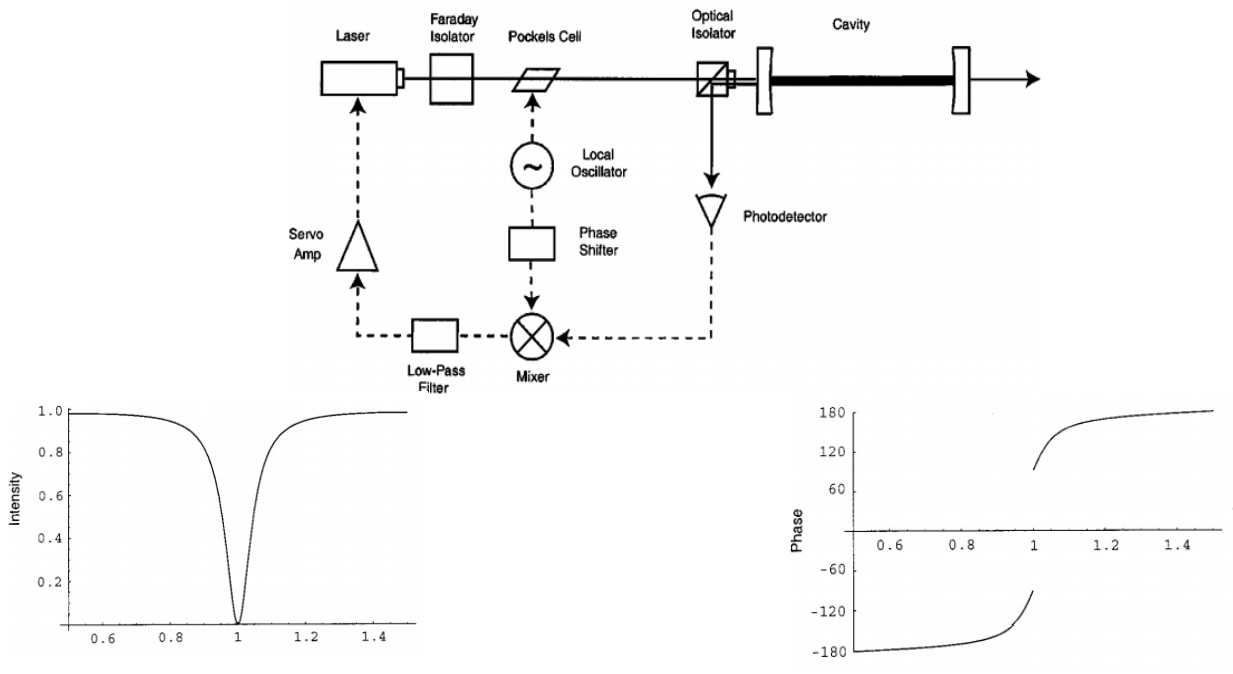

Figure 2.4: (top) block diagram of the PDH stabilization scheme, (bottom left) intensity spectrum of the reflection coefficient for a Fabry-Perot cavity (bottom right) phase spectrum of the reflection coefficient for a Fabry-Perot cavity. [58,59]

SPGD Implementation

As discussed in the survey of stabilization algorithms, monitor signals have been used in some techniques which will be troublesome if we extend the number if GTI cavities. Therefore, we can use the two-photon absorption (TPA) or equivalently second harmonic generation (SHG) signal detection schemes. In the cascaded GTI configuration, instead of using a monitor signal, a single peak power detector is used to feedback the frequency-modulated channels. Each channel is modulated at a modulation frequency of few kHz utilizing analog circuits and then demodulated in the same way as done in single cavity stabilization [37].

However, using the peak detection technique can be utilized in more efficient and simpler control algorithms that can stabilize the stackers much faster.

To resolve this issue, it is needed to first look for a stochastic-based algorithm since instantaneous cavity phase values or their positions in the N-dimensional phase landscape is not

known, and second a model-free algorithm which does not dependent on the analytical form of the metric as a function of our control parameters (e.g. Cavity Phases). That is why we chose Stochastic Parallel Gradient Descent (SPGD) algorithm for stabilization and optimization purposes in this research. This algorithm is a hill-climbing technique which will be further explained in the subsequent section.

The demonstrated control system based on the SPGD algorithm, is shown in Fig 2.5. It applies small random perturbations to all control parameters (voltages of PZTs) simultaneously, and then evaluates the gradient variation of system performance metric (J).

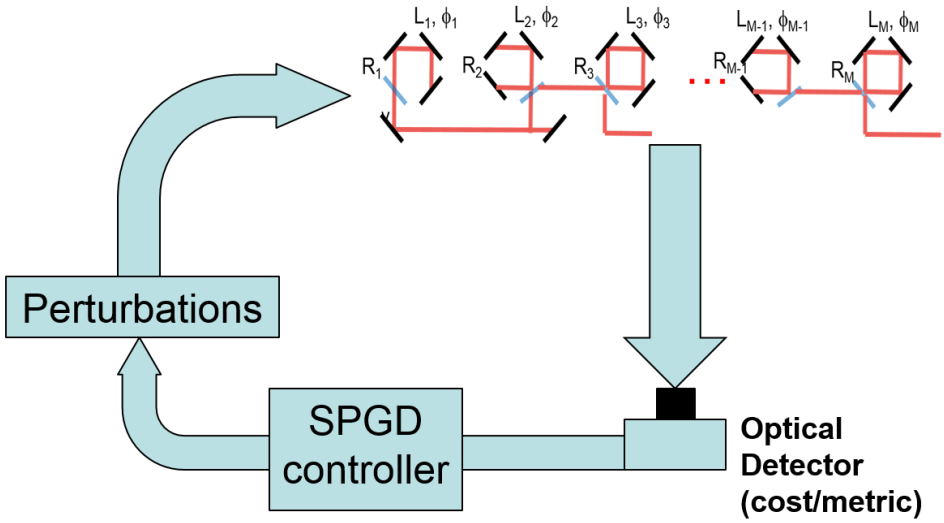

Figure 2.5: SPGD model in GTI based CPSA system

Although measuring the exact instantaneous cavity phases is not required for stacking there are some ways to measure them. As an example, our collaborators in Lawrence Berkeley National Laboratory (LBNL) uses a pulse-pattern-based cavity phase detection algorithm to measure the instant values of the GTI cavity phases. In this technique a burst of N pulses separate from the actual stacking burst is transmitted through the GTI cavities. This specific pulse burst probes the

instantaneous round-trip phase of the GTI cavities based on the fact that there are different measurable intensity functions corresponding to each of the individual pulses while the cavity phases changes over the 2π interval. As a result, it is supposed that the instantaneous phases can be probed and measured by combining those intensity functions [25]. However, beside the technical and implementation costs behind the above technique, still it suffers from the fact that it does not inherently determine what cavity phases are required to realize stacking.

2.3 Stabilization System Implementations

2.3.1 Analog Electronics

The initial techniques explained in the beginning of the chapter for locking single cavity using Monitor signal and Transmission, and locking multiple cavities using peak detection and frequency tagging of each channel have been implemented using Analog Circuits (See Fig 2.6)

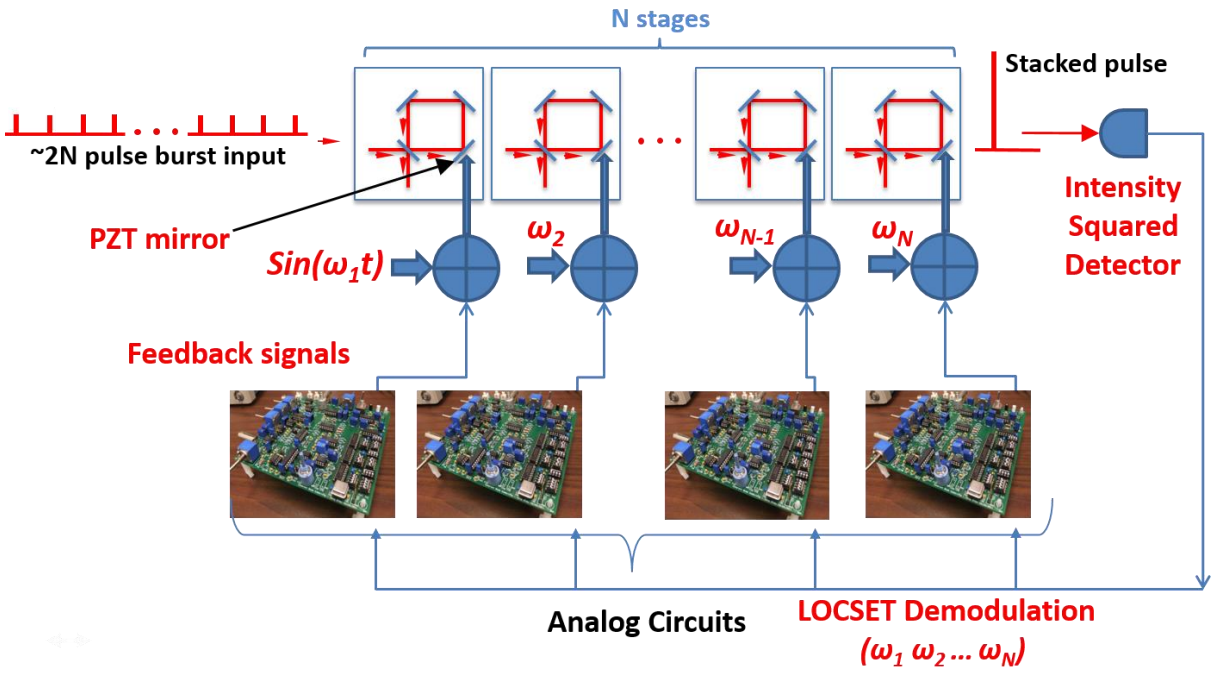

Figure 2.6: Analog-Implementation for stabilizing N-cascaded GTI cavities

Such implementations face many challenges. First is that the number of analog circuits linearly increase with the number of GTI cavities thus making it inflexible. Implementations of such algorithms either in Analog or Digital platforms requires extensive effort for designing filters, frequency up/down counters, mixer, phase shifters, and etc. The other challenge is that manual adjustment of the feedback parameters such as gain and perturbation to lock the cavities take extensive time for multiple GTI cavities case (e.g. 2 Cavities take 0.5 hour and 4 Cavities take 4 hours), thus making it quite inefficient. Lack of remote accessibility and automation are also some other disadvantages of this implementation.

2.3.2 Software-Based Implementation

In order to bypass the challenges in Analog-Based Implementation of the feedback control system we can implement the digital control system which benefits from remote accessibility, automation, improved performance at low frequencies where low frequency electronic noise may be a problem. As the first try, we implemented a LABVIEW-Based control system using stochastic parallel gradient descent (SPGD) algorithm which is in-detail explained in chapter 2. (See Fig 2.7)

LABVIEW can be considered as a graphical-based language and tool for designing complex control systems which provides the user with many pre-defined modules for application development purposes via Graphical User Interface (GUI). The existing modules and libraries inside the design environment are fully compatible with the external electronic instrument and hence are widely used in many automation tasks. The digital signal processing and arithmetic operations carried out in the LABVIEW environment makes it almost immune to the noise compared to the analog platforms and hence is an advantage.

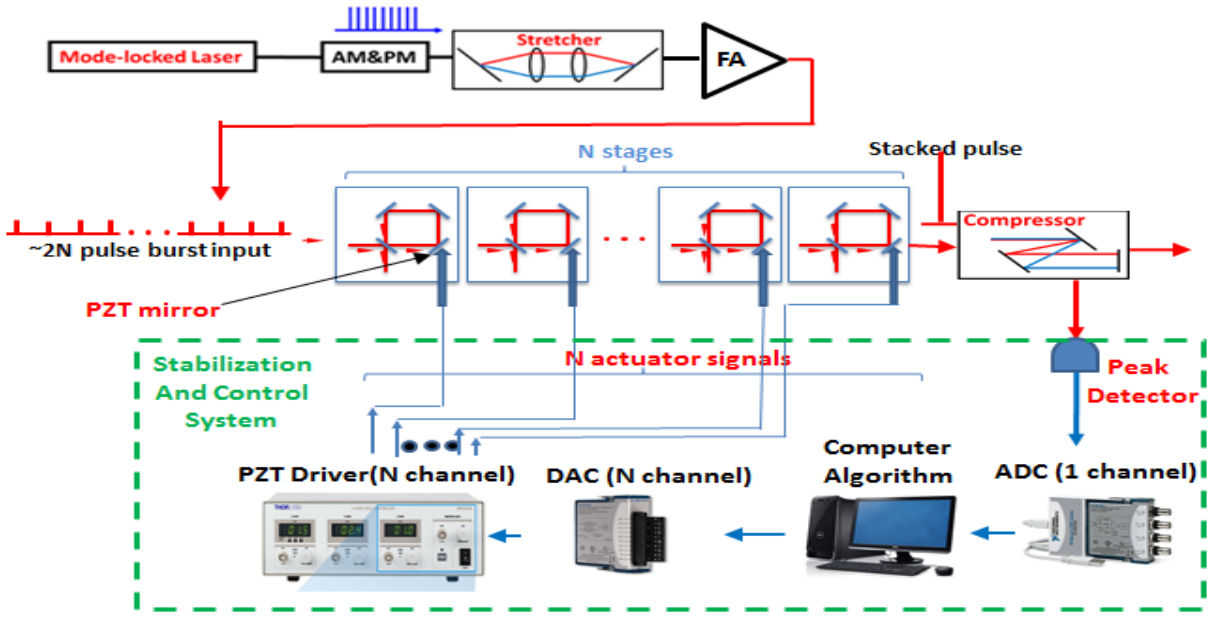

Figure 2.7: Software-Based Implementation for stabilization of N GTI stacker system

However, control loops implemented in LABVIEW suffer from poor execution speed. In order to overcome this limitation we implemented the algorithm in python.

In this section we report the demonstration of a turn-key cavity-stabilization technique for an N-cavity sequence of GTI pulse stackers, which takes seconds to establish itself, and then operates robustly over long and continuous time period. It is very simple in that it does not require

any separate monitor signals, or frequency tagging of each individual cavity. It is based on a single peak-detector, which samples the stacked-pulse signal at the system output and achieves optimized and stable stacking-system performance by maximizing the output pulse peak power. Its implementation is completely digital, relying on analog-to-digital signal conversion, and on software-based system control algorithms. In this control system the SPGD algorithm achieves a very time-efficient and, therefore, rapid system control, thus ensuring robust long-term stability of an N-GTI pulse stacking system against external perturbations. Since the hardware complexity of the demonstrated control system does not depend on the number N of the stacking cavities, it constitutes a very efficient control platform for scaling of the CPSA technique.

Our system control pathway consists of a pulse peak-power detector, a single-channel ADC converter, computer-based system control software, and an N-channel DAC converter, which controls an N-channel PZT driver.

There are number of merits that are important in complex control systems such as limitless flexibility, sufficiently high-speed execution loop, and so on. National Instrument Fixed-Hardware A/D and D/A convertors along with the communication/data path through USB with the PC where the control algorithm is implemented in either LABVIEW or Python languages is limited in providing high speed execution loop. The PC CPU involved in the data communication path and different operations must compete for the same resources. The other limitation to be addressed in such systems is that the software application (e.g. the control algorithm) cannot be hardware-wised implemented where the operations and control algorithms are run much faster. This is the due to the fixed hardware resources in the National Instrument Modules. (However, recently National Instruments LABVIEW-FPGA modules has provided embedded FPGAs that can be programmed using LABVIEW, but it still lacks in some specific cases [27]).

In order to overcome the limitations explained, we decided to benefit from the Field-Programmable-Gate-Arrays (FPGA) technology. FPGAs are well-known for their potentially high-speed operations. This benefit is mainly because they allow for parallel logical and arithmetic operations without the need to compete for access to the processor resources. There is also no operating system in FPGA systems as opposed to the PC-based systems or processors. These features make it possible for the user to be able to parallelly run as many control loops as needed at potentially and sufficiently high execution and update rates. High speed gets more and more important when we go to real-time control of pulse shaping with bandwidth of at least 4 to 5 GHz for saturation compensation. Overcoming the limitations of the conventional Arbitrary Waveform Generators (AWGs) by replacing them with FPGA/fast Digital-to-Analog converters (DACs) is another benefit that can be addressed here. In the next section, details of FPGA control systems will be explained.

2.3.3 FPGA Based Control System

Timing and synchronization among electronic and control elements plays one of the most important roles in outputting an exact timed and jitter-free signal in any control systems. This becomes more critical in time-domain-based techniques such as combining approaches where the read-out, data-processing, and outputting feedback all need to be synchronized. Here in this research we took advantage of the fast processing and high-precision timing capabilities of the FPGA technology through development of software and firmware to realize stacking stabilization and input burst optimization in CPSA system. Fast Analog-to-Digital (ADC) for reading purposes, fast DAC for outputting high-precision feedback signals, FPGA evaluation-board for processing purposed, central PC, for executing the control algorithm, all make a distributed control system which is not only stable enough but is potent to be scaled for larger number of resonators too.

Let us first take a look into the historical path for control implementations and see how FPGAs came in to lead the path. In general control implementations can be realized in two different ways, software-based and hardware based. Software-based implementations such as DSPs (Digital Signal Processors) and microcontrollers require a memory as a platform for maintaining and saving the target control program and a processor to decode and executes the control program. On the other hand, hardware-based implementations utilize electronic components to perform the control commands. In this category many generations have been emerged. In the early 19^{th} century relays were developed which were used as electric switches to turn on/off bigger parts of a system. Then digital gates appeared to be an efficient alternative for on/off switching and other commands in a control system. After these, Integrated circuits showed up starting from the early mini-scale versions (MIS), then large-scale (LSI), Ultra-large scale (USI) and finally very-large scale ICs (VLSI). And finally, application-specific integrated circuits were developed using those ICs for specific tasks in a complex system. However, the process for making ASICs are quite time consuming and hence are not popular for control applications.

FPGA is a technology that allows the user to configure arbitrary integrated circuits for certain purposes and any logic-based tasks can be implemented using these FPGAs. They have shown great advantages compared to both software-based control systems and previous hardware-based generations of controllers. Much faster execution and processing time, scalability, flexibility for being configured for different functions, efficient power consumption and etc are among many advantages of FPGAs.

Specifically, FPGAs are we suited for implementing digital control systems due to their high processing and execution speed, compactness, and power efficiency. Real-time control

systems where the inputs and the target/goal functions need to be updated in real-time are the best applications where FPGAs can be used in the form of a single chip or an evaluation board for communication between other boards. Control algorithms are programmed in a reconfigurable and small-size platform which can be easily edited.

Hardware Structure of the FPGA control system

As shown in figure 2.8, the ML605 FPGA Evaluation Board is an FPGA based digital signal processing board which is used for designing versatile electronic and control platforms using the Virtex-6 FPGA. The Ml605 evaluation board connects the FPGA and the CPU via 1Gbit Ethernet and provides the interface between the FPGA and the physical layer (PHY) through GMII (Gigabit Media Independent Interface). Here, the FPGA evaluation board is externally interfaced with two boards. First it is interface with 2-Channel 1GSPS ADC and 2-Channel 1GSPS DAC via FMC HPC connector. And second, it is interfaced with XM105 daughter card via FMC LPC connector and then gets connected to the 8-channel slow DAC.

The ML605 FPGA board processes digital signals captured by high-speed ADC and then sends feedback signals to the modulator and the cavity actuator. An outerloop control module tries to optimize the input burst profile in terms of amplitude and phase and a cavity control module ensures that each optical cavity is phase stabilized. The FPGA outputs the feedback control signal to optical cavities at kHz frequency, to support kHz repetition rates.

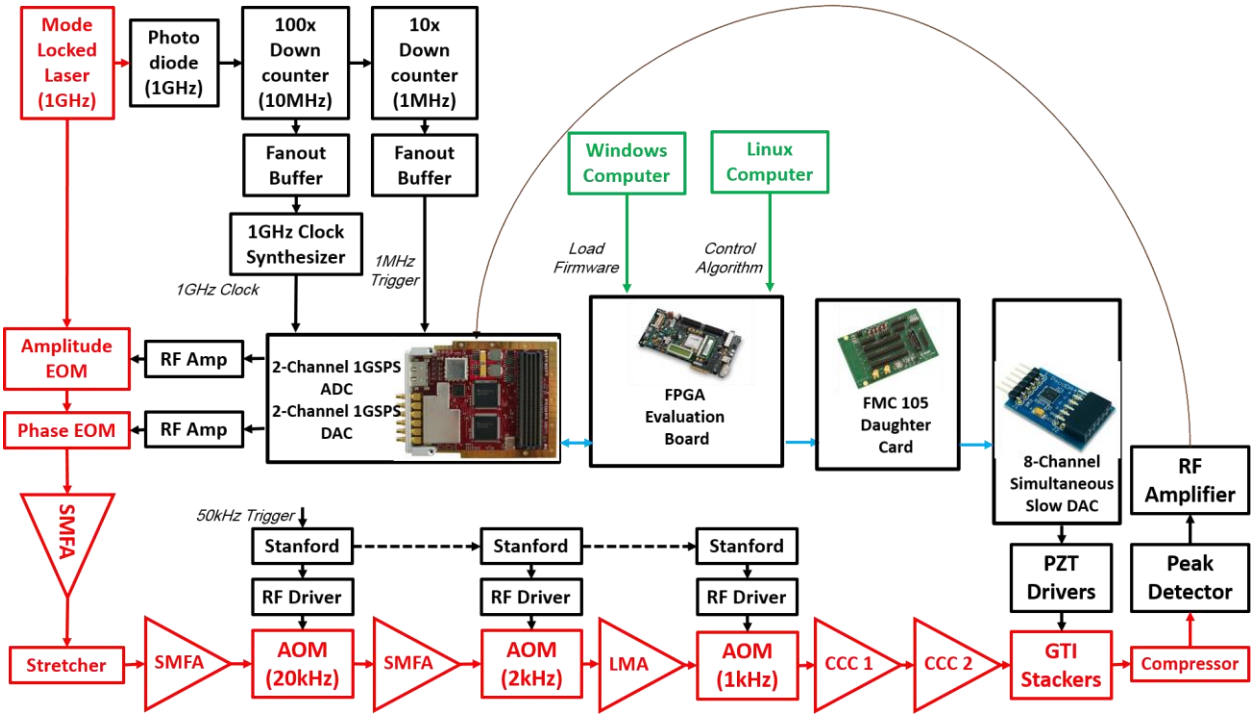

Figure 2.8: FPGA-Based Hardware Structure with Experimental Setup

The sampling clock, which is the master clock signal, is supplied externally by the laser oscillator to enable simultaneous sampling at a rate of 1 GSps (~977.8 MSps). A trigger signal at MHz repetition rate, which is derived from the master clock, determines the repetition rate at which the phase and amplitude waveforms are loaded into the Electro Optic Modulators (EOMs). In addition, through a firmware-based down counting, the 1MHz trigger signal is converted to a 50KHz trigger to enable the ADC reads the SHG signal at 50KHz.The XM105 Debug Card is designed to provide a number of multi-position headers and connectors which output FPGA interface signals to slow DACs (which drive the cavity PZTs).

Firmware and Software Development for the FPGA Based Control System

In this section, I collaborated with the Lawrence Berkeley National Laboratory. The FPGA firmware can be divided into three layers:

The 1st layer (bottom one) is where all the required hardware drivers need to be transferred into a firmware. Here the firmware is inherited from the FMC110 (1GHz ADC and DAC each one 2 channels).

The 2nd layer (Middle One) is the layer where encoding and decoding of the data is done. The FPGA needs to encode the acquired digital data via 1GHz ADC and the central host PC needs on the other side needs to decode them. A UDP-based protocol firmware/software has also been developed for the data transmission and communication of the ML605 and the host PC.

The 1st layer (Top One) in the firmware contains a control program functioning as a digital signal processor for stabilization and optimization purposes in CPSA system. In this layer, two different buffers have been employed to accommodate the required two-sided data transmission between the central PC (as the host) and the hardware (including the FPGA evaluation board, fast ADC, fast DAC, and slow DACs). Specifically an ADC buffer has been developed to provide a fast and synchronous exchange of data from the ADC to the central PC, and a DAC buffer has been developed to provide a secure and fast data transfer from the central PC to the DAC side. A serial-peripheral interface (SPI) has also been made to serialize the generated digital data and clocking them into the ad5628 DAC. On the software side, we implemented all the control algorithms on PC utilizing Python and communicating with the FPGA system via Ethernet.

Chapter 3 System Noise Characterisation Techniques

3.1 Phase Noise Measurement Technique Using a GTI Stacker

Studying and understanding the sources of noise and disturbances, and their effect at the output is a crucial step in control systems for improving the system performance. In electrical systems noise behavior in different time and frequency regions is investigated to fully characterize it and subsequently minimize it. In this section we are primarily interested in understanding how much noise (in radians) from the oscillator pulse train and the GTI cavities appear in the measurements of our system metric and for that we will use a technique which is based on the characteristics of the GTI stacker cavity or the Oscillator Cavity.

This section starts with mathematical representation of the oscillator pulse train . Time domain electric field of the oscillator pulse train can be written as follows in the absence of any kind of noise [38,39,40]:

$$A(t) = A_0 \sum_{m=-\infty}^{\infty} a(t - mT_R) e^{i(\omega_c t + m\Phi_{CE})} \tag{3.1}$$

As shown above the pulse train consists of number of pulses with amplitude A_0, and the terms inside the summation are the envelopes of the pulses $a(t)$ and the propagation part represented by the exponential function.T_R is the pulse repetition period, ω_c is the angular carrier frequency, and Φ_{CE} is the pulse-to-pulse carrier envelope phase slip which is the mismatch from the peak of the envelope. In the frequency domain, it is equivalent to the carrier envelope offset frequency $\omega_{CEO} = \Phi_{CE} * f_{rep}$. Now, since the phase velocity v_p and the group velocity v_g for the

pulse train are not equal, the pulse repetition period T_R does not necessarily correspond to an integer number of wavelengths. This is the origin of the carrier-envelope offset which shifts the frequency comb by $f_{CEO} = \left(\frac{1}{2\pi}\right) * \omega_{CEO}$. This representation can be visually shown as in the following figure 3.1.

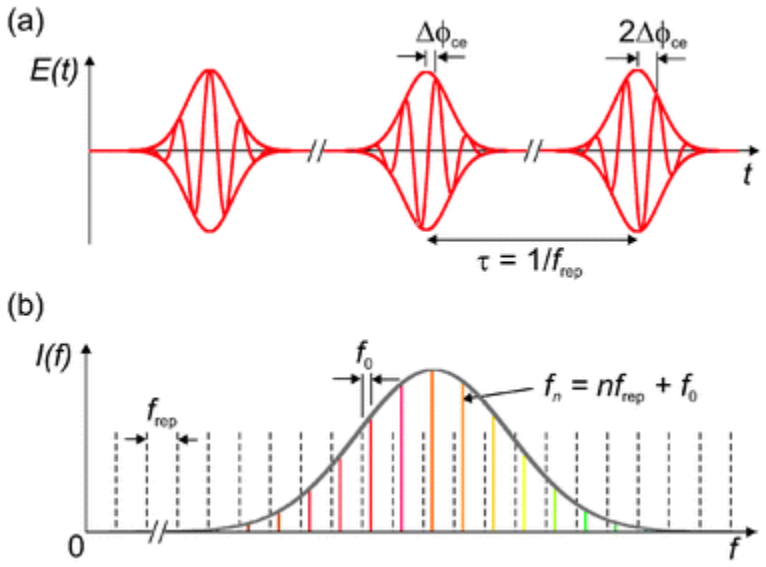

Figure 3.1: Time-frequency correspondence of the output from a femtosecond mode-locked laser.

The pulse train in equation 3.1 in the presence of noise will be as follows:

$$A(t) = [A_0 + \Delta A_0(t)] \sum_{m=-\infty}^{\infty} a\big(t - mT_R + \Delta T_R(t)\big) e^{i(\omega_c t + m\Phi_{CE} + \Delta\delta_{pulse}(t))} \quad (3.2)$$

Where $\Delta A_0(t)$ is the amplitude noise, $\Delta T_R(t)$ is the pulse timing jitter (the envelope delay which varies from pulse to pulse), and $\Delta\delta_{pulse}(t)$ represents the phase noise from the oscillator. These are the three different types of noise appearing in the oscillator pulse train.

Next, we describe the GTI stacker response which is dependent on both the cavity phase and the pulse train errors. Using equation (1.6) for a single cavity, in order to achieve ideal stacking, the output stacked pulse train is the convolution of the input pulse train $\tilde{A}^{in}[k]$ and the

cavity impulse response $\tilde{h}[n-k]$. The impulse response of a single lossless GTI cavity is the response of that cavity to a single pulse $\tilde{p}^{in}(t) = p_s(t)e^{i(\omega t+\phi_0)}$as follows:

$$\tilde{p}^{out}(t) = \sum_{n=0}^{\infty} \tilde{h}[n]\, p_s(t-nT_r)e^{i(\omega_0 t+\phi_0)} \tag{3.3}$$

$$\tilde{h}[n] = \begin{cases} r & for\ n = 0 \\ -r^{n-1}(1-r^2)e^{in\delta} & for\ n = 1,2,\dots \end{cases} \tag{3.4}$$

Where r is the square root of the cavity mirror reflectivity R, and δ is the round-trip phase. An ideal pulse stacker is essentially a GTI resonator with folding mirrors whose reflectivities are exactly unity which completely reflects the incident electric and hence no losses are exhibited. This ideal GTI cavity is represented by an impulse response in which its complex conjugate time reverse can produce a perfect stacked pulse (With no pre-pulse and infinite pre-pulse contrast) if transmitted as the input pulse train.

$$\tilde{p}^{in}(t) = \sum_{n=0}^{\infty} \widetilde{A^{in}}[n]\, p_s(t+nT_r)e^{i(\omega_0 t+\phi_0)} \tag{3.5}$$

$$\tilde{A}^{in}[n] = (\tilde{h}[-n])^* = \begin{cases} r & for\ n = 0 \\ -r^{-n-1}(1-r^2)e^{+in(\delta_{mod}-\omega_0 T_R)} & for\ n = -1,-2,\dots \end{cases} \tag{3.6}$$

Notice n's are negative, therefore $+in(\delta_{mod} - \omega_0 T_R)$ automatically accounts for conjugate. $\omega_0 T_R$ is due to the carrier envelop offset from the oscillator. We denote $\delta_{pulse} = \delta_{mod} - \omega_0 T_R$ to indicate that this is the phase difference between any two consecutive input pulses. As shown above, if $\delta_{pulse} = 2\pi m$ (m is an integer), the last pulse n=0 has 0 phase, and all the other pulses in the incident burst are in phase with each other and π degree out of phase with the last pulse. However, for the cases where the round-trip phase δ is not integer multiple of

2π, it is required to add complex conjugate of that δ to all pulses which is equivalent to have a linear phase ramp according to the $e^{i\delta}$ term in (3.4).

In general, the response of the GTI stacker to any arbitrary input signal $(\tilde{A}^{in}[0], \tilde{A}^{in}[1], \dots, \tilde{A}^{in}[n])$ can be calculated using the following convolution.

$$\tilde{A}^{out}[n] = \sum_{k=-\infty}^{n} \tilde{A}^{in}[k].\tilde{h}[n-k] \tag{3.7}$$

In general where we have phase mismatch $\left(\delta \neq \delta_{pulse}\right)$ the convolution formula leads to the following:

For n=0:

$$\tilde{A}^{out}[0] = A[0] * h[0] + A[-1] * h[1] + \cdots = r^2 + (1-r^2)^2 e^{i(\delta-\delta_{pulse})} + r^2(1-r^2)e^{i2(\delta-\delta_{pulse})} + r^4(1-r^2)e^{i3(\delta-\delta_{pulse})} + \cdots = r^2 + (1-r^2)^2\left(\frac{1}{1-r^2 e^{i(\delta-\delta_{pulse})}}\right) \tag{3.8}$$

For n<0:

$$\tilde{A}^{out}[n] = A[n]h[0] + A[n-1]h[1] + \cdots = (-r^{-n-1})(r)(1-r^2)e^{in\delta_{pulse}} + (r^{-n})(1-r^2)^2 e^{i(n-1)\delta_{pulse}} e^{i\delta} + (r^{-n+2})(1-r^2)e^{i(n-2)\delta_{pulse}} e^{i2\delta} + \cdots = -r^{-n}(1-r^2)e^{in\delta_{pulse}}(1-(1-r^2)(\frac{e^{i\left(\delta-\delta_{pulse}\right)}}{1-r^2 e^{i\left(\delta-\delta_{pulse}\right)}}) \tag{3.9}$$

For the cases, where there is matching between the round-trip phase of the stacker δ and round-trip phase of the oscillator δ_{pulse} (e.g $\delta = \delta_{pulse}$) , a perfect and ideal stacking is achieved. (e.g $\tilde{A}^{out}[0] = 1$ and $\tilde{A}^{out}[n] = 0$ for all n<0) as one can simply verify from the formula above.

Considerations of Different Noise Sources in the Oscillator

Amplitude Noise

It is not necessary to give mathematical derivations of amplitude noise as it can be directly measured by operating either at the peak or the minimum of the target function (e.g. second harmonic generation scan profile) where the derivative of the target function with respect to the phase is zero, thus enabling us to measure the amplitude noise from the oscillator. (this part will be explained in further detail explained throughout this chapter).

The effect of the amplitude noise in the oscillator can also be investigated by treating it as an added small-amplitude waveform to the original oscillator pulse train. Since the convolution is a linear operator, this amplitude noise can be convolved with the impulse response and affects the stacked pulse and the pre-pulses as follows:

$$\tilde{A}^{out}[n] = \sum_{k=-\infty}^{n} (\widetilde{A}^{in}[k] + \Delta\tilde{A}^{in}[k]).\tilde{h}[n-k] =$$

$$\sum_{k=-\infty}^{n} \tilde{A}^{in}[k].\tilde{h}[n-k] + \sum_{k=-\infty}^{n} \Delta\tilde{A}^{in}[k].\tilde{h}[n-k] \quad (3.10)$$

In the formula above $\sum_{k=-\infty}^{n} \Delta\tilde{A}^{in}[k].\tilde{h}[n-k]$ determines the effect of the amplitude noise on the stacked pulse, pre-pulses, and accordingly on the target function. The target function chosen here is a second harmonic generation (SHG) signal which is a peak-power metric. This signal is proportional to the intensity squared of the stacked pulse train.

Jitter Noise (envelope noise)

Jitter builds up over time. Jitter over the burst duration (e.g. ~ 100ns) is negligible. Therefore, the jitter within the bursts can be ignored. The jitter between the bursts are clearly large;

however, this jitter is exactly the same for all the pulses within the bursts therefore the effect of the jitter noise is ignored in the stacking.

Phase Noise

Phase noise can be considered as GTI cavity phase noise, oscillator phase noise within the burst and the oscillator phase noise between the bursts. First, the GTI cavity phase drifts slowly due to mechanical fluctuations in the stacker system. However, on the oscillator side, in addition to the oscillator cavity phase drifts, there are more noise sources such as white noise from the pumping, heating noise (diodes thermal noise), noise from the gain medium, etc. This manifests that there is much more contribution to the total phase noise in the stacking system compared to the GTI cavity phase noise. This will be supported by experimental results throughout the thesis as well. However, all these noise sources within a given short burst duration (e.g ~ 100ns) will be negligible. Further measurements will also show that a control speed in kHz range is sufficient to compensate the effect of phase noise in the oscillator which means that the in-burst phase noise (in GHz range) is negligible.

Between bursts, the oscillator cavity drifts due to changes in the gain medium, changes in the pump level, temperature changes, or the mechanical drifts of components. This effect can be represented in δ_{pulse} where its value is fixed for all bursts, but they are slightly mismatched from the the GTI cavity δ.

For the case where we use longer GTI stacker length (e.g. 9 times longer with Heriot Cavities) compared to the oscillator length, the same phase mismatch in the equal-length case produce noise which is effectively N times larger. This causes the measurement to be more sensitive to the oscillator noise. Therefore, for increasing the sensitivity of the measurements one

can use longer GTIs. This can be also understood through the mathematical derivations in (3.8) and (3.9) where δ_{pulse} changes into $N * \delta_{pulse}$ where the GTI stacker is N times longer than the oscillator cavity length.

Phase Noise in the Pulse Train and the GTI Cavity Stacker

In order to take into account, the additive effect of noise in the GTI cavity round-trip phases and oscillator pulses, equations (3.7) and (3.8) will change into the following respectively:

$$\tilde{A}^{out}[0] + \tilde{A}_0^{out}(t) = r^2 + (1-r^2)^2 \left(\frac{1}{1-r^2 e^{i(\delta+\Delta\delta(t)-\delta_{pulse}-\Delta\delta_{pulse}(t))}}\right) \tag{3.11}$$

$$\tilde{A}^{out}[n<0] + \tilde{A}_0^{out}(t) = -r^n(1-r^2)e^{in(\Delta\delta_{pulse}+\Delta\delta_{pulse}(t))}(1-(1-r^2)(\frac{e^{i\left(\delta+\Delta\delta(t)-\delta_{pulse}-\Delta\delta_{pulse}(t)\right)}}{1-r^2 e^{i\left(\delta+\Delta\delta(t)-\delta_{pulse}-\Delta\delta_{pulse}(t)\right)}}) \tag{3.12}$$

The most basic requirements for a noise measurement system are a metric function (which is sensitive to the control parameter, in this case cavity round-trip phase or the oscillator pulse round-trip phase) and a technique that determines how to measure the phase noise. Here we choose second harmonic signal as the metric since it is a function of the cavity and pulse phases and we retrieve the phase noise from that in the following way.

Any changes in the round-trip length of the GTI stackers or equivalently the oscillator cavity length would result in changes in the output stacked profile. Taking advantage of that, a peak detector that simply integrates the intensity squared over the stacked burst is a suitable choice to obtain the Second Harmonic Generation (SHG) signal as the desired metric for the feedback controller since it is sensitive to the changes of the control parameters and can be considered as mimic of a sum of the intensities squared. J=$SHG(r, \delta, \delta_{pulse})$.

$$J = \sum_{n=-\infty}^{n=0} (\tilde{A}^{out}[n].(\tilde{A}^{out}[n])^*)^2 \quad (3.13)$$

Plugging equations (3.7) and (3.8) into equation (3.9) leads to a symmetric profile of the metric signal with respect to δ and δ_{pulse} meaning that scanning through either of them while fixing the other results in the same profile in the metric function. An example of the scanning profile is as follows where either δ or δ_{pulse} are scanned over a full period of 2π.

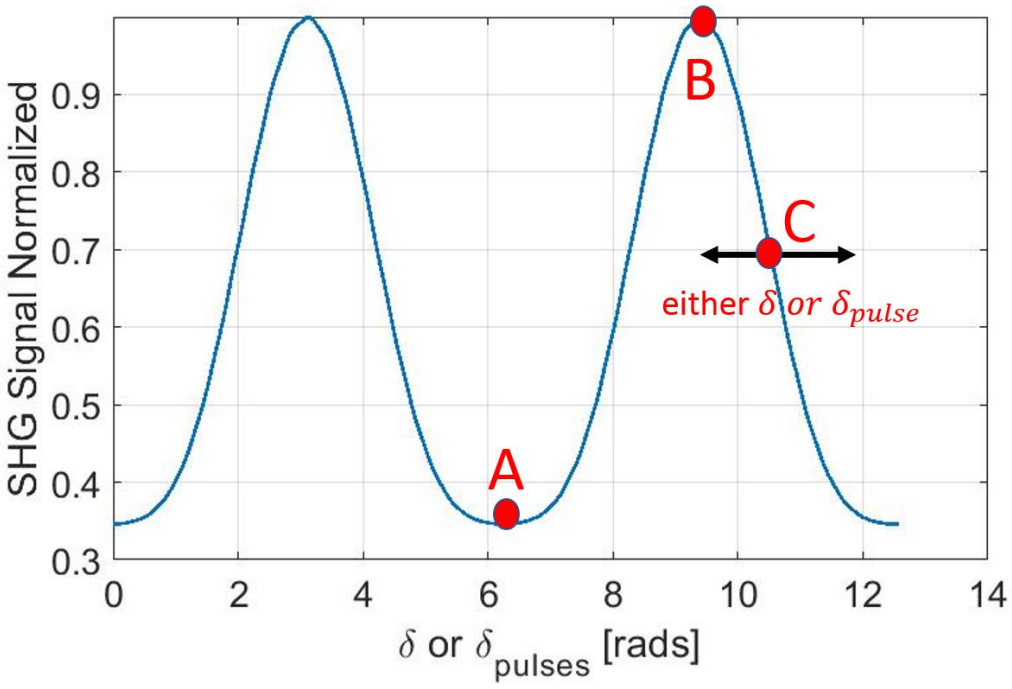

Figure 3.2: phase scan profile for measuring either GTI cavity phase noise or the Oscillator phase noise

In order to measure the phase noise either from the GTI stacker or from the oscillator, the measurement system scans through the phase values for at least two 2π periods and the SHG is accordingly measured. Fig 3.2 shows a simulated scan profile where the phases of a single GTI stacker or the oscillator cavity has been scanned for more than 4π radians.

In a real measurement, the initial scanning is performed to capture the profile of the either GTI cavity or the Oscillator Cavity. If the scan is released roughly halfway between the maximum and

minimum SHG signal (since this is where the signal is most linear) the measurement of the drift in the SHG signal for a certain amount of time correspond to a measurement of the combined phase noise.

For this part, we have developed firmware for the FPGA control system that enables us to acquire data as fast as the external trigger signal. The measurement results shown in the subsequent sections have all been performed with 50 kHz acquisition rate. The following plot is the drift of the SHG signal associated with the scan in Fig 3.2, and being initiated at point C.

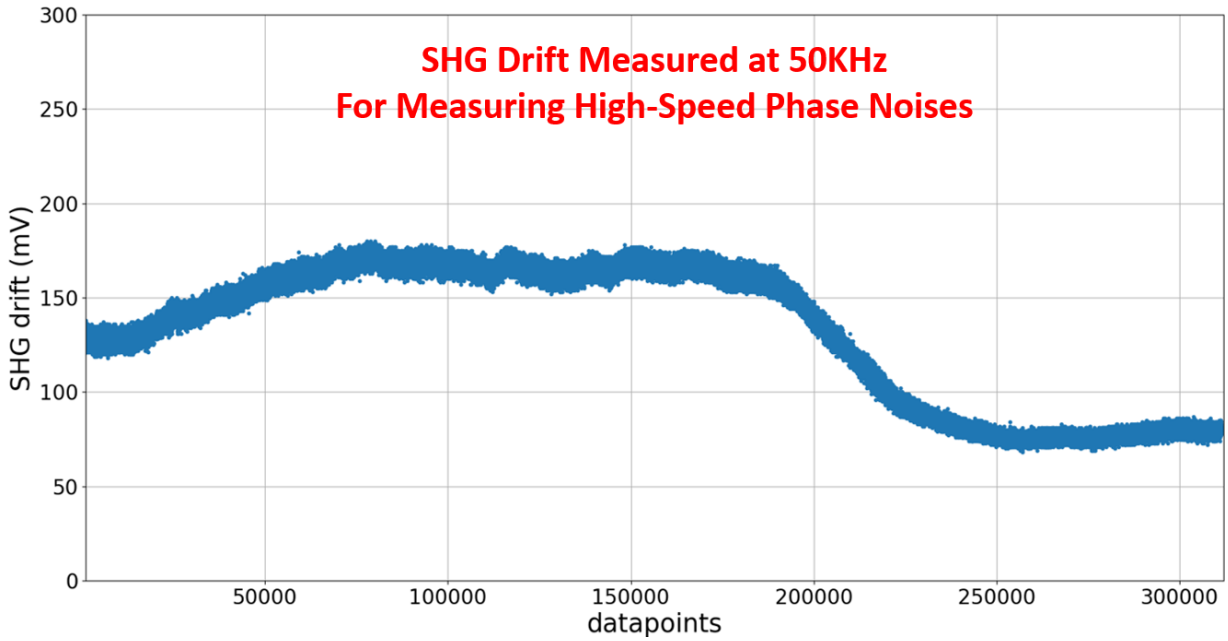

Figure 3.3: an example of the SHG drift signal that starts beginning as the phase scan stops at point C in Fig 3.2.

Using the scan data (e.g. Fig 3.2) the measured drift signal (e.g. Fig 3.3) is converted to corresponding phase noise in radians by noting that the scan signal is 2π periodic in the cavity phase. In order to do that two approaches can be taken. In the first approach a pair of successive maximum and minimum values in the SHG signal is located and subsequently an adjacent pair of maxima (or minima) also located. Then it is guaranteed that there is a 2π phase difference between a pair of maxima (or minima), so the phase difference between the successive maxima and minima

can be determined (e.g. it is π rads for simulation of Fig 3.2). experimental evidence shows that voltage changes almost linearly with the phase between the maximum and minimum SHG values, so all the voltages measured in the drift file can be converted to a phase value (within the allowed phase values which are between 0 and π for the above plot). This method is less precise (due to not perfect linear behavior of the SHG versus phase), but also less sensitive to system noise (amplitude noise from laser) since the data are collected away from the maxima and minima.

The other approach that can be taken is based on interpolation. With this method we use a scan file with some smoothing. Then we scale it so that the maximum value from the scan file is equal to the maximum value of the drift file. Once this is done, interpolation can be done to determine the phase values corresponding to a specific voltage value (again within the allowed phase values, which are between 0 and π in Fig 3.2). This method might be more precise but could also be more sensitive to system noise (amplitude noise from laser) causing problems in the conversion.

For simplicity we use the first approach without applying any interpolation and the phase noise can be retrieved as follows:

$$\Delta\delta(t)\ or\ \Delta\delta_{pulse}(t) = \big(J(t) - J(C)\big) * \left(\frac{\pi}{J(A)-J(B)}\right) \tag{3.14}$$

3.2 Time-Domain and Frequency-Domain Representations of System Noise

Noise analysis or measuring frequency instability in any optical system might be done in either the time domain or the frequency domain. A detailed description of how each of these approaches work is presented below and compared.

Time Domain

We have been analyzing noise effects by classifying them into different components and measuring the system response to each individual one. This procedure though is carried out either in time or frequency domain. Here we present a time-domain based technique called Allen Deviation mainly due to the fact our coherent combining technique has been fundamentally established as a time-domain approach. This Allen Deviation technique can effectively shed light on specific averaged time periods (~ equivalently frequency bands) where the system behaves more stably and hence better to operate at. This feature is rarely easily achieved via other noise-analysis approaches. This approach utilizes a log graph presenting the amount of noise in dB versus a quantity which is the averaged time (will be further explained throughout the chapter). Different regions of these graphs tend to correspond to different noise types with specific slopes namely white phase, flicker phase, white frequency, flicker frequency, and 1/f low frequency noise components.

Here is the sequence of steps for classifying and clustering a data set for making a Allan Deviation graph.

Step 1: Experimentally sample the drift of the metric $y_i's$ (e.g SHG signal) for a certain period of time. N is the number of samples and τ_0 is the sample period. (e.g $\tau_0 = \frac{1}{50KHz}$). These samples will be used in the remaining computational steps.

Step 2: Set the average time to be $\tau = m\tau_0$ where m is the averaging factor.

Step 3: Divide the time history of the sampled SHG signal into clusters of finite time durations $\tau = m\tau_0$. Clustering the sequence can be done in two different ways. Overlapping and Nonoverlapping. In the overlapping version, the time stride between two consecutive data clusters are always equal to the sample period τ_0. For instance, Figure 3.4 shows a typical overlapping data clustering with averaging factor m=3.

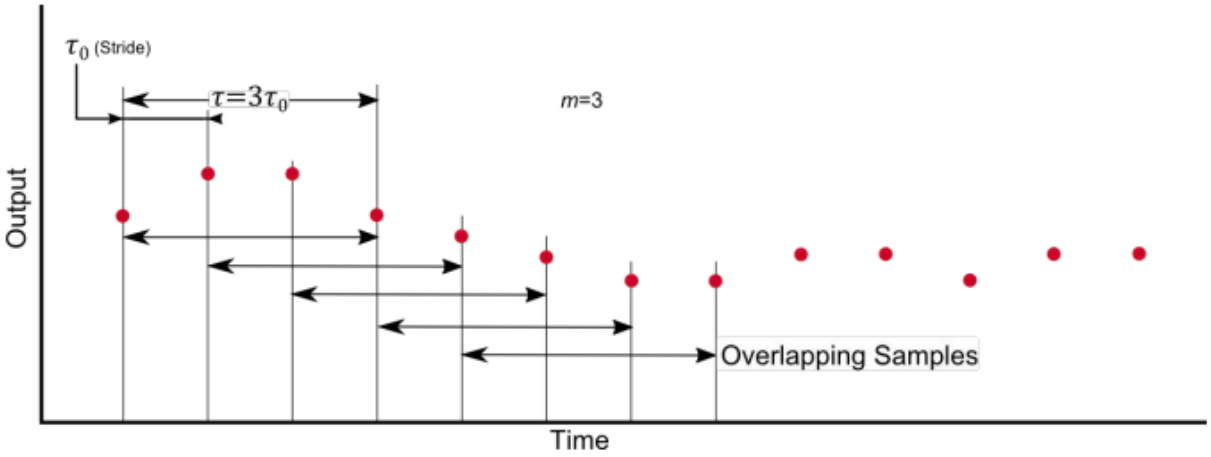

Figure 3.4: Clustering the raw noise data for applying Allen Deviation process

Step 4: Once the clusters are formed, first take the average of each clusters and call them $y_i's$.

Step 5: In the final step, Allen values corresponding to different selections of "m" are calculated using the following formula. Notice that $y_i's$ under the square root represent the average value of each cluster containing m elements, and M is the total number of clusters. (Notice that specifically for this section we do not denote the number of cavities by M). Once the Allen values for all m's are calculated, a log graph of the $\sigma's$ shows the magnitude of noise corresponding to different random processes in dB scale.

$$\sigma(y) = \sqrt{\frac{1}{M-1}\Sigma(y_{i+1} - y_i)^2} \tag{3.15}$$

As shown in Figure 3.5, slopes of -1 and -0.5 approximately correspond respectively to white phase and frequency noises in the system which are mainly due to the spontaneous emission and are considered as high frequency noise. On the other side, slopes of 0 and 1 correspond to 1/f or flicker noises which is typically due to the low-frequency drift in the system set-up such as mechanical drifts of the cavities.

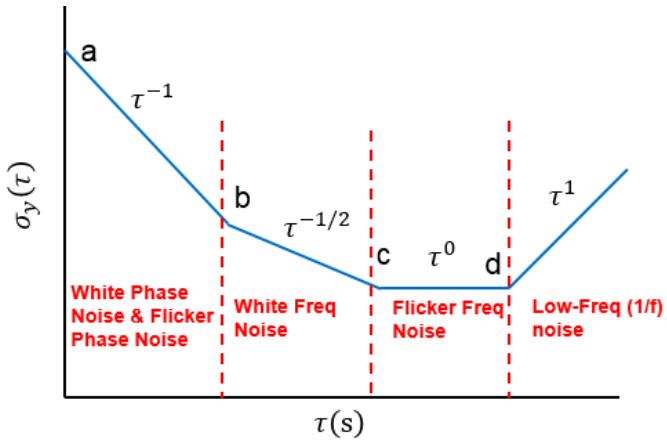

Figure 3.5: Different regions of the Allen Deviation plot

For better understanding the Allen Deviation graph, a few points have been labeled on Figure 3.5. Point a) as it corresponds to m=1 shows the magnitude of the noise with no averaging taken on the dataset. Variation of values among larger number of clusters is feasibly larger and hence m=1 usually is the maximum value on the graph.

Point b) in contrast is when m>1 and M clusters each containing m data points have been averaged and the corresponding Allen value is the standard deviation among these averaged values. This points out that the user can effectively degrade the noise effect by taking more and more averages.

Point d) finally is where a small number of clusters are taken and the variation among them will be small compared to the previous m values.

The following example shows how this phase measurement technique works along with the time domain-based noise analysis approach (Allen Deviation).

Frequency Domain

Once the time history of the drift signal (e.g SHG(t)) is sampled, one can also find the Fourier Transform of the time domain signal utilizing the Fast Fourier Transformation FFT as

$FFT(k) = \sum_{n=1}^{N} x(n) e^{-i2*\pi*k*\frac{n}{N}}$. First, we normalize the average power of the data set input to the FFT to unity. Since the FFT is a symmetric function, it is sufficient to represent half of the spectrum as $FFT = FFT\left(1{:}\frac{N_{FFT}}{2}\right)$,where N_{FFT} is the total number of FFT points we choose which is the closest power of 2 to the size of our data set (N). $Freq = (0{:}\, N_{FFT}/2) * F_s/N_{FFT}$ is the frequency vector against which the FFT is plotted. F_s : The sampling frequency in which the data points in the time domain correspond to (e.g. Fs=50KHz).

The following examples illustrate how we can obtain the Fourier Representation of our time domain SHG (t).

The conversion from frequency domain measurements to time domain measurements utilizes an integral equation. The Allen Deviation plot described above can be also obtained using this integral equation. Leonard S.Cutler (1972) described the following conversion formula for frequency domain to time domain conversion [41,42,43].

$$\sigma_y^2(\tau) = 2\int_0^\infty S_y(f)\frac{\sin^4(\pi f\tau)}{(\pi f\tau)^2}\,df \qquad (3.16)$$

3.3 Example for Phase and Amplitude Measurements:

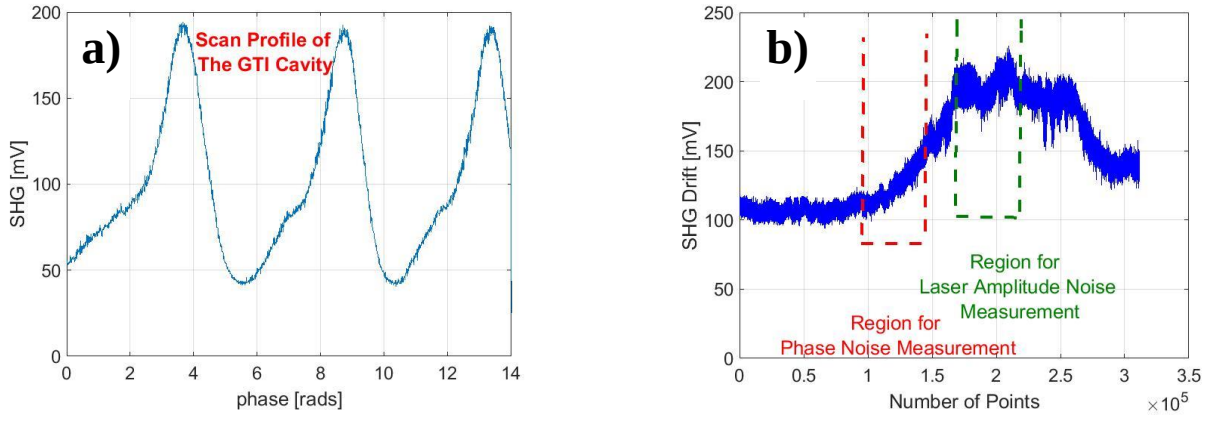

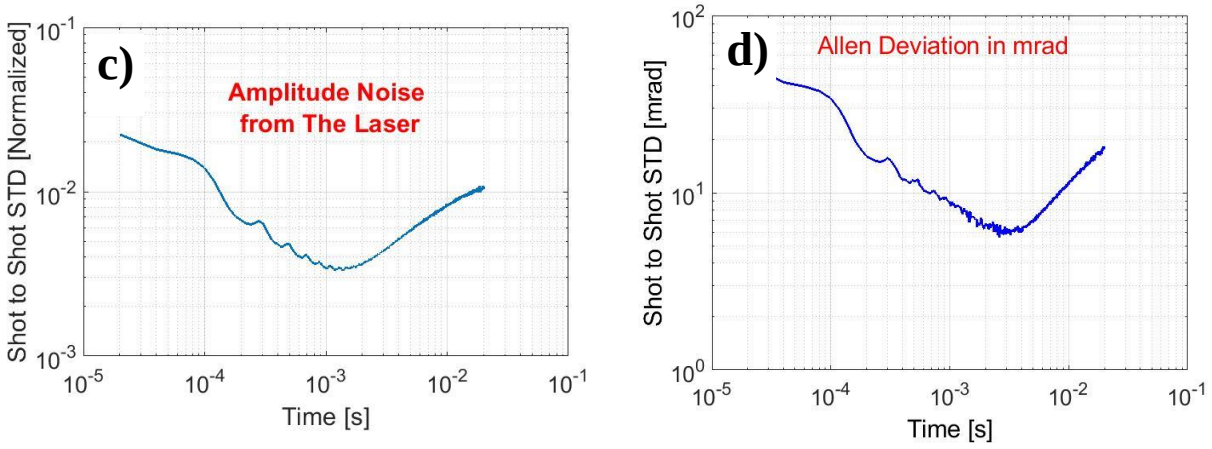

Figure 3.6: a) scan profile of the GTI stacker cavity for more than 4π period b) Second Harmonic Generation (SHG) sampled signal c) Normalized Allen Deviation Characteristics of the Amplitude Noise from the Oscillator. d) Allen Deviation Characteristics of the Stacking Phase noise in absolute mrad

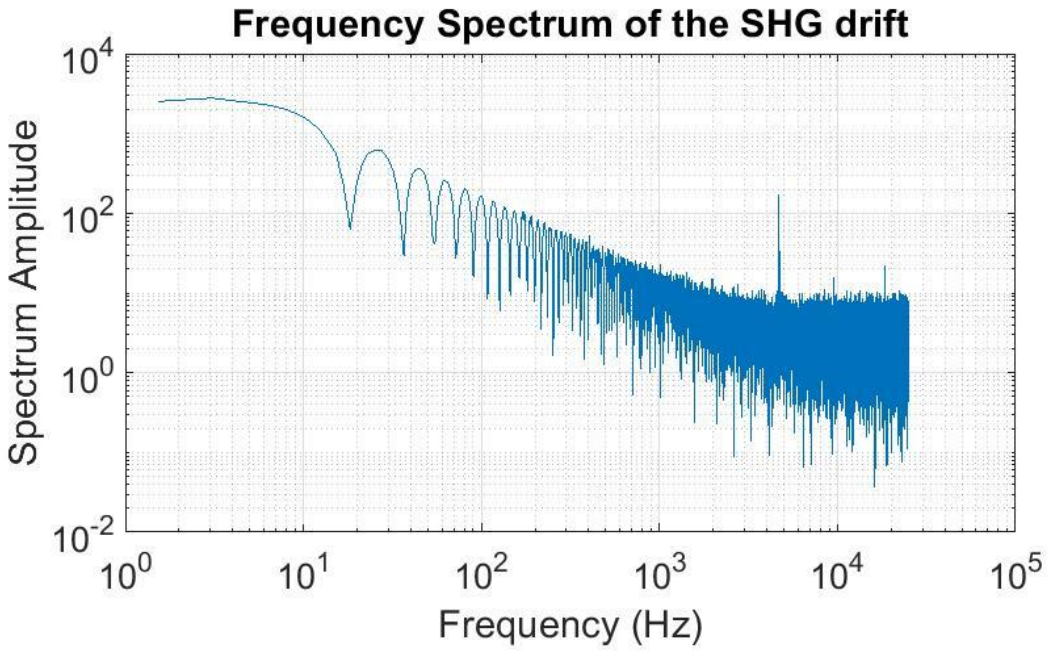

Figure 3.7: frequency spectrum of the SHG drift

In Figure 3.6 a) the scan profile of the GTI has been shown where the round-trip phase of the GTI stacker has been scanned for more than 4π radians by voltage modulating the PZT-mounted cavity mirror. Notice that during the scan time two consecutive maxima and two consecutive minima have been measured to be used for further conversion to corresponding phase

noise values in mrad. The scanning program has been developed such that it stops halfway between the SHG maximum and minimum. This ensures that the cavity works linearly and hence the drift of the second harmonic signal could give us the phase noise.

Figure 3.6 b) shows the measured drift of the SHG signal at 50KHz acquisition rate for about 6 seconds. For this measurement, the SHG signal is detected by a peak-power detector and sampled by a 1-GSPS ADC in conjunction with the FPGA system. Two different regions of the drift signal have been used for phase noise and amplitude noise measurement from the oscillator. The linear region is used to linearly converting the SHG values to corresponding phases in mrad and the peak region is used for measuring the amplitude noise from the laser where the SHG derivate with respect to δ or δ_{pulse} is zero.

Figure 3.6 c) and figure 3.6 d) are Allen Deviation of the amplitude noise and phase noise datasets respectively. Averaging factor m for this specific measurement as was explained previously is 1000 so that the resulting spectrum captures low-frequencies up to 50Hz. Comparing Fig 3.6 c) and Fig 3.6 d) one can verify that the amplitude noise from the laser is clearly much smaller compared to the phase noise from that existing in the measured SHG signal. Physical origin of this has been previously explained in this chapter. Figure d) consists of different frequency bands. For times larger than 0.004(s) or equivalently frequencies below around 600Hz which are considered as low-frequencies phase noise starts increasing approximately at τ^1 or equivalently 1/f (e.g 1/f noise). Mechanical drift in the GTI cavity or the oscillator cavity, it is expected to happen in this frequency band due to the fact these sorts of drift are slow compared to other sources of noise. For the times between 0.004(s) and 0.006(s) (600Hz ~ 800Hz) is the band where the stacking system experiences the least amount of noise hence it is suitable for stabilization purposes. For times smaller than 0.006s ($f > 800Hz$), as was noted previously, is the frequency band

associated with white noises (white phase and frequency noise). These high-frequency noises are expected to be primarily due to oscillator phase noise as noted in the beginning of this chapter.

As an alternative approach to the time-domain based Allen Deviation technique the measured noise can be analyzed in frequency domain using Fourier Transformation. Fig 3.7 is a single ended spectrum of the phase noise data which has been obtained with a sampling frequency of F_s =50KHz, a total number of $N_{FFT} = 2^{16} = 65536$ which is the closet power of two to the sampling frequency F_s.

3.4 Appendix A: Sensitivity Analysis of the SHG profile to Different Number of Input Pulses

Now let us analyze the sensitivity of our SHG signal to the cavity phase. The form of the SHG vs. cavity phase plot is in general sensitive to the number of pulses, the pulse intensities, and the pulse phases. Since here we want to have the SHG metric be only sensitive to the cavity phase, we can decide to have a specific number of pulses, relative pulse intensities and phases such that SHG is insensitive to pulse phase and amplitude when we scan through the cavity phases. In order to get a sense of the cases that gives minimum sensitivity to pulse phase and amplitudes, we present simulation results for a number of cases. All simulation results have been obtained based on a front-mirror reflectivity of R=0.55 for a single GTI stacker.

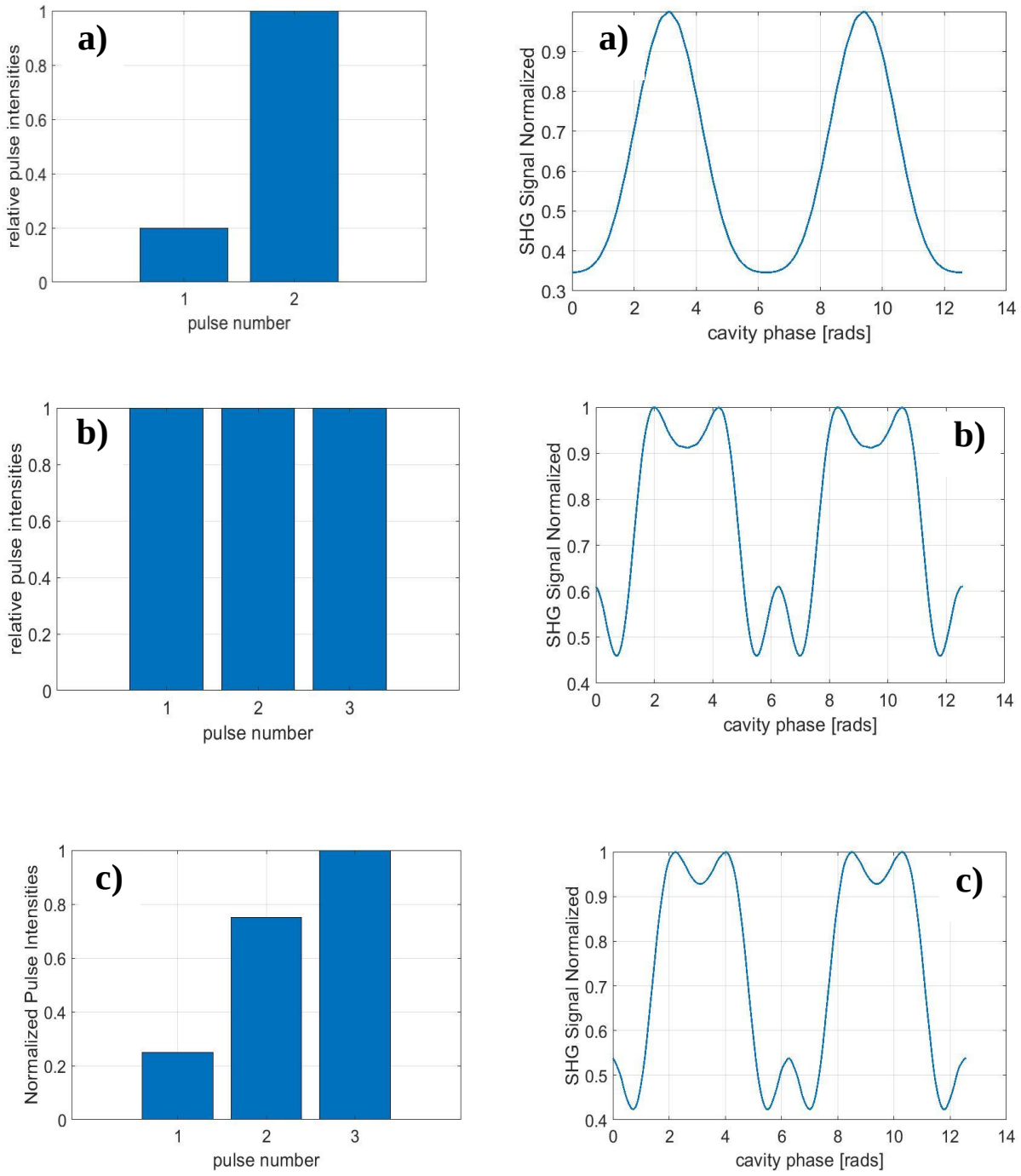

Figure 3.8: a) SHG phase profile with 2 pulse b) SHG phase profile with 3 equal-amplitude pulses c) SHG phase profile with 3 non-equal amplitudes

In the 2 pulse case (See Fig 3.8 a)), the SHG signal will be sensitive to the cavity phase, but will not be affected by the pulse phases (since the only interference that occurs is between the

1st and 2nd pulse). And furthermore, to have the SHG vs. cavity plot not have phase values where the SHG is insensitive to cavity phase (e.g. flat areas) as well as to not have multiple local maxima (or minima) in a 2π section, the relative pulse intensities are important. For that, we examined a profile such that the 2nd pulse has 5 times the intensity of the 1st pulse. This type of profile gives plenty of margin (5 times does not have to be exact, 4 or 6 times would work equally well), and has all of the nice features we want. In the 3-pulse case (See Fig 3.8 b) and 3.8 c)) as one can see in the SHG results, local maxima or minima are appearing in the SHG plot. These local maxim or minima should not be used when phase noise information is being retrieved from the SHG plot since the cavity is not behaving linearly in that region.

3.5 Appendix B: Sources of Noise that Could Affect the Stacking Fidelity

In this section some of the noise sources that can effectively degrade the stacking fidelity while it is under control. These sources can be categorized into three main divisions namely the sources that can affect peak detection accuracy, the sources that can affect burst amplitude and phase control accuracy, sources that place a limitation on having identical pulses in the burst, and finally the sources that affect the stacking interference contrast. The last two categories are not discussed here since they are out of the control-oriented tasks accomplished in this thesis. Instead the first two categories will be discussed in detail here.

Peak Detection Accuracy

As thoroughly explained in the control algorithms throughout the thesis, the metric signal detected by a peak detector plays a significantly important role in determining the direction the control system should take for both stabilizing the stacked pulse and optimizing the fidelity. Therefore any noise generated in the detection process will contribute to the stacking degradation.

Amplitude and Phase noise that have been extensively analyzed in chapter 3 and 4, can be considered as two first noise sources that can directly appear in the detected second harmonic generation signal.

The photodiode used for detecting the SHG signal generates some dark noise in the background that is read out by the ADC while measuring the photodiode output. The ADC itself produces Quantization error. Figure 3.9 shows the measurement result of the photodiode dark noise added to the ADC quantization noise. This clearly shows a p-p 10mV noise which will be added on top of any real SHG signal detected by the detector and quantized by the 1GSPS ADC.

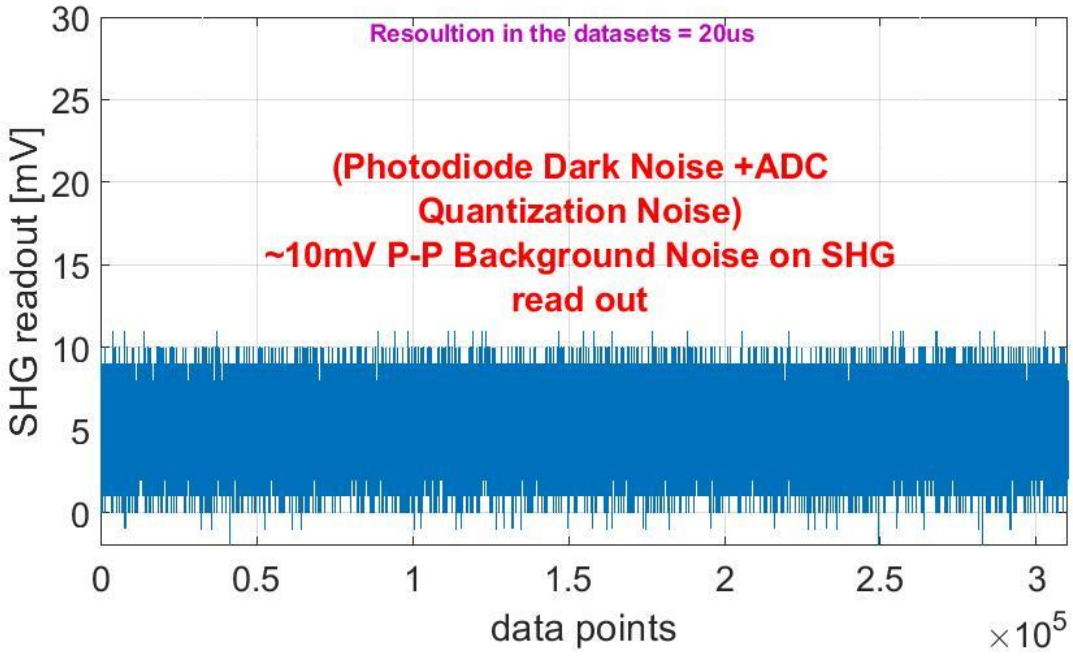

Figure 3.9: Measurement results for the photodiode dark noise and the ADC quantization noise

More specifically the 1GSPS ADC embedded in the FMC 110 in our control systems uses a 12bit 1GSPS ADC chip from Texas Instrument [44]. This specific chip has been characterized in terms of signal to noise ratio (SNR) in different clock p-p voltage ranges and input frequencies.

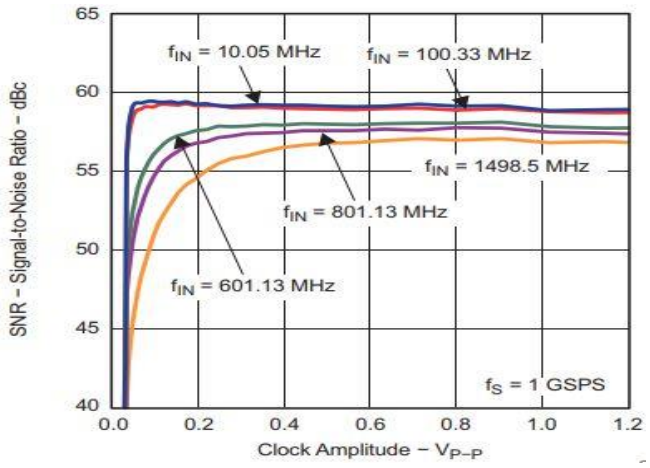

Figure 3.10: Signal-to-Noise (SNR) performance of the 1GHz ADC versus the peak-to-peak clock voltage at different input signal frequencies. [8]

As shown in figure 3.10 ADC gives an output SNR of around 57.5dBc at 800MHz (closest to our 977.8 MHz Oscillator repetition rate).

The other noise source that can be discussed in this category is the noise produced in dithering the PZT while the control algorithms are executed. Any noise in dithering gets amplified by the PZT amplifier before being applied on the PZTs. The PZT amplifier itself generates noise at the output which is added to the dithering noise.

Burst Amplitude and Phase Control Accuracy

To achieve a proper and accurate control on the burst amplitudes and phases many electronics devices are required to operate. The 1GSPS DAC which outputs the amplitude and phase waveforms, the RF amplifier that boosts the DAC output before inputting the waveforms onto the EOMs, and the noise of the EOMs or their output drift are 3 main noise sources that can effectively disturb the control on the input burst.

Chapter 4 Demonstration of Stable Stacking with Cascaded and Multiplexed GTI Configurations

4.1 Experimental Set-Up

In this chapter we will be presenting some experimental systems as well as their corresponding results achieved to demonstrate stable stacking. Specifically, the two experimental sets we will analyze in this chapter are first the 4-cascaded Cavity Set and second the 4+4 Multiplexed Set.

The experimental setup for the 4-cascaded-GTI-cavity scenario (See Fig 4.1) which targets stacking a burst of 9 pulses consists of a 1GHz (~988.8MHz) mode-locked oscillator generating femtosecond long pulses, two as-fast-as 10GHz electro-optic-modulators for imprinting required phase and amplitude modulation on the input pulses, , a grating based stretcher for stretching out the initially generated pulses to about nanosecond long levels, single mode fiber amplifiers, four cascaded 30cm-long GTI cavities designed and arranged in triangular fashion, and finally a peak detector for implementing the feedback control and stabilization system. This experimental setup is also further used for demonstrating the 4+4 multiplexed configuration for stacking up to 81 pulses and hence needs to be understood in depth. The initial chain of femtosecond long pulses at 988 MHz repetition rate are first modulated by the EOMs for both phase and amplitudes and then get stretched out by the specified stretcher. At this step the burst is ready to go under amplification through the single-mode fiber amplifier before getting compressed back to the femtosecond level at the final stage. The output of the SMFA is then transmitted through the GTI stackers for

stacking. The output beam after the last resonator goes into two paths, one for the compression and the other is taken as the objective signal for feedback implementation.

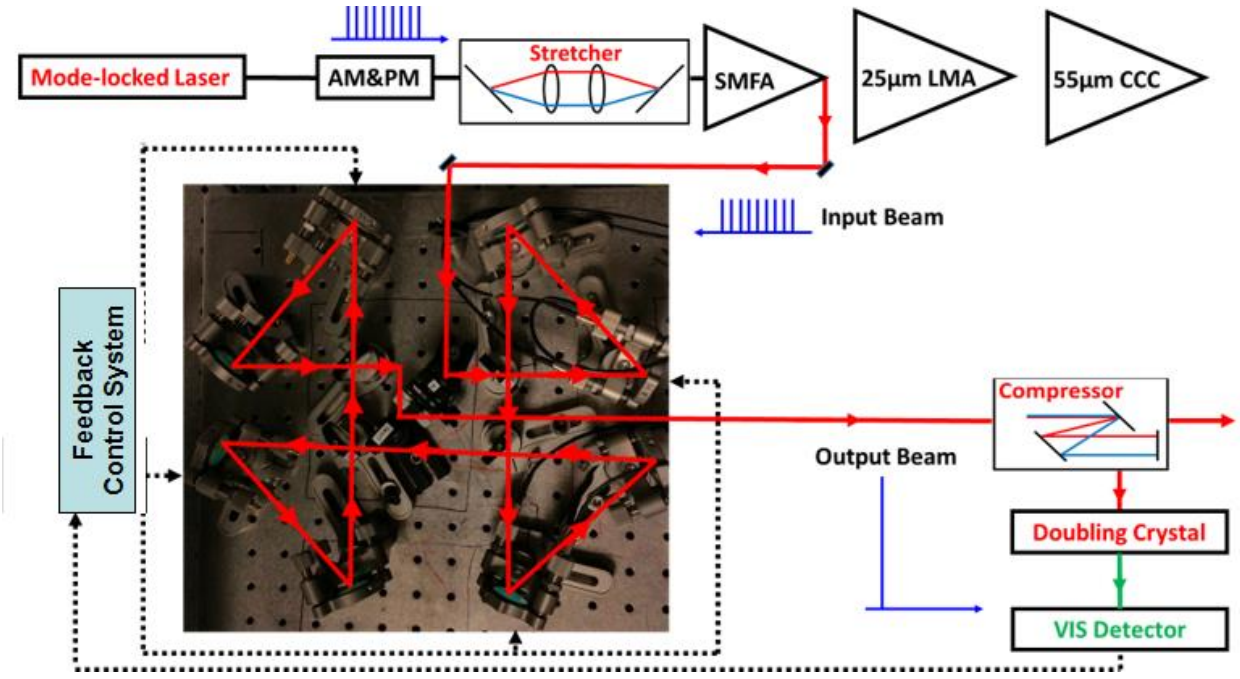

Figure 4.1: Experimental Setup for stabilization of 4-Cascaded GTI stacker system using either the All-Software-based control system using fixed National Instrument hardware set-up or the fast FPGA control system

The feedback control system shown above can be either the All-Software-based control system using fixed National Instrument hardware set-up or the fast FPGA control system where both systems have been in-detailed explained in chapter 2. In the first try we used the All-Software-Based approach to stabilize the system and the stable stacking was demonstrated at 200Hz feedback loop speed. After that, to be able to have more control on the feedback loop speed, and also having control on the scalability of our control system, we developed the FPGA control system.

Second experimental system is the 4+4 Multiplexed Configuration. The experimental setup for this scenario is made of two different sets of GTI cavities. The first set is exactly the same set

which was previously explained, four 30cm-long triangular cavities, and the second set is made of four 2.7m-long Heriot-based Cavities, where these two sets are configured in a multiplexed formation.

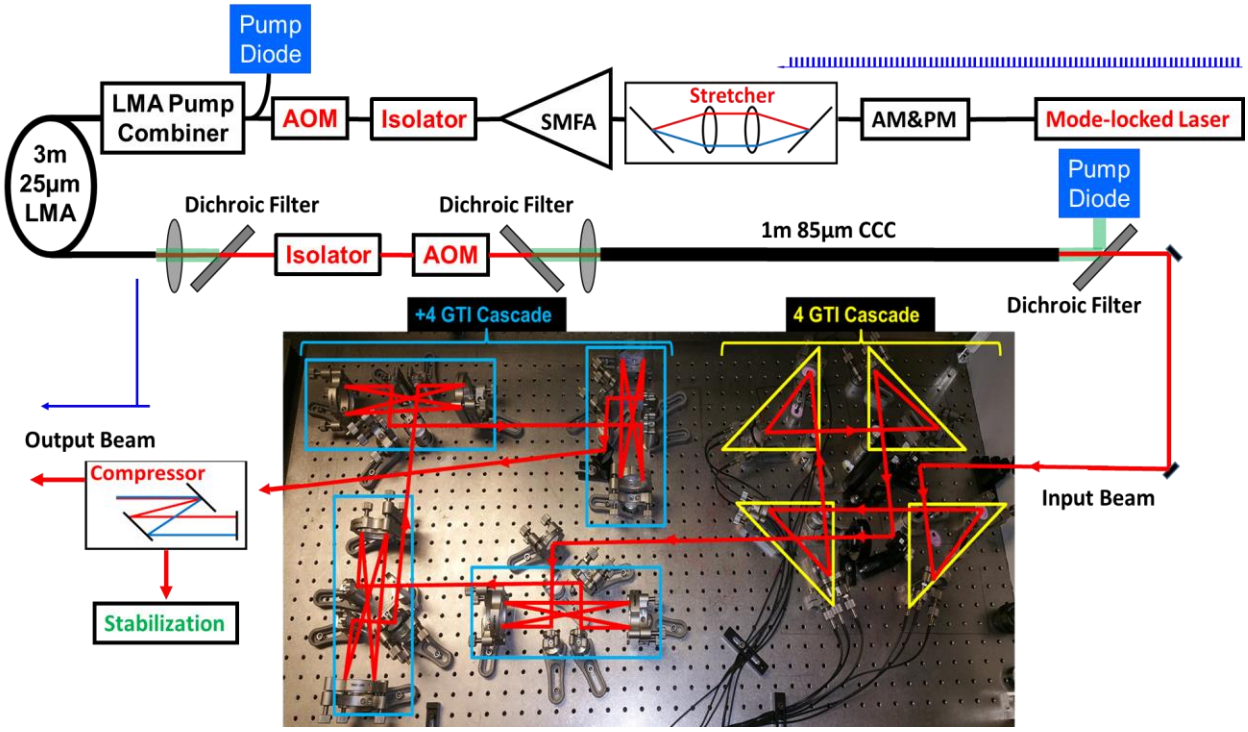

Figure 4.2: Experimental Setup for stabilization of 4+4 Multiplex of two different-length Cascaded GTI stacker sets using the fast FPGA control system

The setup is shown in figure 4.2. This experimental setup similar to the previous experiment starts with the same 1GHz (~988 MHz) mode-locked laser, same EOMs, stretcher and compressor designs. The fiber amplifier here is a 1m-long Chirally-Coupled-Core (CCC) fiber with 40um mode field diameter and 80um core diameter. The stabilization system here is the FPGA based Control System explained in chapter 2. The experiment was carried out for low energy at 1 MHz repetition rate.

4.2 Stacking Sensitivity to Cavity Phase, Pulse Phase and Signal Amplitude Errors

To better understand the complex stacking system, sensitivity of the output stacked burst to changes in different system parameters such as phase and amplitude errors in the input burst, and stacker round-trip phase needs to be investigated. For both 4-Cascaded GTIs, and 4+4 Multiplexed, sensitivity analysis in terms of particular metrics are presented. Peak power enhancement $P_{enhancement}$ and more importantly peak-power-based pre-pulse contrast $C_{pre-pulse}$ are evaluated for both scenarios under different errors and disturbance configurations. Notice that the input burst in this analysis consists of the main part of the burst as well as many other pulses in the tail. This has been particularly done such that evaluated metrics would not be dominantly sensitive to the first pre-pulse.

$$C_{pre-pulse} = \frac{I^{out}[N]}{\max\{I^{out}[1],\dots,I^{out}[2N-1]\}} \tag{4.1}$$

$$P_{enhancement} = \frac{I^{out}[N]}{\max\{I^{in}[1],\dots,I^{in}[N]\}} \tag{4.2}$$

In the equations above, $I[N]$ is the intensity which is just the magnitude of the Electric field squared. As it is clear, the peak-power enhancement is just the intensity of the N^{th} pulse divided by the maximum intensity in the input burst. The pre-pulse is just the intensity of the N^{th} pulse divided by the maximum intensity in the pre-pulses in the output burst.

The sensitivity analysis begins with an optimal design of stacker cavities, input phase profile, and input amplitude/intensity profile. It is important mentioning that the sensitivity to each parameter is investigated while other 2 parameters are kept unperturbed.

For sensitivity to the stacker cavity phase, a perturbation vector of standard deviations with normal random distribution is considered from 0 to 0.1. A randomly generated number associated with each of the standard deviations in this perturbation vector is simultaneously added to all 4 cavity phases in the case of 4-cascaded scenario, and to all 8 cavity phases in the case of 4+4 multiplexed scenario. This is done for 10000 times and the average of all the corresponding 10000

Pre-Pulse Contrasts or Peak-Power Enhancements associated with that particular standard deviation in the perturbation vector is a point in the sensitivity graph.

For sensitivity to pulse phase or pulse amplitudes, a perturbation vector similar to the previous case with the same distribution is considered. A randomly generated number associated with each standard deviation in the perturbation vector is simultaneously added to all the pulse phases or pulse amplitudes, simulation runs for 10000 times, and the average of all the 10000 corresponding Pre-Pulse Contrasts or Peak-Power Enhancements associated with that particular standard deviation in the perturbation vector is a point in the sensitivity graph.

The following results (See Fig 4.3 and 4.4) correspond to the 4-Cascaded Equal length Cavities. The parameters we have chosen for the simulation are as follows:

Front-Mirror Reflectivities: $R1 = 0.58,\ R2 = 0.59,\ R3 = 0.57,\ R4 = 0.58$

Cavity Phases: $\phi_1 = 4.65, \phi_2 = 3.15, \phi_3 = 5.46, \phi_4 = 0$

And the total number of pulses are 50.

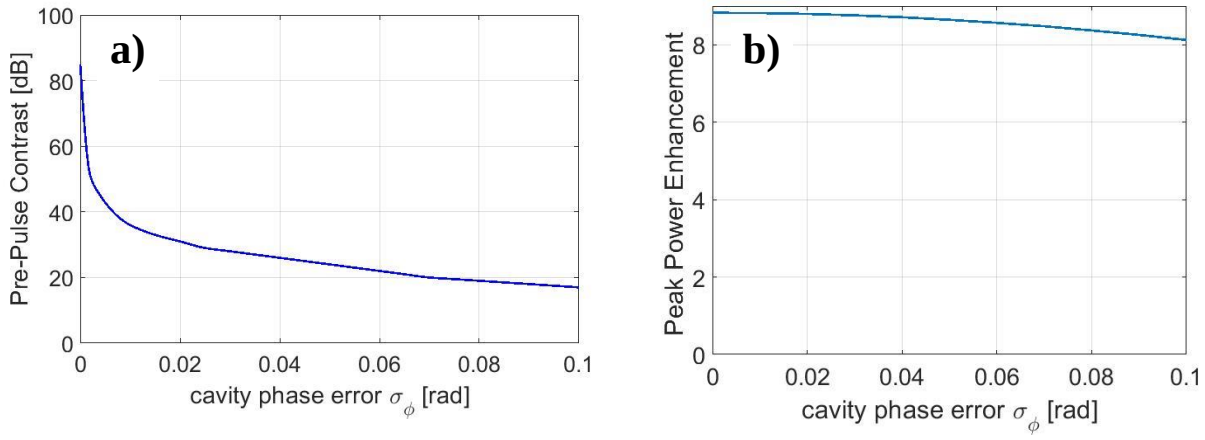

Figure 4.3: a) Pre-Pulse contrast versus cavity phase error for 4-Cascaded GTI cavity set. b) Peak Power Enhancement versus cavity phase error for 4-cascaded GTI cavity set

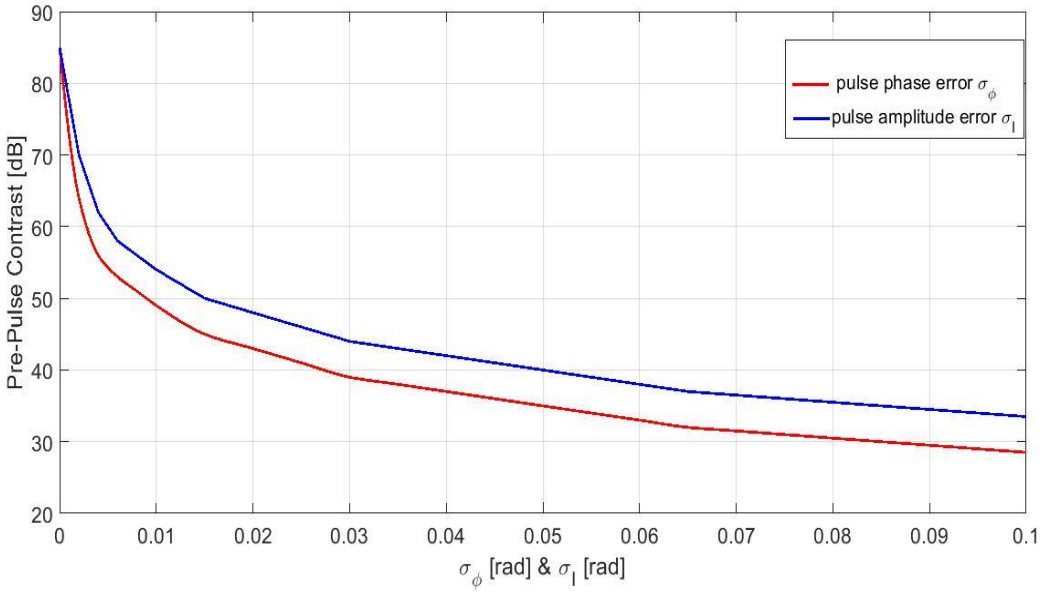

Figure 4.4: Pre-Pulse contrast versus pulse phase and amplitude errors for 4-Cascaded GTI cavity set

By looking into the simulation results in Fig 4.3 and Fig 4,4, we can see that more than 30dB pre-pulse contrast can be achieved if we have less 20mrad phase noise in the stacker whereas the same pre-pulse contrast can be achieved by having less than 80mrads phase noise in the input pulse phase. As a result, the pre-pulse contrast is clearly more sensitive to the cavity phase error than the input pulse phase and input pulse intensity errors. However, our recent experiments manifest the fact that our stacker cavities are quiet enough that such uncertainty in the cavity phases space does not happen. Now this means the sensitivity to the input pulse phase and amplitude matter a lot in our case.

Another source of uncertainty that could affect the stacking is the uncertainty in the front-mirror reflectivity (R). However, it is still possible to keep the pre-pulse contrast unchanged due

to the uncertainty in R and that is through optimizing the input pulse phase and amplitude profile. This will be explained in more details in chapter 5.

In the next part, we present the sensitivity results of the 4+4 multiplexed configuration with nonequal cavity length.

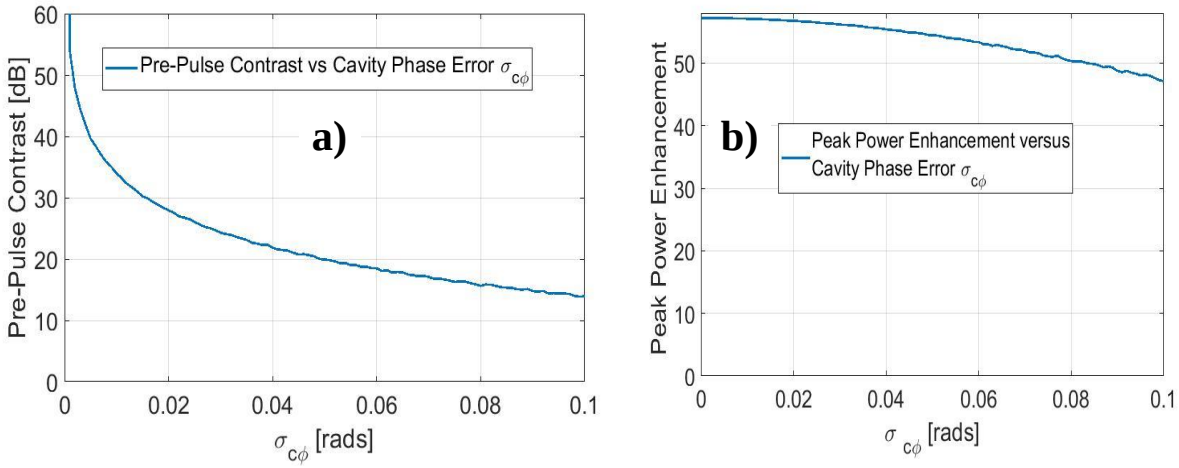

Figure 4.5: a) Pre-Pulse contrast versus cavity phase error for 4+4 Multiplexed GTI cavity set. b) Peak Power Enhancement versus cavity phase error for 4+4 Multiplexed GTI cavity set

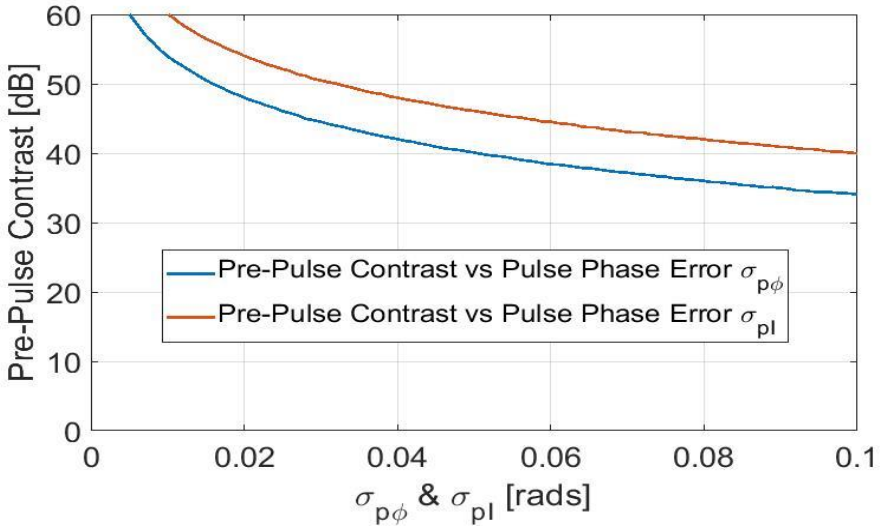

Figure 4.6: Pre-Pulse contrast versus pulse phase and amplitude errors for 4+4 Multiplexed GTI cavity set

The parameters we chose for the simulation results above are as follows:

Front-Mirror Reflectivities: $R1 = 0.58, R2 = 0.59, R3 = 0.33, R4 = 0.57, R5 = R1, R6 = R2, R7 = R3, R8 = R4$

Cavity Phases: $\phi_1 = \phi_5 = 4.65, \phi_2 = \phi_6 = 3.15,\ \phi_3 = \phi_7 = 5.46, \phi_4 = \phi_8 = 0$

And the total number of pulses are 500.

By comparing the sensitivity curves in the case of 4-Cascaded GTI and the case of 4+4 Multiplexed GTIs (Fig 4.5 and Fig 3.6) it is clear that the stacking is much more sensitive to the pulse phase and pulse intensity errors in the Multiplexed case. Same statement is valid for the cavity phase error as well.

4.3 Oscillator Noise Characterization, analysis, and improvement results

As it was mentioned in chapter 1, stacking large number of pulses and achieve using cascaded configuration would be very challenging since large number of GTI cavities will be required. For instance, to stack 81 pulses, 40 cascaded GTI cavities are required to get perfect stacking with exactly precise burst profile. Multiplexed GTI cavity configuration where it multiplexes a cascade of M equal-roundtrip GTI cavities with a second cascade of N-times longer Cavities, is one of the techniques where you can get an approximately precise burst profile by using much fewer cavities.

For stabilization purposes, stacking phase noise has to be sufficiently small so that the control system can find the required phase to stabilize the stacker system and stabilize it against the dominant noise which turns out to be oscillator phase noise. The 30cm Triangular Cavity who

round-trip length is equal to that of the oscillator has been stabilized in which the stabilization was limited to the amplitude noise of the oscillator. However, stabilizing the GTI cavity whose round-trip length was N times larger than that of the oscillator was initially challenging due to higher noise level measured in the peak power signal. Initial As it was explained in chapter 3, phase matching between the round-trip phase of the GTI cavity δ and that of the oscillator δ_{pulse} should be achieved to get stacking. Such phase mismatch is considered as noise in stabilization purposes.

$$\tilde{A}^{in}[n] = \begin{cases} r & for\ n = 0 \\ -r^{-n-1}(1-r^2)e^{+in\delta_{pulse}} & for\ n = -1, -2, \dots \end{cases} \tag{4.3}$$

$$\tilde{A}^{out}[0] = r^2 + (1-r^2)^2 \left(\frac{1}{1-r^2 e^{i(\delta-\delta_{pulse})}}\right) \tag{4.4}$$

$$\tilde{A}^{in}[n<0] = (1-r^2)e^{in\delta_{pulse}}(1-(1-r^2)(\frac{e^{i(\delta-\delta_{pulse})}}{1-r^2 e^{i(\delta-\delta_{pulse})}}) \tag{4.5}$$

By looking at the equations above, one can verify that for the case where the GTI round-trip is N (e.g. ~ N=9) time longer, the phase factor δ_{pulse} gets magnified by factor of N and turns into $9\delta_{pulse}$. This magnification effect for the phase causes the measurement to be more sensitive to the oscillator noise.

In this part, experimental results of measuring stacking phase noise with equal length (e.g. ~ L=30cm) and 9-times longer length GTI cavity (L=2.7m) are presented. will be shown how sensitive this longer cavity reacts to the phase noise from the oscillator.

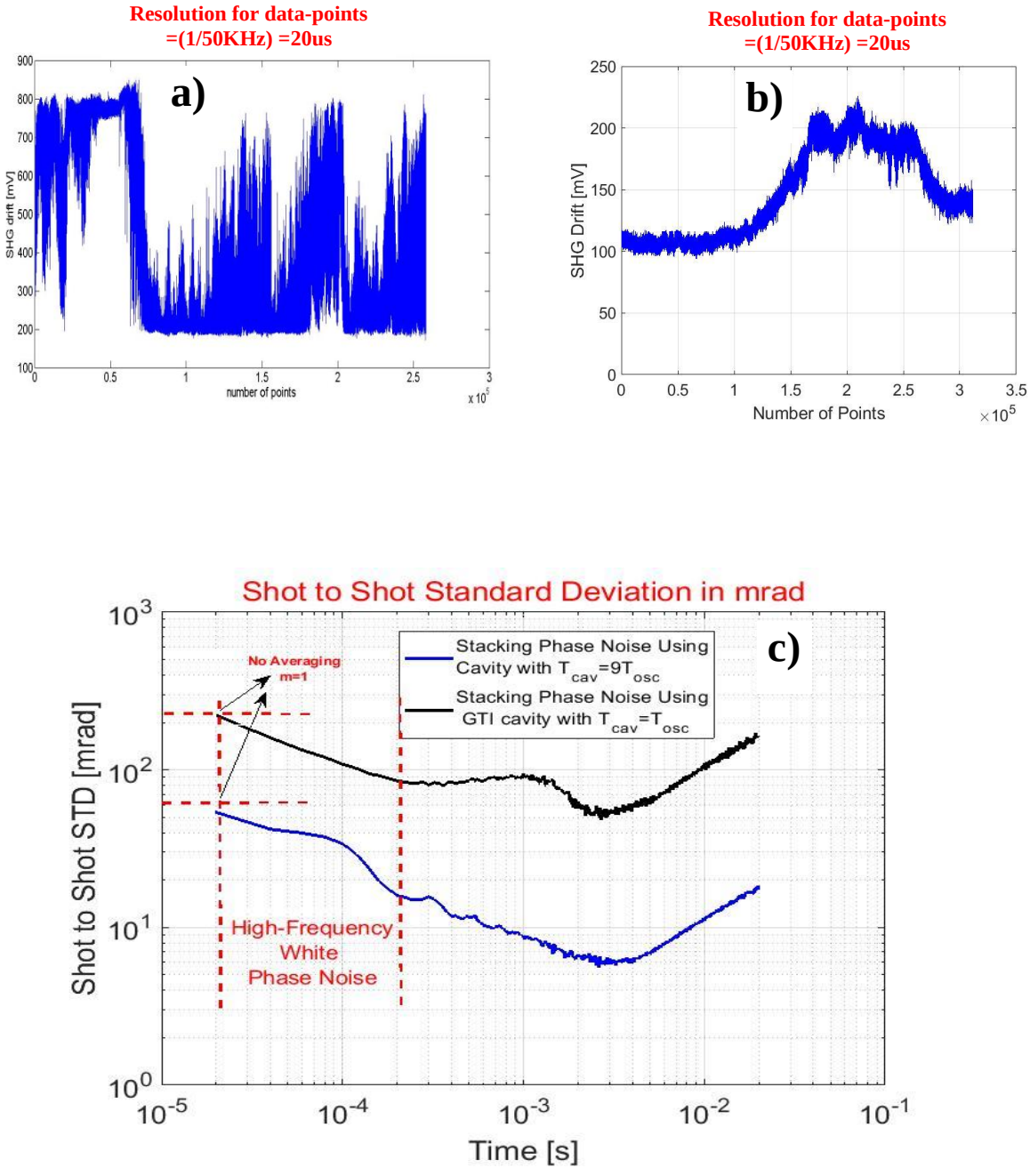

Figure 4.7: a) SHG drift using 2.7m cavity b) SHG drift using 30cm cavity c) Allen Deviation Characterization of the absolute stacking phase noise and comparison

Figure 4.7 a) and 4.7 b) above shows the second harmonic generation (SHG) signal drift for two different-length Cavity. One thing which is important to mention is such large fluctuations shown in figure 4.7 a) is not only due to the phase noise contribution from the oscillator but also due to other sources such as air flow, acoustic noise, and etc. This is because by isolating stacker setup from all external noise sources (air flow, and etc.) this huge noise is no longer existing in the stacking system even without improving the oscillator phase noise.

As one can see in Fig 4.7 c), SHG experiences much more noise with longer-length cavity compared to the short one and this makes stabilization quite challenging. As one can verify from the figure 4.7 c), the lowest phase noise for the short cavity was about 5mrad which was sufficiently small to stabilize the cavity. However, for the 9-times longer cavity, the lowest phase noise measured at around 800Hz was 50 mrad an order of magnitude large that of the short GTI. This is coinciding with the magnification effect of phase mismatch that was previously described. Although these minimum points on the phase noise characteristics curve is the best potential for stabilizing the stacker system however the main important noise level which should be reduced by order of magnitude is where there is no averaging taken (m=1). This is of particular interest for high energy experiments operating at kHz repetition rate where averaging would change the effective repetition rate.

Another important point to be mentioned is that stabilizing the GTI cavity with $T_{cav} = T_{osc}$ has been achieved in such a way that it is just limited to the Oscillator Amplitude Noise. In other words, since the GTI cavity round-trip time is equal to the round-trip time of the oscillator the stacking phase is not sufficiently sensitive to the oscillator phase noise, and therefore the stacking

phase noise is just a the same level as the amplitude noise of the oscillator. This is shown in the figure 4.8

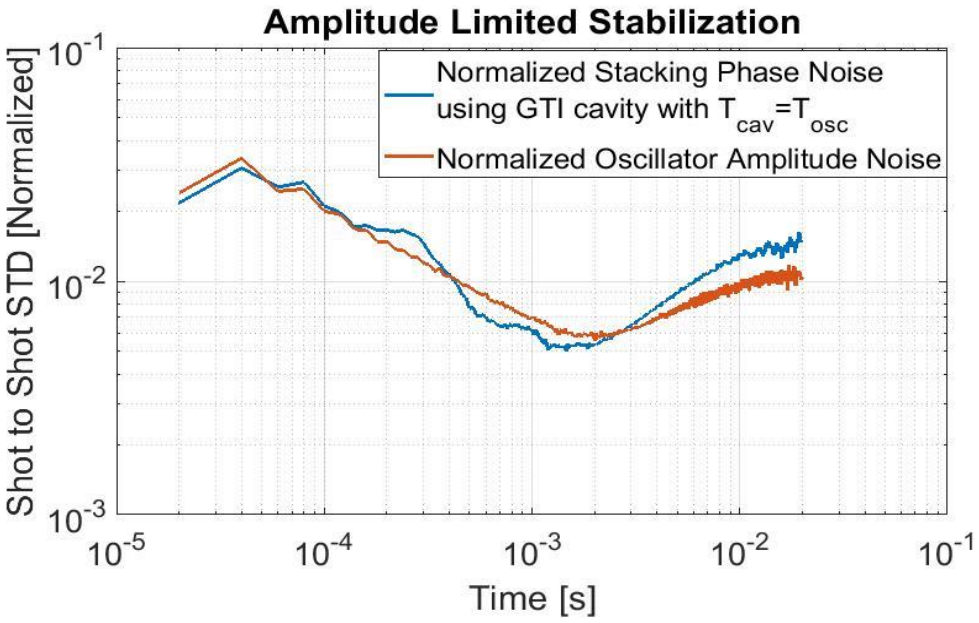

Figure 4.8: Normalized Allen Deviation Comparison between the Short GTI Cavity Stacking Phase and the Amplitude Noise of the mode-locked Oscillator

In order to significantly reduce the stacking phase noise, it was required to look for physical origins of the phase noise in mode-locked oscillators. In the past, researches have been done both theoretically and experimentally on analysis of physical origins in mode-locked oscillators (e.g quantum noise sources, pump noises, oscillator cavity length fluctuations, temperature variations, variations in the gain medium, and etc.). however, majority of these works are strictly case dependent and for different oscillators and electronics system the results are quite different.

Here we experimentally proved that reducing the noise in the pump significantly reduces the mode-locked oscillator phase noise and hence the stacking phase noise. This includes making

the optical setup for the pump more stable and fixing arrangement of the components as well as accurate selection of the driver for the laser diode which will be further explained in the chapter.

In figure 4.9 we present some of the experimental results of the effect of improving oscillator pump noise on the noise observed at the output metric SHG signal. We first show the effect of different drivers on the absolute amplitude noise of the laser diode. And second, the improvement of the noise observed in the SHG signal after cleaning up the pump will be presented.

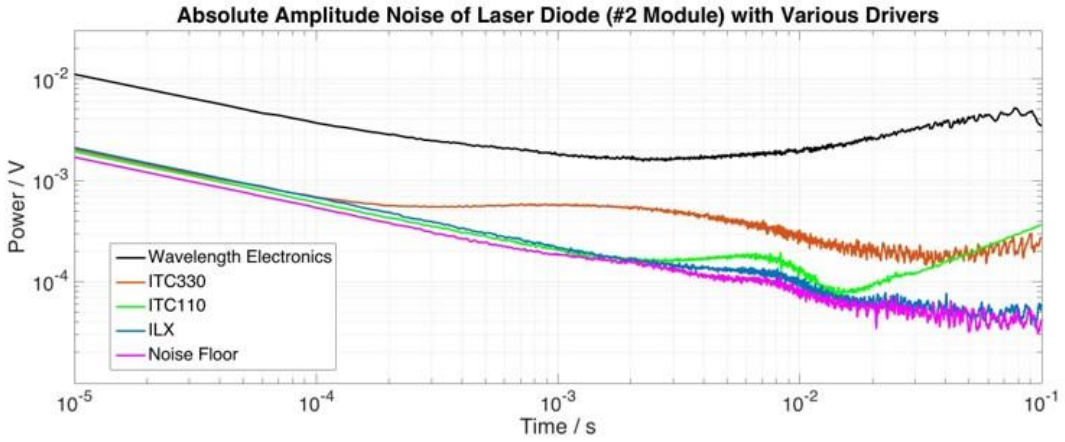

Figure 4.9: Absolute Amplitude Noise of the Laser Diode with Various Drivers

According to our measurement the Wavelength Electronics Driver exhibit the highest noise in the laser diode whereas the ILX performs the best among the others.

By using the low-noise mode-locked oscillator setup, we carried out the noise measuremts for measuring the phase noise one more time and here are the comparison results.

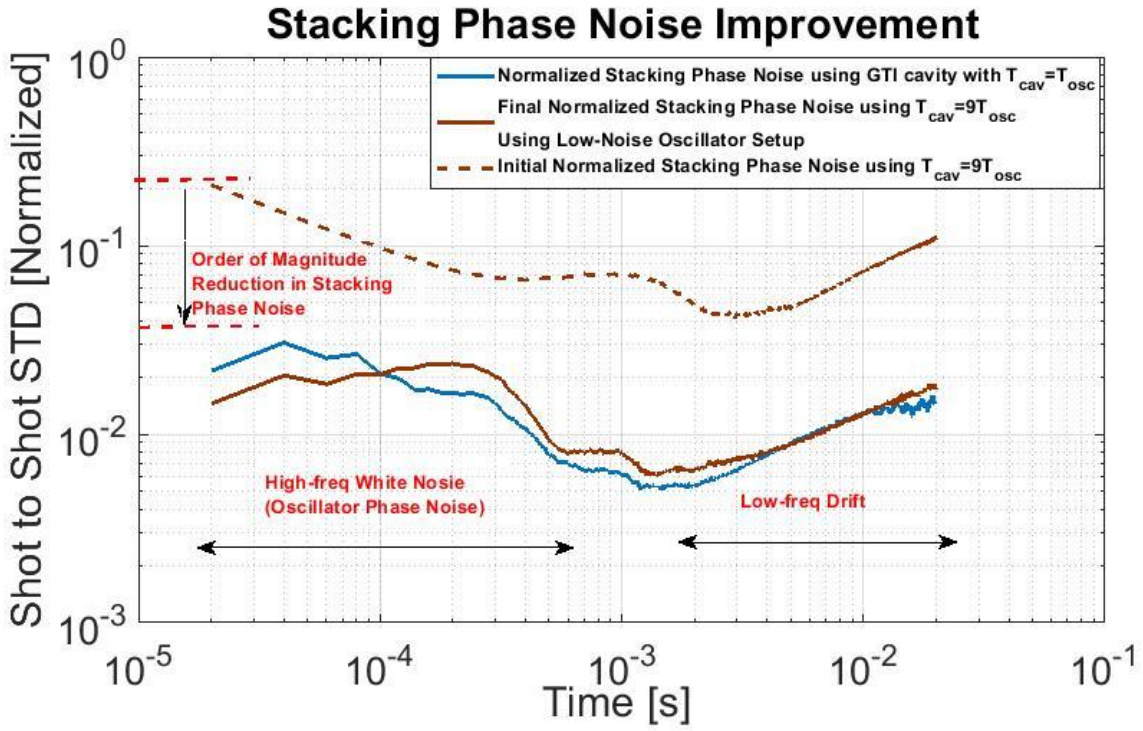

Figure 4.10: Significant Improvement of the Stacking Phase Noise by noise reduction on the pumping side. Curves are the Allen Deviation Characteristics of the stacking phase noise using different-length GTI cavities before and after Noise improvement

The figure 4.10 is the normalized Allen deviation of the SHG signal measured at 50kHz speed. As shown above, after cleaning up the pump the noise on the SHG in the high frequency band (>10KHz) has been reduced by order of magnitude in such a way that the stacking phase noise using the equal-length cavity, stacking phase using the 9-time longer cavity, and the amplitude noise from the laser all experience the same noise level.

In conclusion, we have successfully characterized the phase noise in our 1GHz mode-locked oscillator and improved the stacking phase to the laser amplitude noise.

4.4 Stacker Phase Space and Phase Drift Characteristics, and their effect on stacking stability

Since the stacking stabilization is achieved via a peak-detection technique, it is worth understanding the variation of the metric signal versus different phase values in the stacker phase space. Here we present a 2-Cascade GTI cavity scenario and a the simulated SHG signal versus $\phi 1$ and $\phi 2$ as the cavity phases has been plotted here. The parameters we chose for the following simulation are $R_1(\text{front mirror reflectivity of the } 1^{\text{st}} \text{ cavity}) = 0.66$, and $R_2(\text{front mirror reflectivity of the } 2^{\text{nd}} \text{ cavity}) = 0.34$

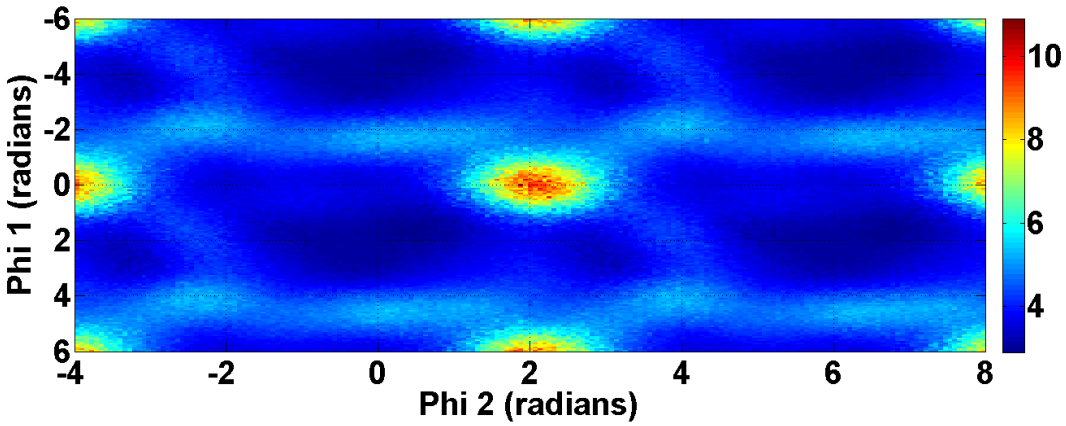

Figure 4.11: A two-dimensional cavity phase landscape where the colors represents the strength of the peak-power metric (TPA or SHG). The simulated landscape covers a 4π×4π phase space for a 2 Cascaded GTI stacking case

The landscape shown in figure 4.11 consists of a main large global maximum in the center which is repeatedly shown up for $\{\phi_1, \phi_2\} \pm 2n\pi$. The concept of the gradient path towards the global maximum is also clearly observed in the simple case of 2 cascaded cavities. For certain conditions depending on the reflectivities of the front mirrors in the GTI cavities, the SHG might experiences other semi-global maximums too. This happens primarily if there are almost close reflectivities. It can be theoretically proved that 2 cavity phases can be swapped upon the condition

if their mirror reflectivities are exactly the same and stacking would not differ. Sensitivity of the stacking to the errors on the reflectivity of the mirrors has been analyzed in [22]. Another feature of the metric landscape versus as a function of the cavity phases is that for larger number of cavities, many local maxima appear around the desired global one, thus the SHG metric function is not considered as a concave function.

For the case of multi-dimensional phase space (e.g. N=4) an N-dimensional parameter space should be still considered for determining local and global maximums. However, the phase landscape is different where many of the maximums around the global are as large as the main-global one. The important point is that even if any of these close-to-global maximums for equal-length GTI cavities are selected during stabilization process, they can still move towards the main-global maximum by applying the optimization algorithm. The rest of the peaks in the landscape are small compared to the main global one.

In order to eliminate the local maximums, initial cavity phase values need to be in the vicinity of the global maximum the local stabilization algorithm such as SPGD runs. If these cavity phase values are not near the global maximum, then the local optimization algorithm will fail to converge to the global maximum.

In order to do this, a Lissajous Scan has been chosen to run before the actual SPGD-based stabilization algorithm. Lissajous has specifically chosen against other scanning methods such as raster scan since the applied voltages on the PZT needs to have smoothly transition from the end of one phase cycle to the next one.

4.5 Stacker Stabilization Algorithm and its implementation

In this section we report the details of the control algorithm we utilized to demonstrate the stable stacking and its implementation as well. In this system we take the PZT voltages as our control parameters and simultaneously apply small random perturbations to all the control parameters, and then evaluates the gradient variation of system performance metric (J). The control signals update in iteration process of SPGD algorithm as following rule.

$$\phi^i = \{\phi_1, \phi_2, \dots, \phi_N\} \tag{4.6}$$

$$\rho^i = \rho_0 * \{\pm 1, \pm 1, \dots, \pm 1\} \tag{4.7}$$

$$\epsilon^i = J\left(\phi^i + \rho^i\right) - J(\phi^i) \tag{4.8}$$

$$\phi^{i+1} = \phi^i + \mu\epsilon^i\rho^i \tag{4.9}$$

Where i is the iteration number, ϕ_k is the round-trip cavity phase corresponding to the k^{th}cavity, μ is the gain coefficient which is positive for maximizing the metric, ρ denotes small random perturbations that have identical amplitudes and +/- sign (if the random generated phase is bigger than 0.5, then the sign is positive, otherwise the sign will be negative), $\epsilon^i$is the variation of system performance metric at the i^{th}iteration. (in our case the metric is the second harmonic generation signal which means J=SHG). Each time this error signal is evaluated, the direction in which the cavity moves is determined based on the sign of ϵ^i. In essence this algorithm performs a global-maximum search in the N-dimensional cavity-phase space.

In essence this algorithm performs a global-maximum search in the N-dimensional cavity-phase space. One complication, however, is that this N-dimensional "landscape" becomes very complex further away from this global maximum, consisting of multiple local maxima and minima, which would derail the SPGD search. To avoid this, a rapid Lissajous scan over the full N-phase space is performed first, identifying the approximate location of the global maximum,

and then “releasing” the SPGD algorithm in its relative vicinity. Since a sparse scan is sufficient, typical scan times are very short. For example, for the 4-cavity system demonstrated here it is less than 5 seconds. Figure 4.12 illustrates the details of the control implementation including the SPGD and the local search part.

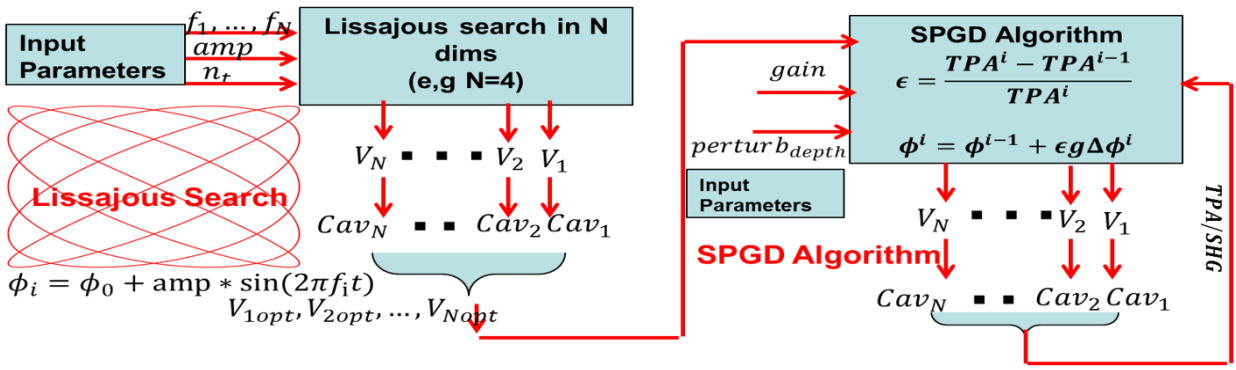

Figure 4.12: Algorithmic description of the Lissajous Local Search followed by the SPGD-based Algorithm for stabilizing the stacked pulse.

Here we simulate the performance of the SPGD algorithm for an equal-length 4-GTI stacker Cascade where the number of input pulses were chosen to be 10. The stacker parameters for the following simulation are as follows:

Front-Mirror Reflectivities: $R1 = 0.55, R2 = 0.52, R3 = 0.63, R4 = 0.63$

Figure 4.13 shows the simulation result for a 4-cascaded GTI stacker configuration where the metric signal (SHG) gets maximized and stabilized after a few iterations.

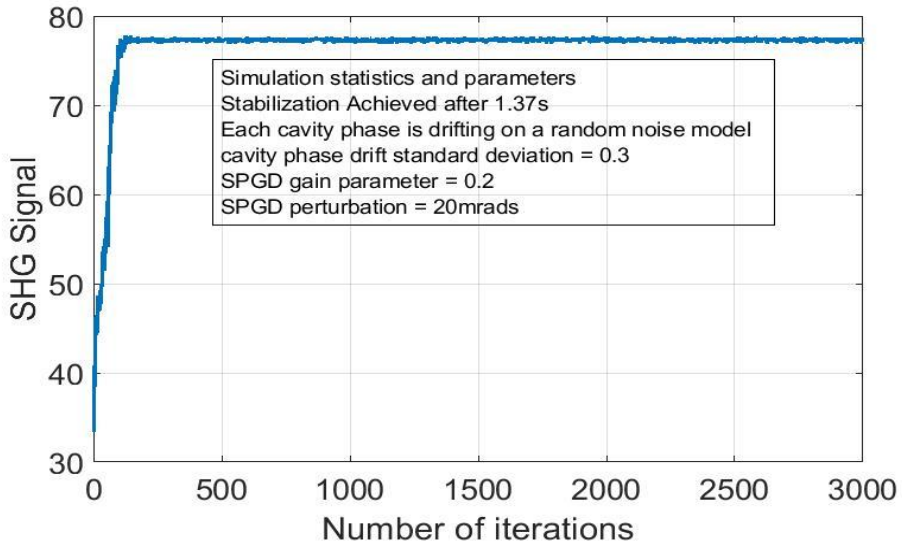

Figure 4.13: Simulation results showing the maximized and stabilized SHG signal associated with 4-cascaded GTI Stacking Stabilization

4.6 Stabilization Results for an Equal-Length 4-GTI Stacker Cascade

In this section we present the stabilization results for the first experimental set-up introduced in section 4.1 which is a 4-cascaded equal length GTI stacker scenario. SPGD algorithm software implemented in a PC runs at 200Hz loop frequency. The algorithm has been written on python and the software was talking to the fixed National Instrument analog hardware through USB. The gain coefficient μ and the perturbation amplitude ρ Is chosen to be 85 and 25mrad respectively but are adjustable in a wide range. 4-cavity locking is reproducibly achieved with <5secs convergence time after turning the stabilization key on. Fig.4.14 shows the stabilized SHG signal over 15mins with σ = 3% of the averaged SHG signal, corresponding to σ = 1.5% of the stacked pulse peak power. Insert in the figure shows the corresponding stacked pulse trace. Robust system operation was tested and verified for up to an hour of continuous running time, currently limited only by the continuous observation duration. This demonstration validates an effective control method for robust stabilization of a scalable number of CPS cavities.

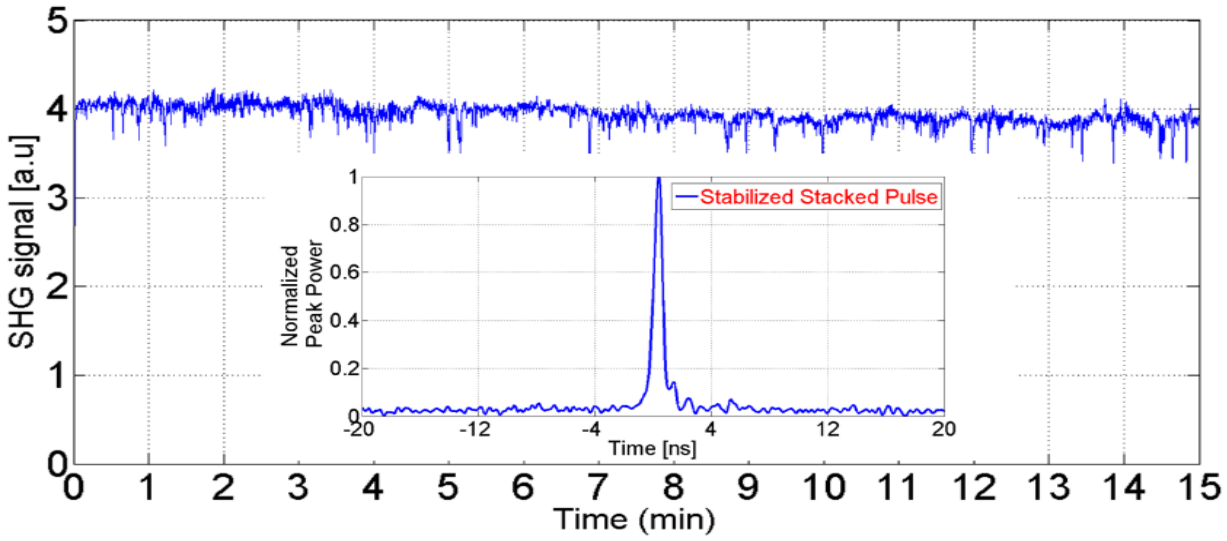

Figure 4.14: Experimental results of 4 Cascaded 1ns-GTI cavities, time domain drift of the maximized metric, and stabilized stacked pulse

4.7 Stabilization Results for a Multiplexed-Length 4+4 GTI Stacker Configuration

In this section we present the stabilization results for the second experimental set-up introduced in section 4.1 which is a 4+4 Multiplexed with non-equal length GTI stackers scenario. In the figure 4.15 we show the way we have closed the feedback loop using the FPGA system developed and explained in chapter 2.

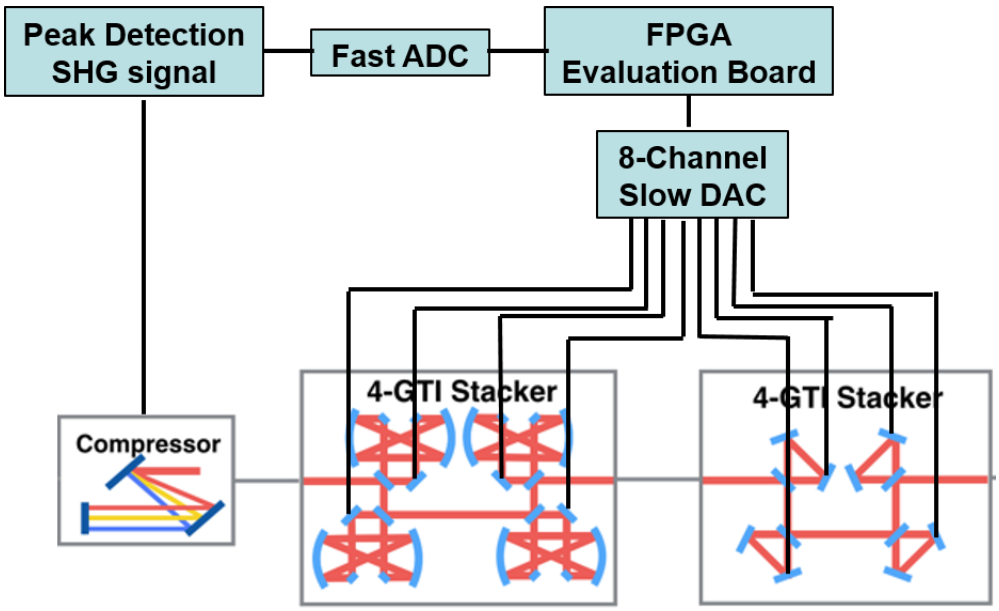

Figure 4.15: Block-diagram of the FPGA Control System along with the Stacker arrangement for 4+4 Multiplexed Stabilization Experiment

Figure 4.16 we present simulation results for a 4+4 multiplexed scenario where the front mirror reflectivities and cavity phase are chosen as follows:

R_1	0.58	R_5	0.58	$\phi 1$	4.66	$\phi 5$	4.66
R_2	0.58	R_6	0.58	$\phi 2$	3.15	$\phi 6$	3.15
R_3	0.69	R_7	0.69	$\phi 3$	5.46	$\phi 7$	5.46
R_4	0.69	R_8	0.69	$\phi 4$	0	$\phi 8$	0

Table 1: Cavity phase and mirror reflectivities for a 4+4 multiplexed stacking configuration

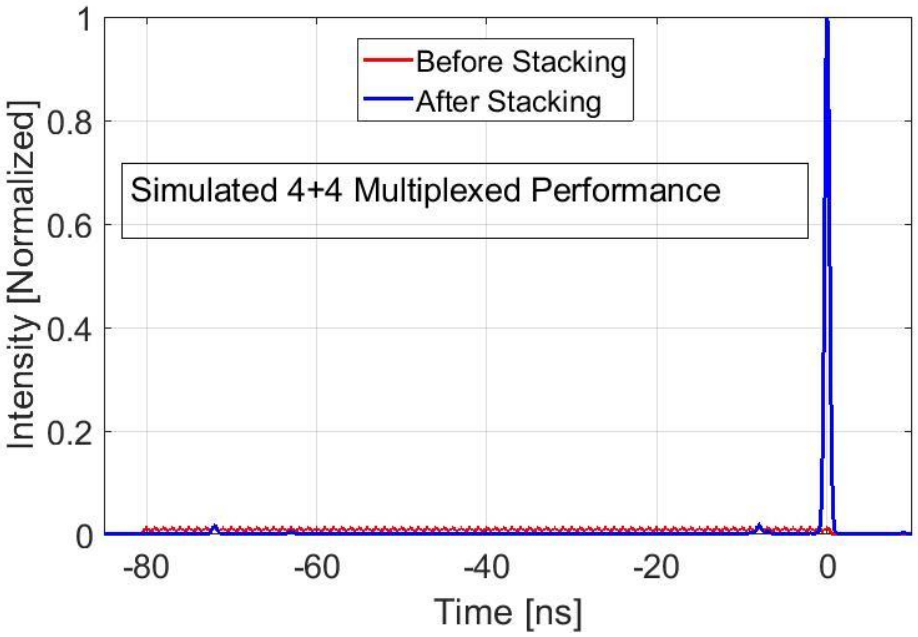

Figure 4.16: Simulation results for 4+4 Multiplexed Stacker System, Normalized Output Stacking Intensity Profile before and after stacking achieved.

Figure 4.17 shows the experimental results for a 4+4 multiplexed configuration with 81 pulse at kHz repetition rate.

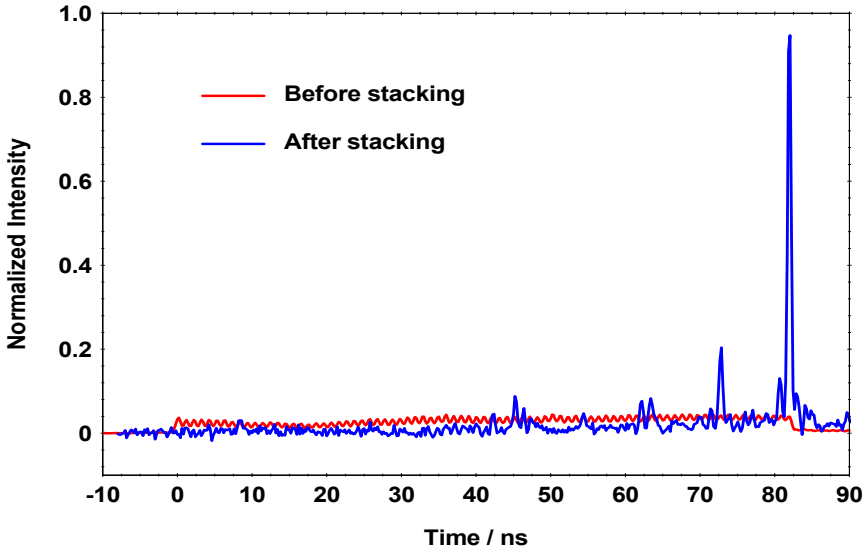

Figure 4.17: Experimental results for 4+4 Multiplexed Stacker System, Normalized Output Stacking Intensity Profile before and after stacking achieved.

These results show quite good qualitative agreement between the simulated experimental conditions and the experimental results. Here the stacked pulse (the 81th pulse) got stabilized with 2% standard deviation. There is the place to further improve the stabilization beyond the 2% standard deviation by either adapting the parameters of the SPGD algorithm or operating at the optimum loop frequency/speed. The largest pre-pulse happens to be at about the 72th pulse that limits the pre-pulse contrast. A pre-pulse contrast of 7dB was measured which is limited by the non-optimized burst pulse amplitude and phase which will be controlled further in feedback control outer-loop explained in chapter 5.

Chapter 5 Optimization of the Stacked Pulse Fidelity

5.1 Background

One of the important and desired characteristics of the stacked pulses is associated with a high degree of pre-pulse contrast which is required by many applications such as laser-plasma acceleration applications, and other laser-matter interaction-based applications. This is along with the main goal which is extracting nearly complete stored energy in the fiber amplifier. This chapter discusses about the algorithms developed and implemented to optimize the input burst profile and hence optimize the stacking performance in CPSA experiment. Technical goals that are targeted to be achieved are high pre-pulse contrast (>40 dB) and simultaneously good stacking efficiency. Stacking efficiency is different from pre-pulse contrast in the sense that one can achieve good stacking efficiency of, for example, 95% to >99%), while the residual few percent of the energy could significantly degrade pre-pulse contrast, if they would happen to be deposited in front of the stacked pulse. These two quantities are defined as follows:

Stacking efficiency η: power contained in the main stacked pulse compared to the energy power in the rest of the pulses: $\eta = \frac{I_{stacked}}{I_{tot}}$.

Pre-pulse contrast: χ: (power contained in the main stacked pulse compared to the maximum power contained in the pre-pulses. $\chi = \frac{I}{\max(I_{pre-pulse})}$.

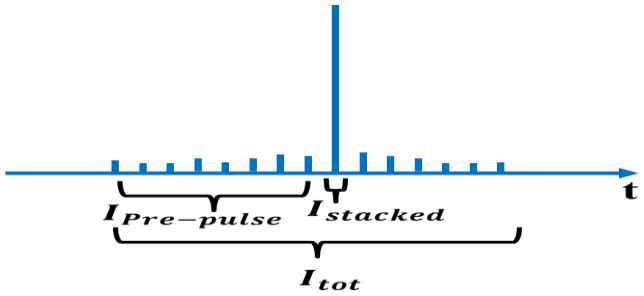

Figure 5.1: representation of power contained in the pulses of the stacked profile

There are many degrees of freedom of in the CPSA which enables one to better improve the stacking performance by real-time optimization of number of parameters. This is an advantage that a number of parameters in the system can be perturbed and optimized to maximize the objective function. The design of the stacking-burst profile in terms of pulse amplitudes and phases, and their practical realization in the stacking system cannot be known with absolute accuracy.

Since the front-mirror reflection coefficients of each GTI cavity cannot be defined with the accuracy of better than approximately 1%, it is sufficient to put uncertainty in determining the optimal values of input pulse amplitudes and phases. Furthermore, even if this recipe would be known precisely, it is nearly impossible in practice to imprint it with an absolute accuracy using electro-optic modulators at the front of the system, since there always is a certain degree of inaccuracy in knowing the exact amplitude and phase response of each of the modulators, expressed for example as inaccuracy in knowing the V_π voltage of a modulator. Also, it is known that various linear and nonlinear effects in the fibers and components of the fiber amplifier chain

might also affect both the amplitudes and the phases of the stacking-burst pulses. It is certain that quantifying all these effects beforehand would be a very challenging, and perhaps even a hopeless task.

Therefore, one of the critical tasks carried out and will presented in this chapter is to develop a computer-based optimization system, which would optimize the stacking-burst amplitude and phase profiles in real time, based on the measured fidelity of the stacked pulse at the system output.

Before discussing the details of how we developed, and implemented our optimization algorithm, similar to what was presented in chapter 2, a general viewpoint and discussion on the concept and definition of optimization followed by a survey of some optimization algorithms is presented. At the end, we decided to choose Stochastic Parallel Gradient Descent (SPGD) algorithm for optimization aspects of the system since it is a hill-climbing algorithm that can be used in any optimization problem where you have an approximately good starting point sufficiently close to the optimal point in your objective function. Moreover, it is compatible with the peak power detection scheme of the system in the sense of maximization which is targeted in the experiment. And finally, for comparison purposes, a genetic algorithm (GA) was developed, and implemented to compare its performance with that of SPGD.

5.2 Concept and Definition of Optimization

Concept of stabilization in control theory was disused and defined in the previous section. In this section we discuss the concept of optimization in control theory and concretely define what optimization is. Optimization is a process of finding precise values of certain system parameters

to either maximize or minimize one or more metric functions. A mathematical representation for optimization problem is as follows:

$$given: \begin{Bmatrix} f_i(x_1, \dots, x_n), one\ or\ more\ metric\ functions \\ x_1, \dots, x_n\ system\ parameters \end{Bmatrix}$$

$$Optimization\ problem: finding\ precise\ required\ values\ (X_1, \dots, X_N) such\ that\ f_i(X_1, \dots, X_N) \geq f_i(x_1, \dots, x_n)\ for\ all\ (x_1, \dots, x_n)$$ [for the case of maximization]

Optimization is widely used in variety of mathematical and control problems. The metric function f_i can be a cost function, an error function, a dissipation function for the case of minimization. On the other hand, f_i can be a power function, or energy function for the case of maximization. As an example, for coherent combining of fiber amplifiers where pulses are first split into a number of channels and then recombined after the amplification, output peak power can be considered as a metric function. After stabilizing path lengths for different fiber channels, still there exist some parameters in the system such as the polarization state of the combined beam that need to be precisely set to achieve maximized peak power and hence optimize the performance [67]. Another example would be coherent pulse stacking system where an optimization algorithm tries to find precise system parameters such as pulse phases and amplitudes to maximize peak power or pre-pulse contrast as two different metric functions, and as a result, optimize the system performance.

In the following section, a general survey of existing optimization algorithms is presented where they can be used to optimize the performance of coherent combining systems by maximizing particular metric functions.

5.2.1 Survey of Optimization algorithms

1) SPGD

Detailed discussion on the theory of stochastic parallel gradient descent algorithm (SPGD) was presented in chapter 2.

2) Genetic Algorithm (GA)

Genetic algorithm is essentially an optimization model based on the concept of evolution [45,46]. This algorithm simulates an optimization problem as a specific structure similar to the structure of chromosomes and tries to optimize the target function by finding the best chromosome or genes in the structure [47]. This approach is utilized in variety of applications and the way it is implemented is pretty much problem specific.

In order to implement this algorithm, a population consist of a number of genes is selected. Then the process of selecting the best genes for production begins. The genes that make a better value for the goal/target function are assigned with higher probability to produce kids. This process is taken for many iteration until the desired value for the goal function is achieved. The general flow-diagram of genetic algorithm is shown in the following figure.

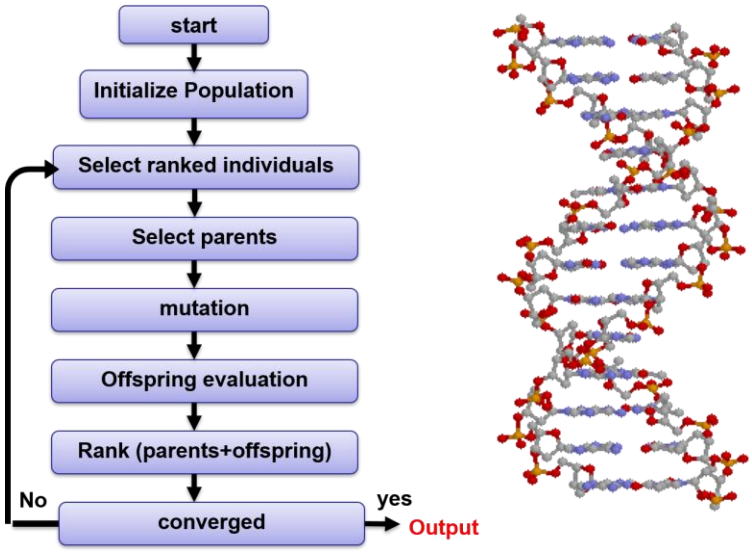

Figure 5.2: Flow-diagram of typical genetic algorithms for optimization purposes

3) Simulated Annealing (SA):

Simulated annealing is a probabilistic optimization technique used for approximating the global optimums of a complex large optimization problem. This technique is more suitable when approximating the global optimum is more important than accurately obtaining a local optimum in the large search landscape. This technique is based on the physical annealing process of a solid material where the solid's temperature is increased first up to sufficiently close to its melting point and then is released to naturally lowers its temperature and hence relieve the existing non-uniformities inside it [60,61,63]. In order to implement or simulate the algorithm a stochastic sampling method such as Metropolis-Hasting algorithm. [64] is used. This algorithm was initially utilized for simulating or modeling the equilibrium behavior of a group of atoms (in our case input pulse phases or amplitudes). In each iteration, a given atom (control element) receives certain amount of displacement as shown in equation (5.1) and the resulting system energy change $\Delta E(\equiv \Delta J)$is calculated. This applied displacement is accepted if the resulting energy change becomes negative ($\Delta E < 0$). However, if $\Delta E > 0$ the displacement is not rejected but is behaved with a probability distribution called probability acceptance as shown in equation (5.2) [61].

$$\Delta u^k = \{\Delta u_i^k\} \text{ perturbation (displacement vector)} \tag{5.1}$$

$$p^k = e^{-\frac{\Delta J^k}{T^k}} \text{acceptance probability} \tag{5.2}$$

4) Algorithm Of Pattern Extraction (Alopex)

Alopex is a cross-correlation based learning algorithm that was first used by Harth & Tzanakou, in 1974 for mapping receptive fields [65]. For any optimization algorithm, there are two important decisions that need to be made during iterations. In which direction the parameter space needs to be modified and the step size along the determined direction. Usually the step size can be chosen to be constant and the direction to move from the current point to the next point is determined based on the correlation between changes in the parameter space and the changes in the target function for certain number of iterations. This is the core feature of alopex. If the vector of control parameters is $u = (u_1, \dots, u_m)$, then the update in the parameter space is done according to the iterative relation [55]:

$$u^{k+1} = u^k + \eta \mathrm{x}^{\mathrm{k}} \ \ where \ \ x^k = (x_1, \dots, x_m)^k \ \& \ \mathrm{x_i^k} = \begin{cases} 1 \ with \ probability \ p_i^k \\ -1 \ with \ probability \ 1 - p_i^k \end{cases} \quad (5.3)$$

$$p_i^k = \frac{1}{(1+e^{-\frac{c_i^k}{T^k}})} \ where \ c_i^k = \Delta u_i^k \Delta J^k \ \& \ \Delta u_i^k = u_i^k - u_i^{k-1} = \eta x_i^{k-1} \quad (5.4)$$

In equations (5.3) and (5.4), T^k is a temperature parameter which is updated after a certain number of iterations. By looking at equations above, it is clear how the algorithm is based on the correlation between Δu_i^k and ΔJ^k to determine its direction to move from current point to the next point [55,56].

5.3 Implementation of SPGD-Based Algorithm for Optimizing the Burst

Before implementing the optimization control system, an optimized set of pulse amplitude and phase profiles which were obtained based on our theory of stacking have been input into our Electro-Optical Modulators (EOMs). These profiles were manually perturbed such that a perfect stacked pulse with sufficiently small pre-pulses in the stacked train is achieved. this illustrates that the designed amplitude and phase profile provides a solution sufficiently close to the optimal

stacking point. Taking this as an experimental evidence, an SPGD-based Optimization algorithm for optimizing the input burst profile is proposed.

The second fact is that our stacking optimization will be much slower than cavity phase stabilization which runs inside the nested control loop. For instance, executing 1000 loops for stabilizing cavity phases at kHz range, will make the optimization loop runs every second which is slow enough.

It is known that SPGD algorithm has a convergence time which is roughly proportional to the number of parameters you want to optimize in your problem and might reduce the convergence speed but for specific cases (e.g. 4 Cascaded GTI cavities with 18 parameters for amplitudes and phases in a 9-pulse configuration or 4+4 Multiplexed Case with 162 parameters in a 81-pulse configuration), convergence time in the order of minutes will be acceptable to us.

Also knowing that stacking optimization is not a stabilization problem we can turn the outer-loop control off and just continue the cavity stabilization once we get the optimized stacking parameters.

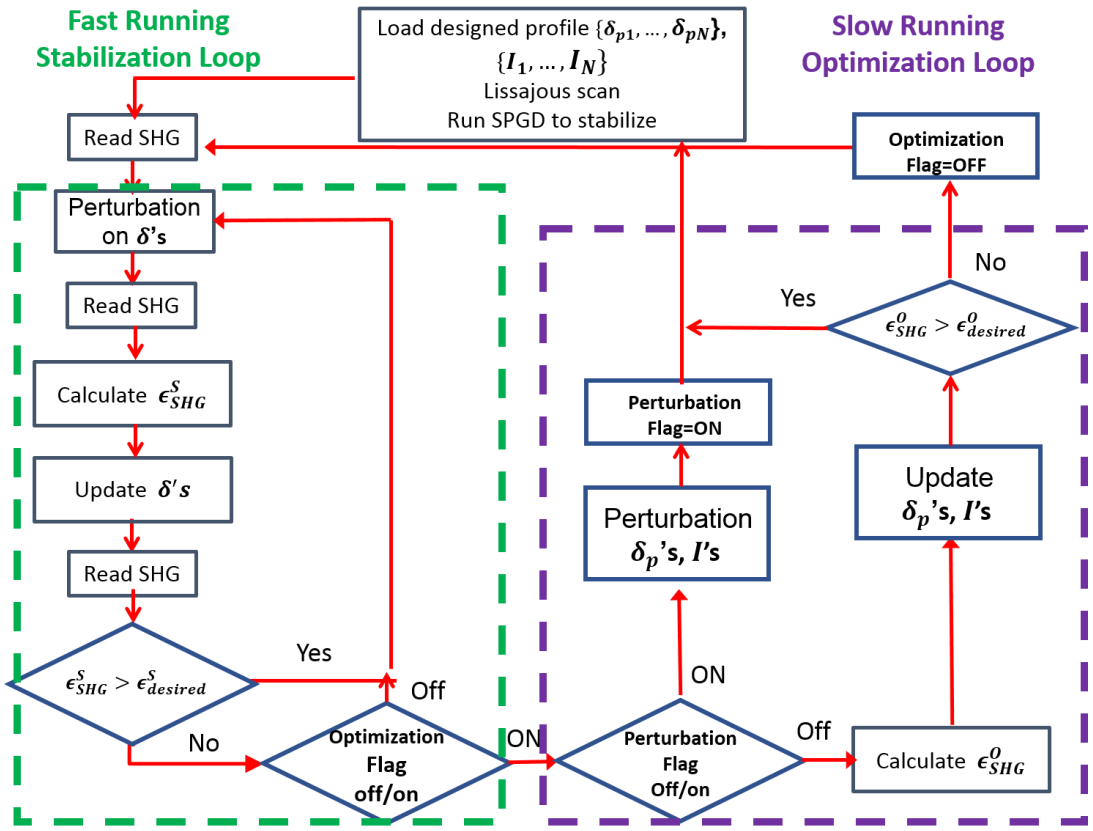

Figure 5.3: Block Diagram of the Control Algorithm for Stacker Stabilization and Pulse Profile Optimization

phase stabilization process. This is based on the assumption that there is not any slow-drifts in the system that can change the optimized parameter set.

For low-energy experiments where the saturation effects are not of that importance, the amplitude profile is not required to be real-time optimized, however for high-energy experiments the amplitude profile needs to be optimized too to compensate for any saturation effect. This optimization should be done along with the stabilization process since any perturbation on the amplitude or phase profile will completely changes the required stacker cavity phases for stabilization. Therefore, a nested-based control algorithm has been used where the optimization loop runs outside the stabilization feedback loop.

The algorithmic control program shown in figure 5.3 is implemented using the FPGA-based control system. Details of the implementations will be presented later on through the chapter. Cavity phases are denoted as δ, amplitudes of the input pulses are denoted as $\sqrt{I}$ (square root of pulse intensities), ϵ_{SHG}^{S} is the error signal for the stabilization loop which is calculated at each iteration for determining how to update cavity phases. ϵ_{SHG}^{O} is the error signal for the optimization loop for determining how to update the pulse amplitudes and phases. Two flags have been considered for the outer-loop which signals if perturbing the pulse parameters and executing the outer-loop is needed or not.

As shown in the block diagram above, initially the designed amplitude and phase profile for the input burst is loaded to the Electro-Optic-Modulators (Phase and Amplitude EOMs) then the control system tries to stabilize the stackers for this initially loaded input waveforms by running an initial local-search (Lissajous) in N dimensional cavity phase space, finding a point which is sufficiently close to the main-global maximum, and releasing the SPGD-based algorithm to stabilize.

After this initial step, the program enters the normal stabilization loop. This loop consists of 5 stages namely perturbing stacker cavity phases, measuring the metric signal, calculating the corresponding error signal (~ relative difference between the two measured SHG between two consecutive iterations) updating cavity phases depending on the value calculated for the error signal, and finally re-measuring the metric signal. The iteration update rate or equivalently loop speed is controllable and can be increased to about 4KHz (limited by the data communication

depending on the operational frequency or interest). One important point about this loop is that it keeps running even if the optimization loop is turned off.

The optimization loop which acts as an outer-loop with respect to the stabilization loop. The important point in this loop is that for each iteration either perturbing the pulse phases/amplitudes or updating them is immediately followed by the stabilization process as it was explained before. The updated amplitude and phase profile need to be loaded between the pulses to avoid damaging the amplifiers in the system. In order to achieve this, specific firmware for the FPGA has been developed that swaps two waveforms between the pulses and outputs the new one to the 1GHz digital to analog converter. Details of the firmware development for this will be explained throughout the chapter.

5.4 Experimental Setup

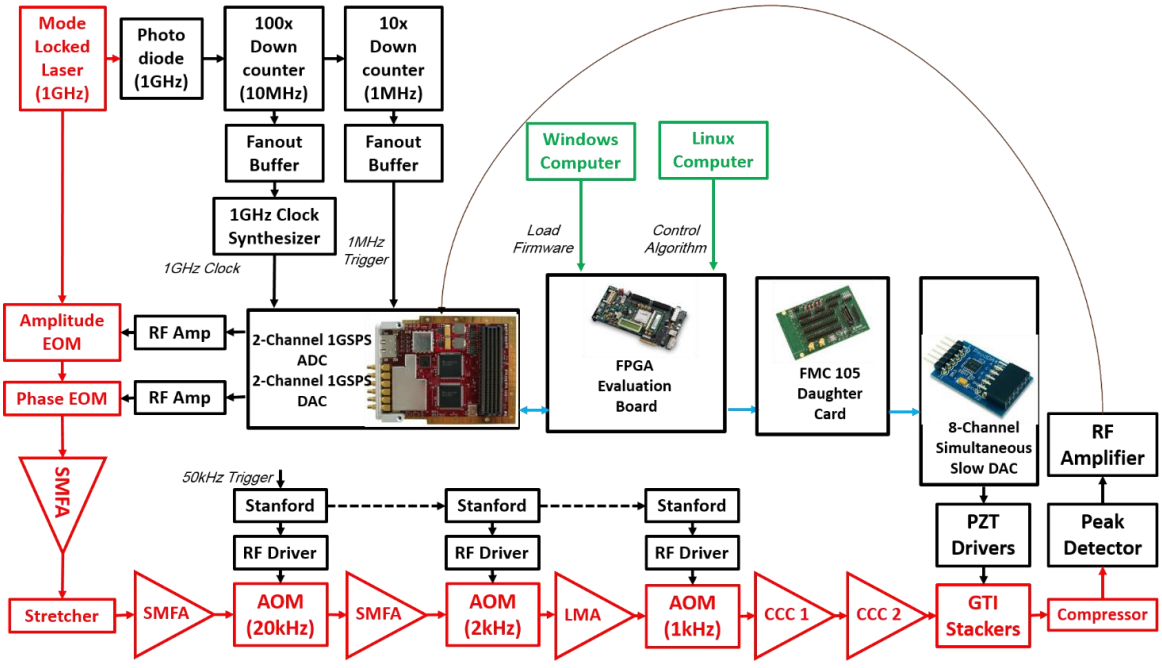

Figure 5.4: Experimental Setup for improving stacking fidelity

As shown in figure 5.4, a 1GHz clock signal from the mode-locked oscillator is used to sample out the SHG data acquired by the 1GSPS ADC. This readout data is used for calculating how much improvement has been achieved in the peak-power signal during stabilization and optimization process. Each peak of the metric signal is read every 20us ($\frac{1}{f_{rep}} = \frac{1}{50KHz} = 20us$). This requires a 50KHz trigger signal synchronized with the mode-locked Oscillator.

The 1GSPS DAC with maximum 500MHz analog bandwidth in this system is the key part for optimizing the burst amplitudes and phases. We have programmed the DAC such that maximum 500MHz analog Bandwidth is obtained and get a time resolution of 1ns in +/- for receives a 1MHz trigger signal to load the updated amplitude and phase waveforms onto the RF amplifier first to boost the output power up to more than 2V before being loaded onto the EOMs.

As explained, the 1GSPS DAC and ADC in the experimental system need to receive different trigger signal from the laser system. In order to efficiently provide this a firmware-based down-counter has been developed such that the incoming 1MHz trigger signal gets down-counted to 50KHz enabling the ADC successfully detects the SHG peaks every 20us. This is a pathway for rearranging the entire the trigger scheme in and trigger the rest of the control system using the FPGA system operating as the Master Trigger Source.

5.5 Implementation of Genetic Algorithm for Optimization Purposes

In this section a complete introductory description as well as implementation details of a genetic algorithm for optimization purposes in CPSA system is presented.

To explain the implementation, we consider optimizing the phase profile in the burst while the amplitude profile is fixed. However, similar model can be applied for the amplitude profile as well. For initialization or making the initial set of parents in the problem, a certain number of phase profiles is taken (e.g. N_{parent}=20). The way we implement the genetic-based optimization algorithm is that phase profiles can be either parents or children. The first parent is first initialized. This initial profile could be a profile that ends up in a point relatively-close to the global peak in the landscape of the target function or it can be a profile that makes the target function lays arbitrarily far from the global peak. We will later on show that the algorithm successfully optimizes the system so that the target function converges to the maximum almost independent of the initial condition. For instance, in the case of 4-cascaded GTI stacking with 9 pulses, the first parent is initialized as $P_1 = [\phi_1, \dots, \phi_{10}]$. In the next step, the (N_{parent}-1) remaining profiles (parents) are generated using the first (master) profile based on mutation. In order to do this, a random sequence of 0's and 1's are assigned for each individual phases within a profile which determines if that particular phase gets mutated or not (e.g $S = [0\ 0\ 1\ 0\ 1\ \dots .\ 0\ 1]$). This sequence is then dot-multiplied by a sequence of random phases generated based on the normal distribution of 0 average (e.g $R = normrnd(1{,}10)$) . For instance, for the case of N_{parent}=20 and N_{pulse}=10, the i^{th}profile P_i $(2 \leq i \leq 20)$ is generated as in equation (5.5):

$$P_i = P_1 + S_i .* R_i \tag{5.5}$$

This procedure is continued until all phase profiles or parents are initialized. Next, each of the N_{parent} parents should produce certain number of offspring which are phase profiles (e.g $N_{offspring} = 9$) similar to the procedure taken for making the parents in the previous step (see equation (5.6)). We denote the offspring as O_{ij} where i is the index of the parent from which the

offspring is reproduced, and j is index of the child (e.g O_{23} is the 3rd child from the 2nd parent).

$$O_{ij} = P_i + S_j .* R_j \tag{5.6}$$

an initial population consist of N_{parent} parents and $N_{parent} * N_{offspring}$ children is made to be input into the genetic algorithm. As a result, the total number of individual phase profiles in the population is ($N_{offspring}$. +1)*N_{parent}.

Next stage in the algorithm is the evaluation where each individual phase profile among the entire population of (N_{parent}+1)* $N_{offspring}$ elements is evaluated in terms of their corresponding system response or the target function value. In our case, the SHG signal value corresponding to each of those individual elements is calculated, sorted out, and the first N_{parent} highest SHG values and their corresponding phase profile is selected. These new N_{parent} profiles are denoted as new parents to reproduce new sets of children. This process is carried out for certain number of iterations such that a convergence is guaranteed. Here we present a complete flow diagram of the optimization algorithm for better grasp of concept (See Fig 5.5).

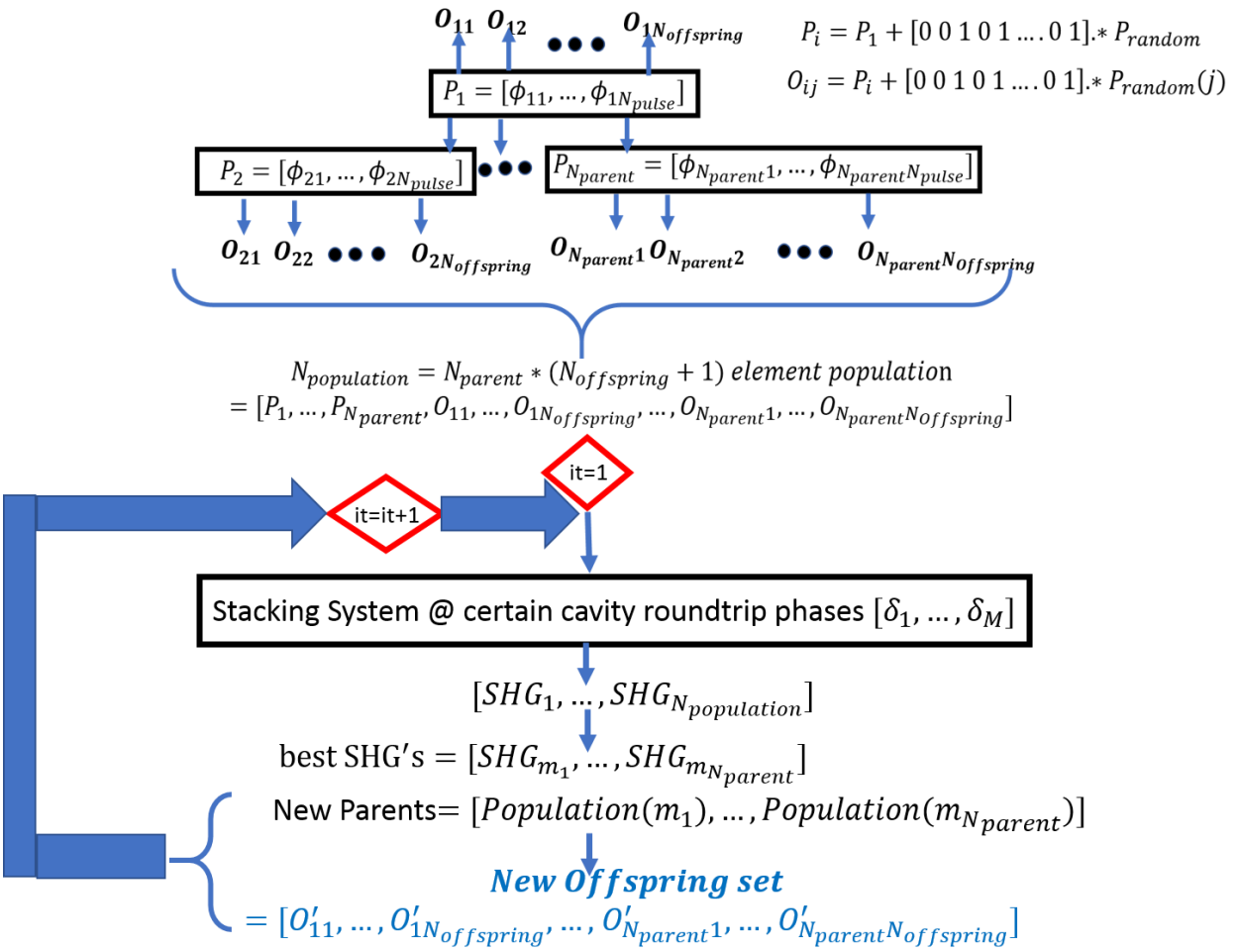

Figure 5.5: Flow-Diagram for the Genetic Algorithm

To evaluate the performance of the algorithm and to compare it with the SPGD algorithm, we performed a detailed numerical study for an equal-length 4-GTI stacker configuration, which can stack approximately 9 pulses. An ideal stacking at the output of a stacking arrangement would correspond to a single stacked pulse. The required amplitudes and phases for the incident stacking burst that would produce this single stacked pulse could be calculated by taking a time-reversed complex conjugate of the impulse response (i.e. stacker response to a single input pulse) for a chosen 4-GTI cascaded cavity design, determined by the set of front-mirror reflectivities and roundtrip phases given below. We simulate the effects of non-ideal conditions in the system by

adding random phases to each of the stacking burst pulses. Then we use this "non-ideal" stacking burst as an identical input to both SPGD and Genetic algorithms and calculate the performance of each algorithm of optimizing the input stacking burst phases. Multiple random realizations of these "distorted" input stacking profiles are used for multiple simulation runs to obtain the evaluation of the performance of each of the algorithms for a multitude of possible system conditions. By comparing the results of each algorithm in terms of the converged metric (SHG) and the final stacked profile (i.e. pre-pulse contrast) we can estimate how well each of the algorithms will be able to compensate these system-induced distortions.

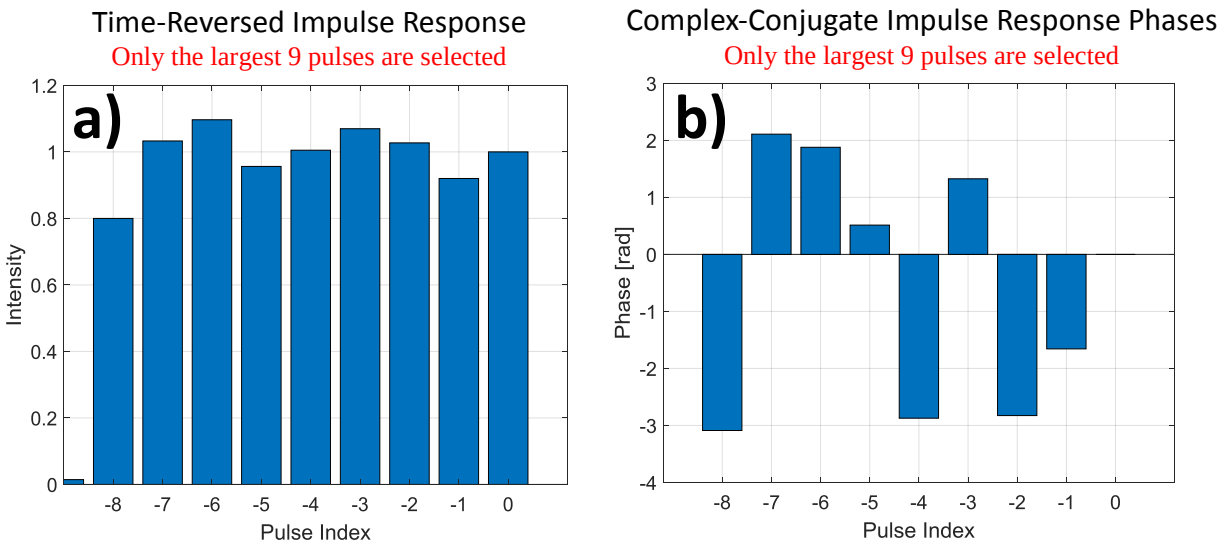

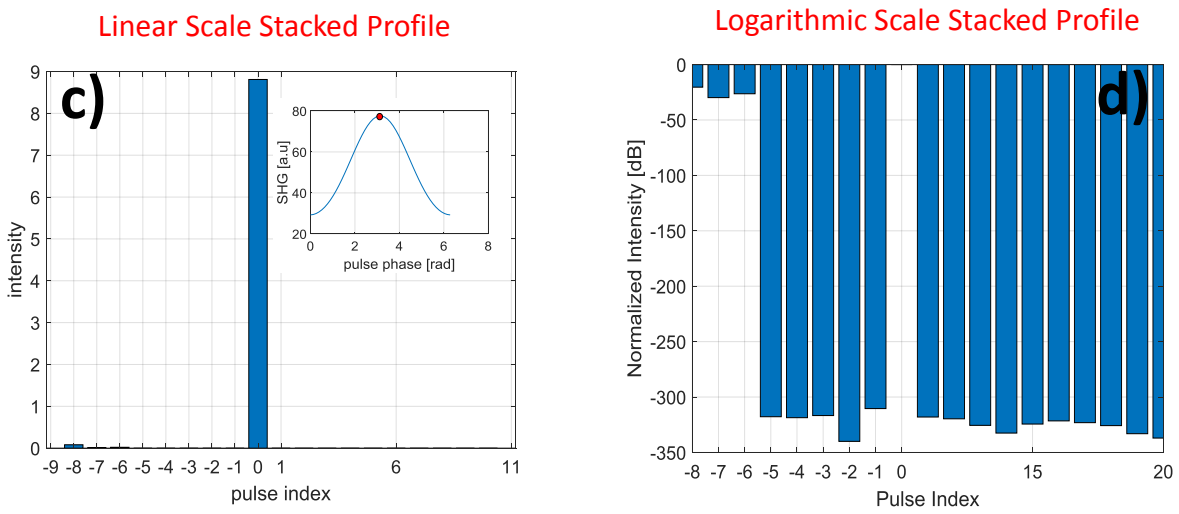

Figure 5.6: a) time-reversed impulse response as the input intensity profile with the largest 9 pulses b) Complex-conjugate phase of the impulse response as the input phase profile c) ideal stacked profile in linear scale d) ideal stacked profile in logarithmic scale

Parameters of the stacking system that has been used corresponding to the simulation results presented here are as follows: The reflectivities for the front mirror in the GTI cavities are: $R_1 = 0.55, R_2 = 0.52, R_3 = 0.63, R_4 = 0.63$. Cavity phases have been chosen to be as $\delta_1 = 4.66, \delta_2 = 3.15, \delta_3 = 5.46, \delta_4 = 0$.

An ideal single stacked pulse, i.e. pulse with no pre- and post-pulses, can only be achieved with an infinitely long incoming stacking burst [22]. In real experiment the incoming burst has to be truncated to a finite number of pulses. Therefore, in these simulations we truncate the infinitely-long input amplitude profiles to the largest 9 pulses of the time-reverse complex conjugate of the impulse response (as shown in figure 5.6a). However, this truncation produces the non-zero pre-pulse content, which is evident as the first three pulses at the positions "-8", "-7", and "-6" in the 5.6 c and d. It originates from the front-mirror reflections of the first pulses in the incoming stacking burst, which therefore cannot be reduced by controlling stacking burst phases. In actual experiment, these reflection-caused pre-pulses can be made arbitrarily small by increasing the

length of the truncated burst to a sufficient length to achieve the required level of the pre-pulse contrast [22]. To reduce the computation time, we chose to not increase the burst length, but to ignore the first three calculated pre-pulses in the subsequent analysis.

In this part, we present simulation results corresponding to completely random initial phase profiles where all the pulse phases are randomly deviated from the optimal "ideal" profile. Few examples of different phase profiles (see fig 5.7), their corresponding SHG values, as well as their resulting stacked profiles are presented here to get a better sense that the algorithm can respond to any arbitrary initial point and to converge to the optimum.

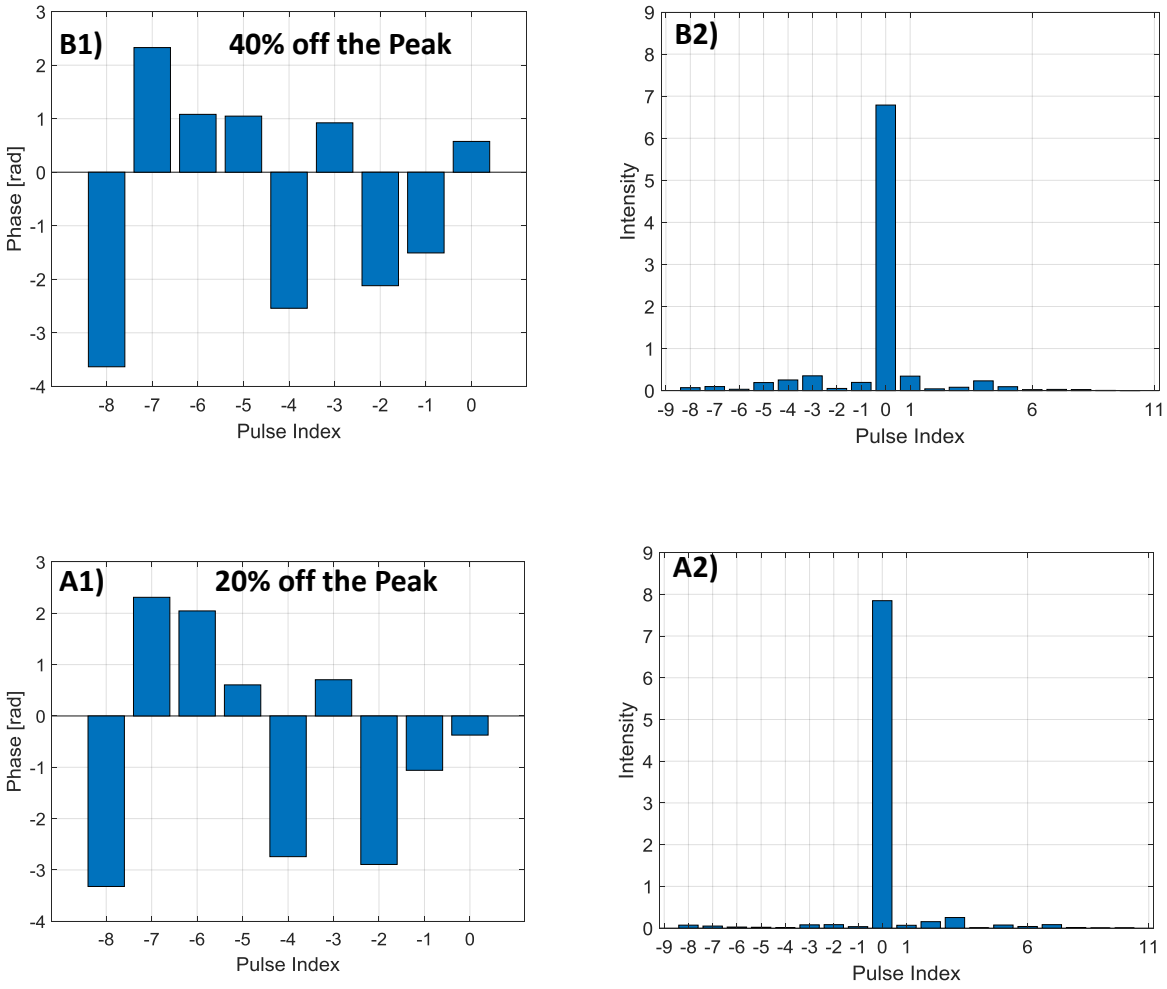

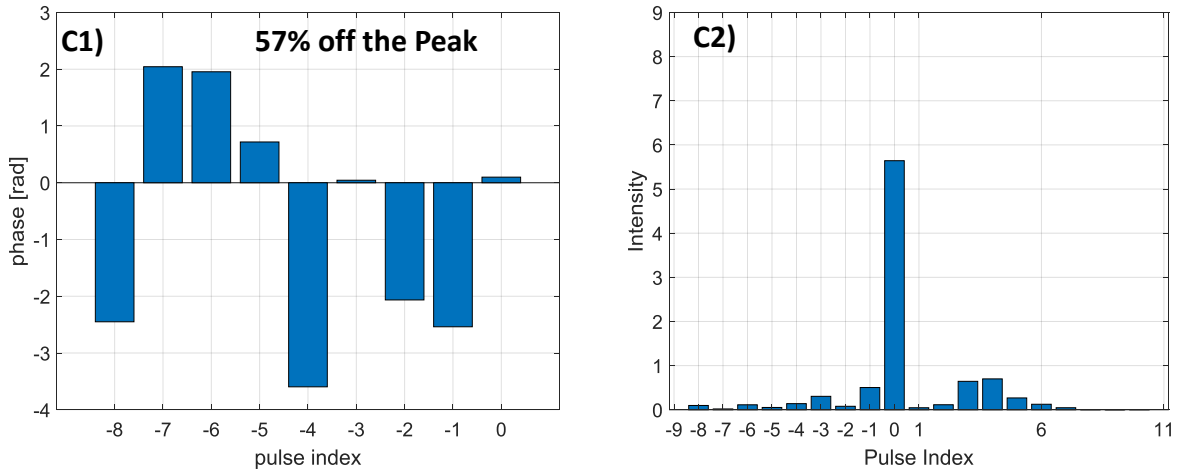

Figure 5.7: A1) and A2) are the perturbed phase profile resulting in an SHG 20% off the peak and the corresponding stacked profile respectively. B1) and B2) are the perturbed phase profile resulting in an SHG 40% off the peak and the corresponding stacked profile respectively, C1) and C2) are the perturbed phase profile resulting in an SHG 57% off the peak and the corresponding stacked profile respectively.

One point to be mentioned about the results in figure 5.7 is that in real experimental scenario the starting point is not expected to be significantly off the global peak (perhaps, by 10% - 20%). For evaluation purposes, and to make sure the designed algorithms are able to optimize arbitrary profiles, and hence the stacking performance, we examined as many cases as possible even as way off as about 60% of the global peak.

For the following simulations we examined 250 random phase profiles of the input stacking bursts, each defined as a normal distribution with a certain value of its standard deviation σ. This σ was kept the same for every five profiles, and then changed, thus giving overall 50 different σ values covering the range $0 < \sigma < 0.5$. Each distribution corresponds to a specific initial point on the SHG "landscape", i.e. SHG signal magnitude produced by each corresponding "initial" stacked profile which would occur without the optimization, as shown in Figure 5.8. As expected, SHG-signal magnitude decreases with increasing σ due to increasing stacking errors, and the SHG value spread also increases.

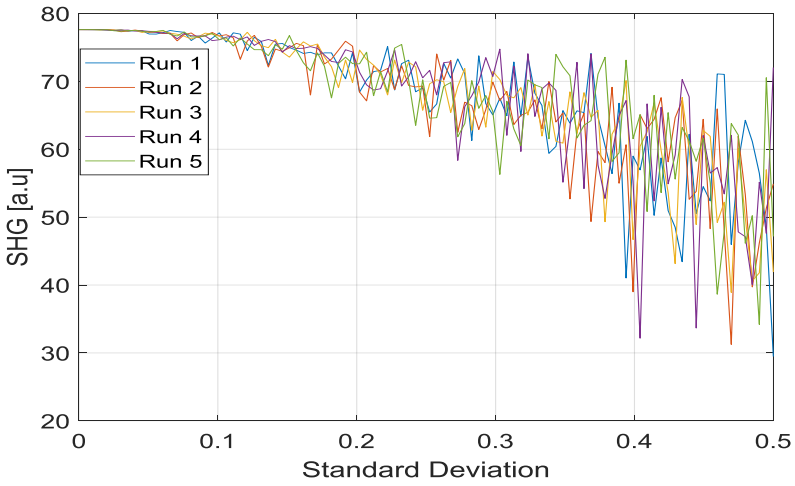

Figure 5.8: SHG changes with respect to the perturbations specified by the standard deviation of the normal distribution

Next, in figure 5.9(a) and (b) we show the optimization simulation results, comparing both algorithms. Only results of 50 "perturbations", each with a different σ value, are plotted here

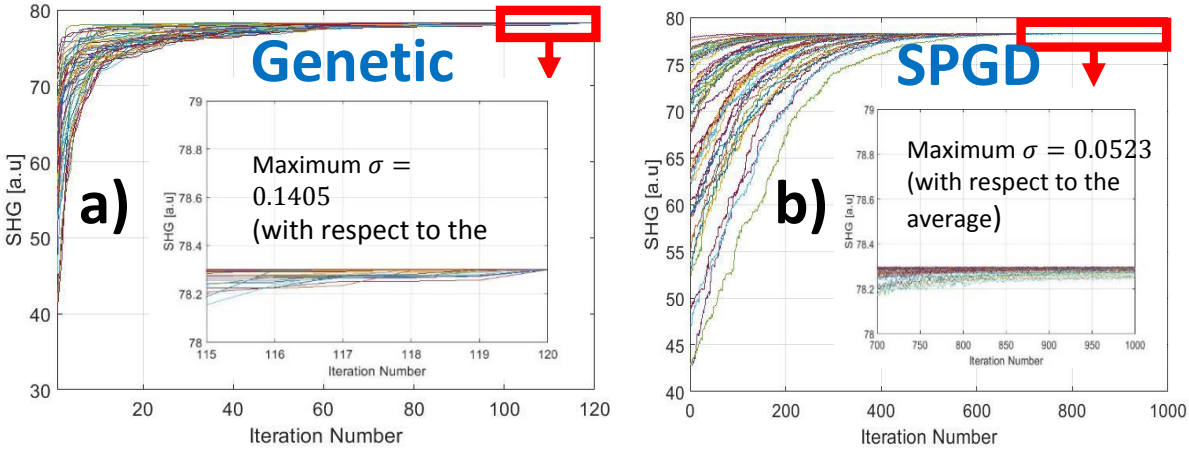

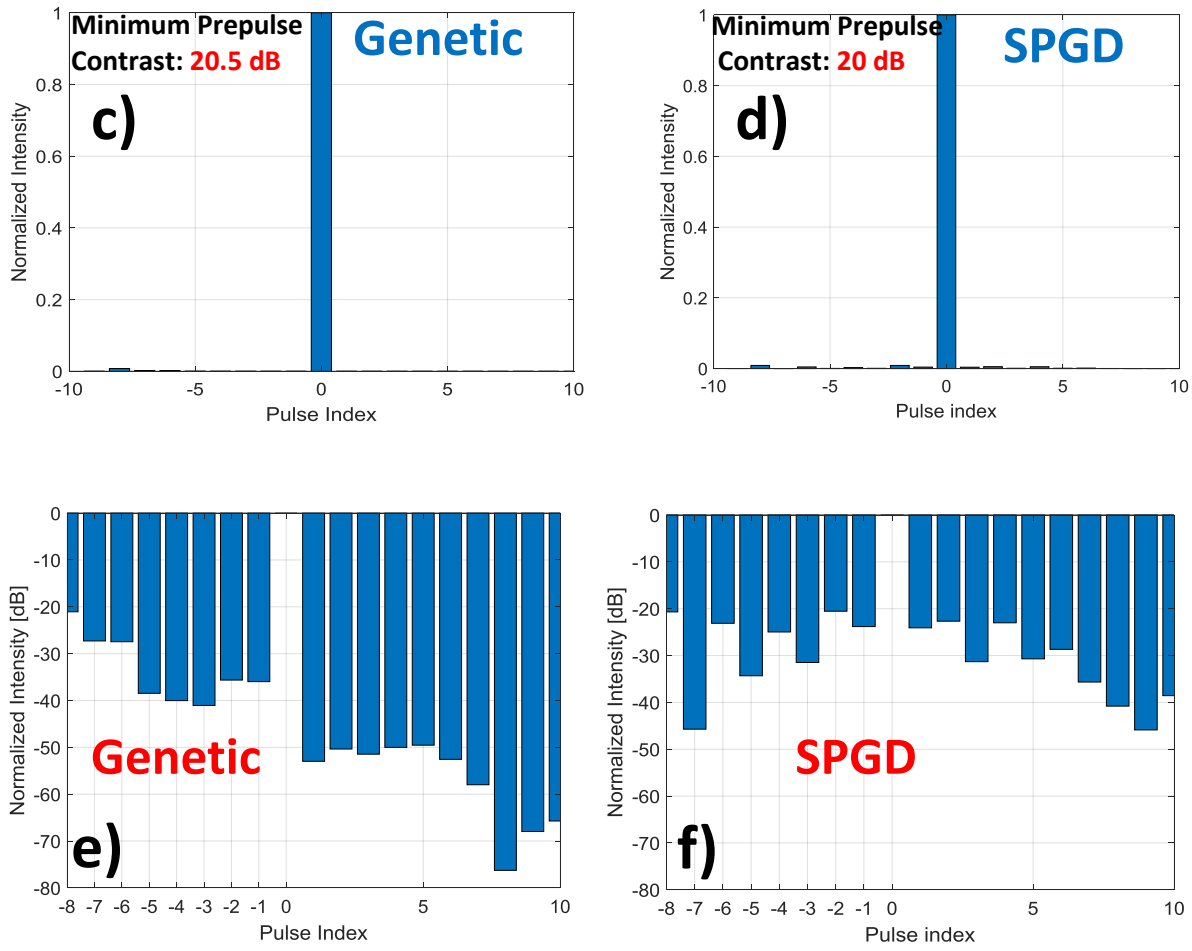

Figure 5.9: a) SHG profile over 120 iterations for 50 different perturbation distributions (Genetic) b) SHG profile over 1000 iterations for 50 different perturbation distributions (SPGD) c) & d) corresponding linear-scale stacked profile associated with Genetic and SPGD algorithms respectively. e) & f) corresponding logarithmic-scale stacked profile associated with Genetic and SPGD algorithms respectively

As shown in figure 5.9(a) and (b), both algorithms are capable to optimize the stacked profile, and to closely approach the "ideal" case, as measured in terms of the stacked-pulse peak power (i.e. stacking efficiency). The genetic algorithm seems to be a bit faster (approximately twice), but this is not very critical for our application. Two examples of stacked profiles after the optimization with each of the algorithms are presented in 5.9 (c), (d) – linear scale, and (e), (f) – logarithmic scale. What we can immediately notice is that pre-pulse contrast after the genetic-algorithm optimization is close 35dB (after discarding first three "reflected" pulses, as discussed

earlier), but only ~20dB after the SPGD optimization. It is important to state that for achieving >40dB contrast it will be imperative to modify the signal metric, i.e. instead of peak-power (proportional to SHG) optimization, it will be necessary to also measure the pre-pulse contrast as well. But this goes outside the scope of the current thesis work, and will have to be carried out I the future

Also, since the Genetic and SPGD algorithms are both intrinsically based on random numbers that are generated in each iteration, it is important to make sure the algorithm behavior does not diverge in different runs, and it always converges to the optimal point. In order to do this, we have run the two algorithms for number of times for 4 different starting points on the SHG landscape,1%, 20%, 40%, and 57% off of the global peak, and observed the behavior of the algorithms for those different runs.

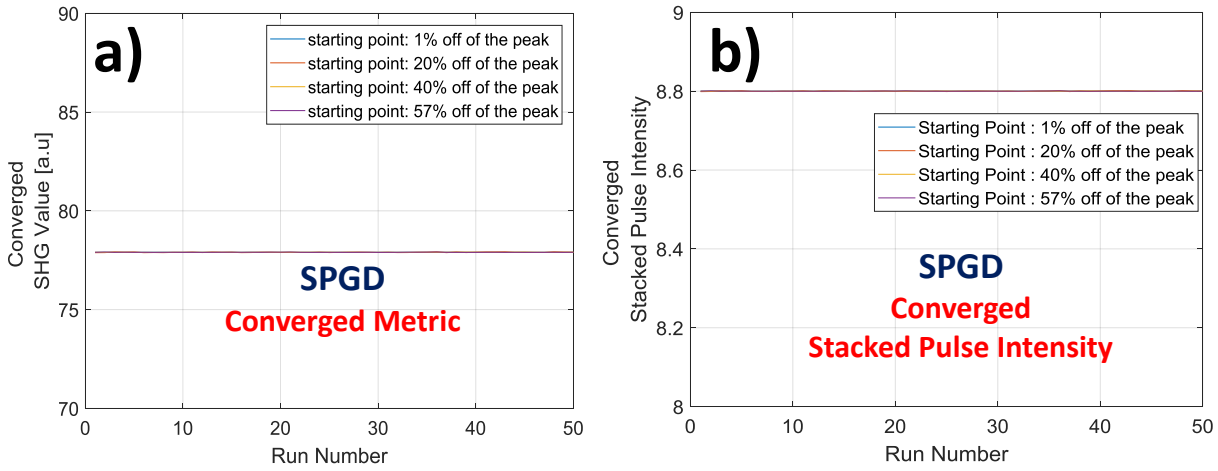

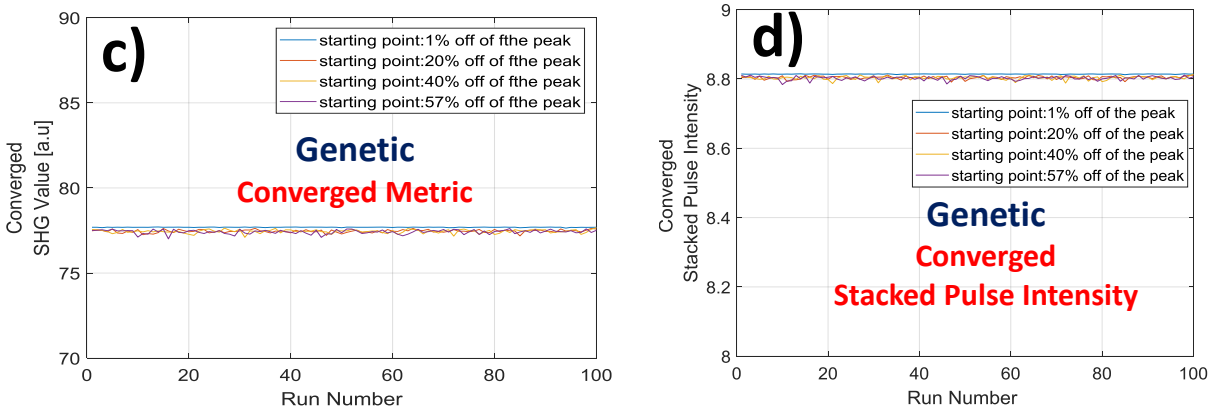

Figure 5.10: a) Converged SHG value for different runs (SPGD) b) Final Stacked Pulse for different runs (SPGD) c) Converged SHG value for different runs (GENETIC) d) Final Stacked Pulse for different runs (GENETIC)

As shown in Figure 5.10 a) and c), the two algorithms successfully converge to the global peak for all 50 runs. comparing a) and c) shows that final converged SHG value through SPGD is more insensitive to the randomness nature in different runs compared to the Genetic algorithm. The statistical changes of the stacked peak in different runs are also shown in Figure 5.10 b) and d). They also manifest that the optimized stacked pulse is guaranteed to be achieved for different runs both for SPGD and Genetic algorithm.

Chapter 6 Conclusions and Future Work

6.1 Conclusions

This thesis focused on utilizing efficient algorithms for stabilization and optimization aspects of CPSA and developing a robust, scalable, and distributed digital control system with firmware and software integration for algorithms, to support the CPS application.

Theoretical foundations of the control algorithms (specifically Stochastic Parallel Gradient Descent (SPGD) algorithm) as they pertain to both stabilizing the stacking system and optimizing the input burst profile have been fully presented. Hardware implementation along with firmware/software development for the FPGA-based Control system (In collaboration with LBNL) have been presented. This FPGA-based feedback control system is a distributed synchronous digitizer network with firmware and software integration for algorithms, therefore it can be scaled to large numbers of cavities. It also provides sufficiently high feedback loop speed enabling the user to control the system at different frequency regimes of interest.

A novel GTI-based Noise measurement technique for measuring stacking phase noise as well as the amplitude noise from the mode-locked oscillator has been developed. Detailed theoretical derivation for representing the output stacking noise in terms of the phase mismatch between the GTI stacker cavities and the oscillator cavity has been provided. We illustrate that the oscillator phase noise is the dominant factor contributing to the total output stacking noise. The details of how the technique works and how the measurement system was developed along with

some examples were shown. The neat thing about this is that it does not require any measurement of the frequency-comb merits such as linewidth which not only should be measured over a certain period of time but also requires complicated measurement setups such as the Heterodyne. Time-domain-based Allen Deviation technique as well as frequency-domain-based analysis of noise measurements have been used to better understand the characteristics of the measured noise in different frequency bands.

The GTI-based technique described above was applied to different stacking configurations (A 30cm-long GTI cavity with the same round-trip time as the oscillator's round-trip time, and a 2.7m-long GTI cavity with round-trip time 9 times the oscillator's round-trip time) to effectively measuring the characteristics of the mode-lock oscillator noise (and how they affect the output stacking. We mathematically and experimentally showed how the stacking phase noise gets more sensitive to the oscillator phase noise when a longer length GTI cavity is used for noise characterization. By effectively reducing the noise in the pump current and accordingly the oscillator phase noise, we experimentally manifested how the stacking noise can be reduced in an order of magnitude down to the limit of the amplitude noise of the oscillator. Simulation and experimental results for stabilization of two different GTI stacker configurations (4-Cascaded and 4+4 Multiplexed) have been presented.

For stacking fidelity improvement, an algorithmic-based optimization was implemented in the FPGA-based Control system in an outer-feedback-loop nested with the stabilization feedback loop. We have developed a dual-buffer DAC in the firmware enabling the 1GSPS DAC swap between two different amplitude waveforms between the pulses and output the updated waveform to the electro-optic modulators at the trigger arrival. In addition, a detailed discussion on different sources of disturbances/noises degrading the stacking fidelity was presented.

By implementing this optimization algorithm in the FPGA-control system, we effectively removed the previously existing Arbitrary-Waveform-Generators (AWGs) in the system which were not sufficiently fast in operation. We also developed a firmware that uses a reference trigger signal (e.g the 1MHz trigger signal synchronized with the laser) and generates different synchronous triggers to trigger the rest of the optical system such as the Acousto-optic-modulators (AOMs). This is a pathway to puts the FPGA system as the master clock for triggering the entire stacking system.

Finally, we developed a Genetic-Algorithm-Based optimization program to get more sense of how other optimization algorithms (other than SPGD) can effectively improve the stacking performance. In this analysis, a detailed description of how we implemented the Genetic Algorithm was presented first and then the performance of the algorithm in terms of the converged SHG metric and the optimized stacked profile was evaluated. A one-to-one comparison between the Genetic Algorithm and SPGD was also performed to see how effective they are in compensating for arbitrary changes in the pulse phases and hence optimizing the stacked profile.

6.2 Future Work

There are various paths of research to be explored specifically on control sides of the stacking system. one of the important desired characteristics of the stacked pulses is associated with a high degree of pre-pulse contrast of up approximately 40 – 60 dB, which is required by laser-plasma acceleration applications, as well as numerous other laser-matter interaction-based applications. Since in practice peak detection cannot be achieved with better than approximately 1% accuracy, this stacked-pulse fidelity metrics does not allow achieving pre--pulse of better than approximately 20 dB. At this point we had identified techniques with which this limitation

can be overcome (for example, developing a new fidelity measurement technique which would detect both the pre-pulse content and the stacked pulse peak). This opens a path for future works to be done to effectively increase pre-pulse contrast.

Bibliography

[1] Rafael R. Gattass and Eric Mazur, "Femtosecond laser micromachining in transparent materials," Nature Photonics 2(4), 219-225 (2008)

[2] Leemans, W.; Esarey, E. Laser-driven plasma-wave electron accelerators. Phys. Today 2009, 62(3), 44-49.

[3] Bahk, S-W., Pascal Rousseau, T. A. Planchon, Vladimir Chvykov, Galina Kalintchenko, Anatoly Maksimchuk, G. A. Mourou, and Victor Yanovsky. "Generation and characterization of the highest laser intensities (10 22 W/cm 2)." Optics letters 29, no. 24 (2004): 2837-2839.

[4] Chu, Yuxi, Zebiao Gan, Xiaoyan Liang, Lianghong Yu, Xiaoming Lu, Cheng Wang, Xinliang Wang et al. "High-energy large-aperture Ti: sapphire amplifier for 5 PW laser pulses." Optics letters 40, no. 21 (2015): 5011-5014.

[5] Limpert, Jens, Fabian Stutzki, Florian Jansen, Hans-Jürgen Otto, Tino Eidam, Cesar Jauregui, and Andreas Tünnermann. "Yb-doped large-pitch fibres: effective single-mode operation based on higher-order mode delocalisation." Light: Science and applications 1 (2012): e8.

[6] Ma, Xiuquan, Cheng Zhu, I-Ning Hu, Alex Kaplan, and Almantas Galvanauskas. "Singlemode chirally-coupled-core fibers With larger than 50μm diametercores." Optics express 22, no. 8 (2014): 9206-9219.

[8] M. Kienel, A. Klenke, T. Eidam, S. Hȍdrich, J. Limpert, and A. Tünnermann, "Energy scaling of femtosecond amplifiers using actively controlled divided-pulse amplification," Opt. Lett. 39(4), 1049-1052 (2014).

[9] Y. Zaouter, F. Guichard, L. Daniault, M. Hanna, F. Morin, C. Hȍnninger, E. Mottay, F. Druon, and P. Georges, "Femtosecond fiber chirped- and divided-pulse amplification system," Opt. Lett. 38(2), 106-108 (2013).

[10] R. Jason Jones, and Jun Ye, "Femtosecond pulse amplification by coherent addition in a passive optical cavity," Opt. Lett. 27(20), 1848-1850 (2002).

[11] S. Breitkopf, T. Eidam, A. Klenke, L. von Grafenstein, H. Carstens, S. Holzberger, ..., and J. Limpert, "A concept for multiterawatt fibre lasers based on coherent pulse stacking in passive cavities," Light: Science & Applications. 3(10), e211 (2014).

[12]. Tong Zhou, John Ruppe, Paul Stanfield, John Nees, Russell Wilcox, and Almantas Galvanauskas, " Resonant cavity based time-domain multiplexing techniques for coherently combined fiber laser systems," submitted to European Physical Journal (2015).

[13] Zhou, Tong, John Ruppe, Cheng Zhu, I-Ning Hu, John Nees, and Almantas Galvanauskas. "Coherent pulse stacking amplification using low-finesse Gires-Tournois interferometers." Optics Express 23, no. 6 (2015): 7442-7462.

[16] S. Zhou, F. W. Wise, and D. G. Ouzounov, "Divided-pulse amplification of ultrashort pulses," Opt. Lett. 32, 871–873 (2007).

[17] Kienel, Marco, Arno Klenke, Steffen Hȯdrich, Tino Eidam, Jens Limpert, and Andreas Tünnermann. "Divided-Pulse Amplification for High Energy Extraction." In Advanced Solid State Lasers, pp. ATu3A-09. Optical Society of America, 2013

[18] Breitkopf, Sven, et al. "A concept for multiterawatt fibre lasers based on coherent pulse stacking in passive cavities." Light: Science & Applications 3.10 (2014): e211.

[20] Ristau, Detlev, ed. Laser-induced damage in optical materials. CRC Press, 2014.

[22] Ruppe, John. "Theoretical and Experimental Foundations of Coherent Pulse Stacking Amplification." (2017).

[23] Phillips, Charles L., John M. Parr, and Eve A. Riskin. Signals, systems, and transforms. Prentice Hall, 1995.

[24] Siegman, Anthony E.. Lasers. : University Science Books, 1986.

[25] Xu, Yilun, et al. "FPGA-Based Optical Cavity Phase Stabilization for Coherent Pulse Stacking." IEEE Journal of Quantum Electronics (2017).

[26] Vorontsov, Mikhail A., and V. P. Sivokon. "Stochastic parallel-gradient-descent technique for high-resolution wave-front phase-distortion correction." JOSA A 15.10 (1998): 2745-2758

[27] www.ni.com

[28] Yang, Hui-zhen, and Xin-yang Li. "Theoretical analysis of adaptive optics system based on stochastic parallel gradient descent algorithm." Optoelectronics Letters 6.6 (2010): 426-428.

[29] Jiang, Wenhan, et al. "Hill-Climbing Wavefront Correction System For Large Laser Engineering." Current Developments in Optical Engineering III. Vol. 965. International Society for Optics and Photonics, 1989

[30] Cauwenberghs, Gert. "A fast stochastic error-descent algorithm for supervised learning and optimization." Advances in neural information processing systems. 1993.

[31] A. Dembo and T. Kailath, ‘‘Model-free distributed learning,’’ IEEE Trans. Neural Netw. 1,58–70 (1990).

[32] G. Cauwenberghs, ‘‘Analog VLSI stochastic perturbative learning architectures,’’ Int. J. Analog Integr. Circ. Signal Process. 13, 195–209 (1997).

[33] J. Alspector, R. Meir, B. Yuhas, and A. Jayakumar, ‘‘A parallel gradient descent method for learning in analog VLSI neural networks,’’ in Advances in Neural Information Processing Systems, J. D. Cowan, ed. (Morgan Kaufman, San Mateo, Calif., 1993), Vol. 5, pp. 836–844

[34] D. B. Kirk, D. Kerns, K. Fleischer, and A. H. Barr, ‘‘Analog VLSI implementation of multidimensional gradient descent,’’ in Advances in Neural Information Processing Systems, C. L. Giles, ed. (Morgan Kaufman, San Mateo, Calif., 1993), Vol. 5, pp. 789–796.

[35] M. Duflo. Random Iterative Models. Pringer, New York, 1991.

[36] H. Robbins and S. Monro. A stochastic approximation method. The Annals of Mathematical Statistics, 22(3):400–407, 1951.

[37] Zhou, Tong. Coherent Combining of Optical Pulses in Spatial, Spectral and Time Domains. Diss. University of Michigan, 2015.

[38] F. X. Kärtner, U. Morgner, T. Schibli, R. Ell, H. A. Haus, J. G. Fujimoto, and E. P. Ippen, “Few-cycle pulses directly from a laser,” Top. Appl. Phys. 95, 73–136 (2004).

[39] Paschotta, R., et al. "Optical phase noise and carrier-envelope offset noise of mode-locked lasers." Applied Physics B 82.2 (2006): 265-273
.

[40] Kim, Jungwon, and Youjian Song. "Ultralow-noise mode-locked fiber lasers and frequency combs: principles, status, and applications." Advances in Optics and Photonics 8.3 (2016): 465-540

[41] Barnes, James A., et al. "Characterization of frequency stability." IEEE transactions on instrumentation and measurement 1001.2 (1971): 105-120

[42] M. M. Tehrani, “Ring laser gyro data analysis with cluster sampling technique,” Proc. SPIE, vol. 412, pp. 207–220, 1983

[43] H. Hou, “Modeling inertial sensors errors using Allan variance,” M.S. thesis, MMSS Res. Group, Dept. Geomatics Eng., Univ. Calgary, Calgary, AB, Canada, UCGE Rep. 20201, Sep. 2004

[44] http://www.ti.com/lit/ds/symlink/ads5400.pdf

[45] J. H. Holland: Adaptation in natural and artificial systems. MIT Press, Cambridge, MA, 1 st Ed., 1975,2nd ed., 1992.

[46] Kinnear, K. E. (1994). A Perspective on the Work in this Book. In K. E. Kinnear (Ed.), Advances in Genetic Programming (pp. 3-17). Cambridge: MIT Press

[47] Mitchell, M. (1995). Genetic Algorithms: An Overview. Complexity, 1(1), 31-39

[48] Nise, Norman S. "Control system engineering, John Wiley & Sons." Inc, New York (2011).

[49] Goodwin, Graham C., Stefan F. Graebe, and Mario E. Salgado. "Control system design." Upper Saddle River 13 (2001).

[50] Oppenheim, A.V., Wilsky, A.S., and Hamid, N.S. (1997). Signals and Systems. Prentice–Hall, Upper Saddle River, N.J., 2nd. edition.

[51] A Novel Technique for Phase Locking Optical Fiber Arrays," T. M. Shay and Vincent Benham, in Free Space Laser Communications IV, Jennifer C. Ricklin and David G. Voelz, eds., Proc. SPIE 5550, 313-319 (2004).

[52] "First Experimental Demonstration of Fiber Array Phase Locking by RF Phase Modulation," T. M. Shay and Vincent Benham, Proceedings of the 17th Solid State and Diode Laser Technology Review, Sean Ross, ed., pg. BEAM (2004).

[53] "Self-synchronous Locking of Optical Coherence by Single-detector Electronic-frequency Tagging", T. M. Shay, US Patent 7,058,098, June 2006.

[54] Klenke, Arno, et al. "Coherently-combined two channel femtosecond fiber CPA system producing 3 mJ pulse energy." *Optics express* 19.24 (2011): 24280-24285.

[55] Hansch, T. W., and B. Couillaud. "Laser frequency stabilization by polarization spectroscopy of a reflecting reference cavity." *Optics communications* 35.3 (1980): 441-444.

[56] Pound, Robert V. "Electronic frequency stabilization of microwave oscillators." *Review of Scientific Instruments* 17.11 (1946): 490-505.

[57] White, A. "Frequency stabilization of gas lasers." *IEEE Journal of Quantum Electronics* 1.8 (1965): 349-357

[58] Drever, R. W. P.; Hall, J. L.; Kowalski, F. V.; Hough, J.; Ford, G. M.; Munley, A. J.; Ward, H. (June 1983). "Laser phase and frequency stabilization using an optical resonator". Applied Physics B. 31 (2): 97–105

[59] Black, Eric D. (2001). "An introduction to Pound–Drever–Hall laser frequency stabilization" . Am J Phys. 69 (1): 79–87

[60] Zommer S, Ribak EN, Lipson SG, Adler J. Simulated annealing in ocular adaptive optics. Opt Lett 2006;31(7):1–3.

[61] Kirkpatrick S, Gelatt CD, Vecchi MP. Optimization by simulated annealing. Science 1983;220:671–80.

[62] Zakynthinaki MS, Saridakis YG. Stochastic optimization for a tip-tilt adaptive correcting system. Comput Phys Commun 2003;150:274–92.

[63] Yang, Huizhen, and Xinyang Li. "Comparison of several stochastic parallel optimization algorithms for adaptive optics system without a wavefront sensor." Optics & Laser Technology 43.3 (2011): 630-635.

[64] Metropolis N, Rosenbluth AW, Rosenbluth MN, Teller AH, Teller E. Equation of state calculations by fast computing machines. J Chem Phys 1953;21:1087–92.

[65] Harth, E., & Tzanakou, E. (1974) Alopex: A stochastic method for determining visual receptive fields. Vision Research, **14**:1475-1482

[66] Sastry PS, Magesh M, Unnikrishnan KP. Two timescale analysis of the Alopex algorithm for optimization. Neural Comput 2002;14:2729–50.

[67] Klenke, Arno, et al. "530 W, 1.3 mJ, four-channel coherently combined femtosecond fiber chirped-pulse amplification system." Optics letters 38.13 (2013): 2283-2285